

**Michaela Scharfegger**

**HIGHLY STRUCTURED SILICON-GRAPHITE COMPOSITE  
MATERIALS FOR LITHIUM-ION BATTERIES**

## **Doctoral Thesis**

Submitted in fulfilment of requirements for the degree of  
Doctor of Technical Sciences

at the

**Graz University of Technology**

**Institute for Chemistry and Technology of Materials (ICTM)**

**In Cooperation with VARTA Micro Innovation GmbH**

This work has been carried out under the supervision of

**Univ.-Prof. Dipl.-Ing. Dr. techn. Franz Stelzer**

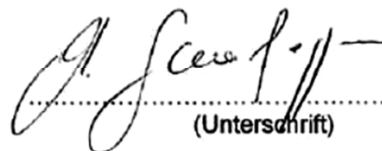
**2013**

Deutsche Fassung:  
Beschluss der Curricula-Kommission für Bachelor-, Master- und Diplomstudien vom 10.11.2008  
Genehmigung des Senates am 1.12.2008

## EIDESSTATTLICHE ERKLÄRUNG

Ich erkläre an Eides statt, dass ich die vorliegende Arbeit selbstständig verfasst, andere als die angegebenen Quellen/Hilfsmittel nicht benutzt, und die den benutzten Quellen wörtlich und inhaltlich entnommenen Stellen als solche kenntlich gemacht habe.

Graz, am 19.08.2013

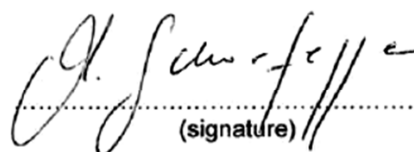
  
.....  
(Unterschrift)

Englische Fassung:

## STATUTORY DECLARATION

I declare that I have authored this thesis independently, that I have not used other than the declared sources / resources, and that I have explicitly marked all material which has been quoted either literally or by content from the used sources.

19.08.2013  
date

  
.....  
(signature)

## **ACKNOWLEDGEMENT**

I am very grateful to my supervisor, the head of the Institute for Chemistry and Technology of Materials, Prof. Dipl.-Ing. Dr. techn. Franz Stelzer for giving me the opportunity to write this doctoral thesis and for his excellent guidance during the last years.

Furthermore, I would like to express my real gratitude to my financial supporter, the company Varta Micro Innovation GmbH. In this context, my special appreciation deserves Dr. Stefan Koller, the CEO of the company, and Dr. Harald Kren, my project manager, for their guidance and dedication the whole way of my thesis.

Additionally, I am deeply and honestly grateful that I had the chance to work together with such great colleagues and friends. I would like to start with Stephania Toulis, because without her practical support I had not finished yet. MSc Sandra Pötz and Christian Baumann for their support especially in the thesis writing phase. Dr. Christoph Stangl, Dipl.-Ing. Patricia Handel and Dr. Bernd Fuchsbichler for their theoretical support on this doctoral thesis. Furthermore, I would like to thank my colleagues Dipl.-Ing. Katharina Gruber, Katja Kapper, Andrea Droisner, Dipl.-Ing. Gisela Fauler, Dr. Martin Schmuck and MSc Pierre Baumann.

I am particularly grateful and want to acknowledge the Austrian Centre for Electron Microscopy and Nanoanalysis FELMI-ZFE for the impressive electron microscopic images in this doctoral thesis.

Furthermore, I would also like to thank the scientific and non-scientific staff members of the ICTM, TU Graz.

Finally, I would like to express my deep gratitude to Christoph Scheifflinger for the proof reading and linguistic revision of my thesis as well as relatives and friends, who supported me in the last years.

## **Abstract**

Nowadays, the lithium-ion battery is omnipresent as energy storage system, starting in the area of portable electronic devices, such as mobile phones, laptops, and ending up in high energy and power applications like stationary power supplies and the automotive branch, recently. Especially due to the demanded high energy- and power densities, the lithium-ion battery was able to achieve a dominant position in the sector of rechargeable batteries within the last years. To keep this supremacy, continuous development regarding to energy, power and safety is necessary and has been done within the last years. The measures to increase the energy and power of this system are mainly focused on the research of the anode and cathode active materials, whereby the tendency is going to high-capacity anode and high-voltage cathode active materials. Potential candidates for high-capacity anode active materials are lithium alloys, but due to their low cycle stability, caused by high volume changes during the lithiation and delithiation process, these materials are far away from commercial application.

Within this thesis a successful fabrication of a high-capacity silicon-graphite composite material with special particle design was carried out. The embedding of volume-expanding silicon particles in a carbonaceous matrix on single graphite particles improved the structural stability and cycle stability, respectively.

## **Kurzfassung**

Heutzutage ist die Lithium-Ionen Batterie als Energiespeichersystem nahezu allgegenwärtig, beginnend im Bereich der portablen Elektronikgeräte wie Mobiltelefone oder Laptops, bis hin zu Hochenergie- und Hochleistungsanwendungen im stationären Energieversorgungsbereich und jüngst im automotiven Bereich. Insbesondere durch die Nachfrage zur Bereitstellung von hohen Energie- und Leistungsdichten war es der Lithium-Ionen Batterie möglich, in den vergangenen Jahren eine solch dominante Position im Bereich der wiederaufladbaren Batterien einzunehmen. Um diese Position halten zu können, ist eine stetige Weiterentwicklung in den Bereichen Energie, Leistung und Sicherheit notwendig und konnte auch in den vergangenen Jahren beobachtet werden. Das Hauptaugenmerk hinsichtlich energie- und leistungserhöhenden Maßnahmen liegt überwiegend im Bereich der Anoden- als auch Kathodenmaterialforschung. Diesbezüglich geht die Entwicklung in Richtung hochkapazitiver Anodenmaterialien sowie Kathodenmaterialien, welche höhere Spannungsbereiche erlauben. Potenzielle Kandidaten für solche hochkapazitiven Anodenmaterialien sind vor allem Materialien, die mit Lithium Legierungen bilden. Da diese jedoch durch ihre enormen Volumenänderungen während des Lithiierungs- bzw. Delithiierungsprozesses eine mangelnde Zyklenstabilität aufweisen, sind sie von einer kommerziellen Anwendung weit entfernt.

Im Rahmen dieser Dissertationsarbeit konnte erfolgreich ein hochkapazitives Silizium-Graphit Kompositmaterial mit einem neuartigen Partikeldesign hergestellt werden. Durch Einbettung der volumenexpandierenden Siliziumpartikel in eine kohlenstoffbasierende Matrix und Aufbringen dieser Ummantelung auf einzelne Graphitpartikel konnte eine Optimierung dieser Kompositmaterialien hinsichtlich Struktur- bzw. Zyklenstabilität erreicht werden.

# Table of Contents

<b>1</b>	<b>Introduction .....</b>	<b>1</b>
<b>2</b>	<b>Theoretical basics.....</b>	<b>3</b>
2.1	Electrochemical system.....	3
2.2	Fundamental thermodynamics .....	6
2.3	Battery characteristics.....	16
<b>3</b>	<b>Lithium-ion battery.....</b>	<b>18</b>
3.1	Historical background of lithium-ion batteries.....	18
3.2	Construction of a lithium-ion battery .....	19
3.3	Active materials for lithium-ion batteries.....	21
3.3.1	Negative active materials: Carbonaceous-based insertion materials .....	23
3.3.2	Negative active materials: Lithium alloys .....	25
3.3.2.1	Lithium alloys: Silicon .....	27
3.3.3	Positive active materials .....	30
3.3.3.1	Layered transition metal oxides $\text{LiMO}_2$ .....	30
3.3.3.2	Spinel type compound $\text{LiMn}_2\text{O}_4$ .....	32
3.3.3.3	Olivine type compounds $\text{LiMPO}_4$ .....	32
3.4	Nonaqueous liquid electrolytes for lithium-ion batteries.....	34
3.4.1	Separators .....	36
3.4.2	Electrolyte/electrode interphases .....	37
3.5	Ageing mechanisms in lithium-ion batteries.....	39
<b>4</b>	<b>Experimental Part.....</b>	<b>43</b>
4.1	Electrode fabrication and measurement setup .....	43
4.2	Electrochemical characterisation .....	44
4.3	Particle characterisation.....	45
4.4	Active material fabrication: Fluidized bed reactor .....	46
4.5	Introduction.....	49

<b>4.6</b>	<b>Research on polymer precursors .....</b>	<b>50</b>
<b>4.7</b>	<b>Generation 1 of silicon-graphite composite materials .....</b>	<b>53</b>
4.7.1	Fabrication procedure.....	53
4.7.2	Optimization of EP/CNP composition.....	54
4.7.3	Optimization of the pyrolysis process.....	58
<b>4.8</b>	<b>Generation 2 of silicon-graphite composite materials .....</b>	<b>61</b>
4.8.1	Fabrication procedure.....	62
4.8.2	Optimization of the EP/CNP composition.....	65
4.8.3	Optimization of the spray drying process .....	69
4.8.4	Influence of varied shell compositions.....	74
4.8.4.1	Influence of increasing silicon particle sizes.....	75
4.8.4.2	Influence of increasing silicon content.....	77
4.8.4.3	Influence of varied carbonaceous matrix compositions.....	79
4.8.5	Further development of Gen2 materials.....	82
<b>4.9</b>	<b>Generation 3 of silicon-graphite composite particles .....</b>	<b>84</b>
4.9.1	Fabrication procedure.....	85
4.9.2	Varying parameters and their influences on Gen3 materials .....	85
4.9.2.1	Influence of increasing shell thickness/silicon content .....	88
4.9.2.2	Influence of initial carbon black .....	94
4.9.3	Optimization of the coating process .....	97
4.9.3.1	Optimization of the coating process: Constant pump speed and varied pressure of spray flow .....	98
4.9.3.2	Optimization of the coating process: Varied pump speed and constant pressure of spray flow .....	100
4.9.4	Structural characterisation of a Gen3 particle with focused ion beam technique .....	103
<b>4.10</b>	<b>Comparison of the different generations of materials.....</b>	<b>105</b>
4.10.1	Rate capability tests of Gen(1-3) materials .....	110
<b>4.11</b>	<b>Characterisation of a Gen2 material with transmission electron microscopy.....</b>	<b>112</b>
<b>5</b>	<b>Conclusion .....</b>	<b>116</b>
<b>6</b>	<b>Appendix.....</b>	<b>118</b>
<b>6.1</b>	<b>List of chemicals.....</b>	<b>118</b>
<b>6.2</b>	<b>List of devices.....</b>	<b>119</b>
<b>6.3</b>	<b>List of abbreviations .....</b>	<b>119</b>

<b>6.4</b>	<b>List of figures</b> .....	<b>121</b>
<b>6.5</b>	<b>List of tables</b> .....	<b>125</b>
<b>6.6</b>	<b>References</b> .....	<b>128</b>

# 1 Introduction

In recent years, a rapid development has taken place in the area of portable electronic devices (mobile phones, lap-tops etc.), resulting in a rising energy demand within this area. Therefore, the remarkable almost simultaneously industrial upturn of secondary batteries is not surprising. Due to their high energy and power density, lithium-ion batteries (LIBs) were able to prevail at the worldwide battery market against other rechargeable battery systems, such as nickel-cadmium or nickel-metal hydride battery (Figure 1). Nowadays, the LIB is one of the most frequently used rechargeable battery system.

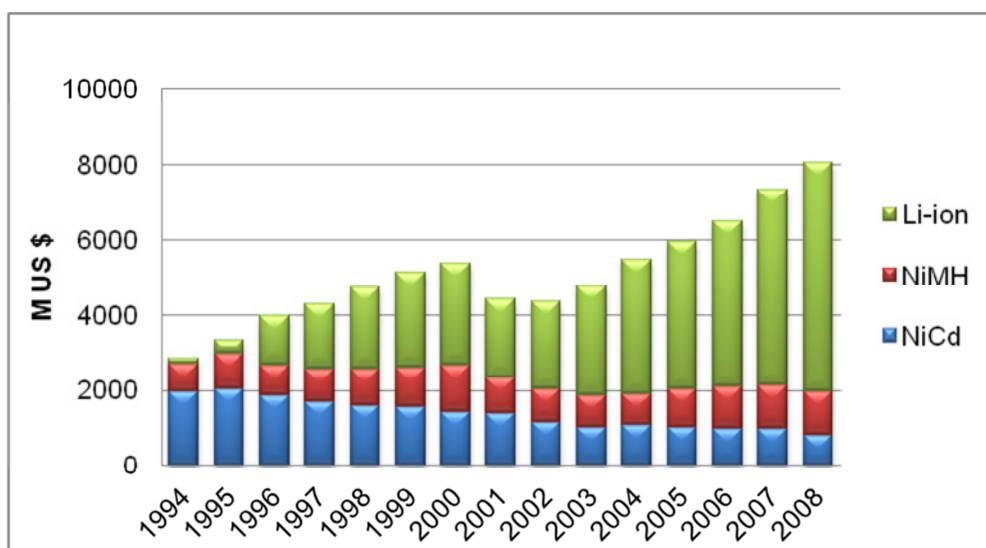
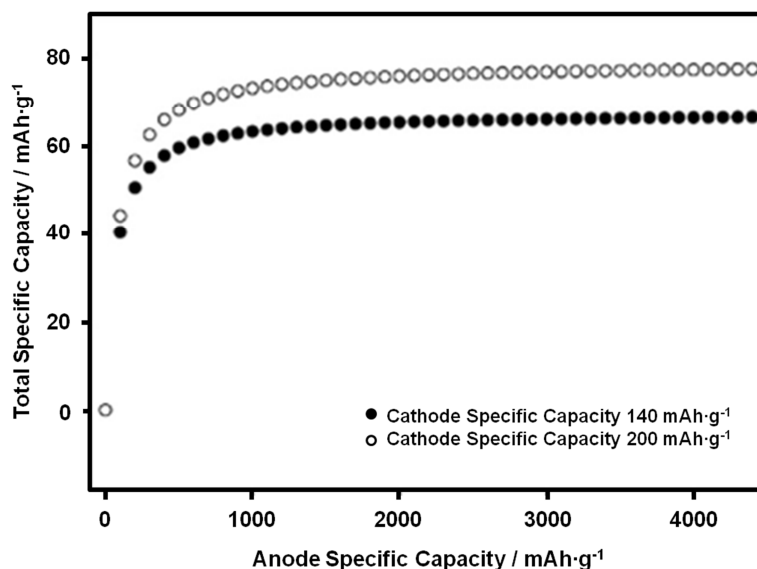


Figure 1: Rechargeable battery market worldwide (redrawn from [1])

Decreasing oil reserves, a growing interest of society in sustainable energy and a rapid development of lithium-ion batteries, since their market introduction in the 1990s, were the main reasons for automotive industry discovering this battery system for its application. Today it represents one of the most promising systems to replace ecologically harmful combustion engines in the future.

Due to this new application area LIB systems are facing new challenges. On the one hand the energy and/or the power density of this battery system needs to be improved and on the other hand costs have to be reduced in order to compete with the low cost combustion engine.

An improvement of the energy is mainly achieved, either by the increase of the specific capacities of the electrode materials and/or by enlarging the potential difference between the positive and negative electrode materials. This in turn led to an intensive research on new and advanced active materials within the last years.



**Figure 2: The total cell capacity (18650 Li-ion cell) as a function of the anode capacity including masses of other required internal components and case [2]**

A promising approach for increasing the cell capacity of LIBs is based on the replacement of the commonly used anode material graphite with a high-capacity anode material such as silicon. Unfortunately, the major disadvantage of these high capacity anode materials is the poor cycle stability due to high volume changes during the lithiation and delithiation processes. Furthermore, the increase of anode capacity with the intention to improve the cell capacity is only useful until the anode capacity reaches a value of  $1200 \text{ mAh}\cdot\text{g}^{-1}$ , as further increases are negligible for higher cell capacities (Figure 2).

In the context of this doctoral thesis, composite materials, consisting of structure-stable graphite and high-capacity silicon, were fabricated. These composite materials are able to provide high volume stability and deliver satisfying capacities in the range of 1000 to  $1200 \text{ mAh}\cdot\text{g}^{-1}$ . Due to the special structure of these new developed composite materials, it was possible to compensate the high volume changes of silicon.

## 2 Theoretical basics

### 2.1 Electrochemical system

In general, a battery is an electrochemical energy source, which is able to convert chemical into electrical energy, by electrochemical oxidation and reduction reactions occurring at its electrodes. Moreover, such batteries consist of one, or an ensemble of electrochemical single cells, which are connected in series and/or parallel.

Electrochemical cells are divided in two sub-types, the galvanic cell and the electrolytic cell. While the electrochemical reactions of galvanic cells are spontaneous ( $\Delta G < 0$ ), electrolytic cells need an applied external energy to start their electrochemical reactions ( $\Delta G \geq 0$ ). [3] [4]

Furthermore, depending on the principle of operation, electrochemical cells are divided in the following three groups [5]

1. **Primary cell:** These cells are not rechargeable cells, due to an irreversible overall electrochemical reaction. This implies that after the fixed amount of educts is consumed by discharge, the cell cannot be used again.
2. **Secondary cell:** Secondary cells, also called accumulators, work with reversible electrochemical reactions, which offer the possibility to recharge the cells several times.
3. **Fuel cell:** Contrary to secondary cells, fuel cells have an open system, where the reactants are continuously fed into the cell.

A characteristic feature of an electrochemical cell is the generation of an electric current by the electrochemical processes taking place at the electrodes. Generally, the resulting electric current, which is more precisely the movement of electrons in the external circuit, is counterbalanced by the movement of ions between the positive and negative electrode within the electrolyte. [5]

For a better understanding of the operating principle of an electrochemical cell, a schematical illustration of a galvanic cell is given in figure 3. As demonstrated, such galvanic cell consists of two electrodes, which immerse in an ion-conducting electrolyte and are electrically

conducted through an external circuit. The salt bridge is responsible for the ionic charge transfer between the two half-cells. The negative electrode is always represented by the electrode with the more negative redox-potential relative to the counter electrode. An oxidation process at the negative electrode leads to the generation of electrons. These electrons are consumed again by the reduction process, which occurs at the positive electrode. [3] [5] [6]

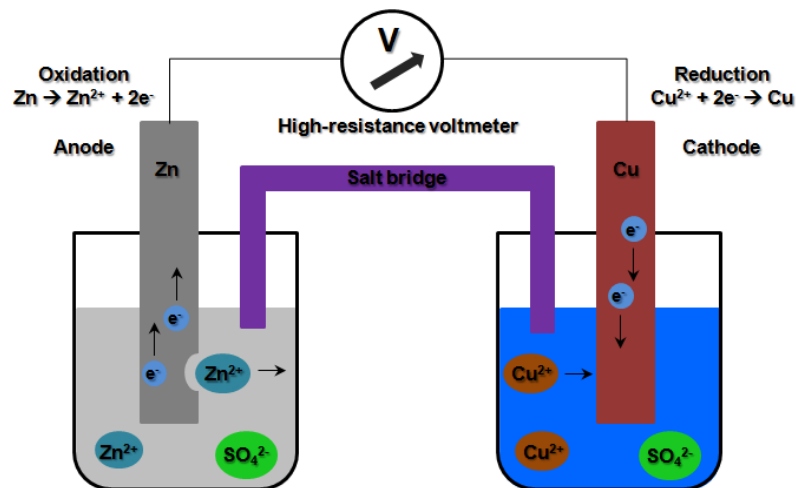
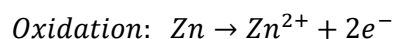
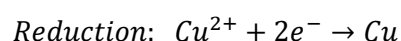


Figure 3: Schematic illustration of galvanic cell (Daniell element) (redrawn from [7])

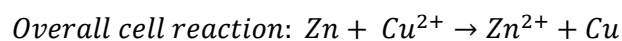
The Daniell element, illustrated in figure 3, is a well-known example of a galvanic cell, consisting of a copper positive electrode and a zinc negative electrode, in electrolyte solutions of their corresponding ions. If the electrodes of the two half cells are electrically connected by an external circuit and ionically contacted by a salt bridge, an oxidation at the less nobler zinc electrode and reduction reaction at the nobler copper electrode starts at same time. In sum, the following cell reactions occur in the Daniell element. [5]



[Eq. 1]



[Eq. 2]



[Eq. 3]

Basically, a direct measurement of the absolute potential of a single electrode is not possible, only the potential difference of the two half-cells can be measured in galvanic cells. Consequently, a reference potential is required to determine the electrode potential of a single electrode.

A list of some electrode potentials under standard conditions is represented in Figure 4. In this so called electrochemical series, chemical elements are ranked in order to their standard electrode potentials. Within this series, the arbitrary zero point is set by the potential of the normal hydrogen electrode (NHE). [5]

Considering the zinc and copper electrode metals of the Daniell element, the following standard potentials can be obtained



*E<sup>0</sup> ...electrode potential under equilibrium conditions*

These two standard potentials result in the following terminal voltage under equilibrium conditions

$$\Delta\varepsilon_{00} = E^0(\text{Cu}/\text{Cu}^{2+}) - E^0(\text{Zn}/\text{Zn}^{2+}) = (+0,34V) - (-0,76V) = \mathbf{1,10V}$$

**[Eq. 5]**

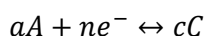
*Δε<sub>00</sub>...potential difference between two half cells under equilibrium conditions*

(Oxidised form + ne <sup>-</sup> )	⇌ Reduced form)	E <sup>0</sup> /V
F <sub>2</sub> (g) + 2e <sup>-</sup>	⇌ 2F <sup>-</sup>	2.87
Co <sup>3+</sup> + e <sup>-</sup>	⇌ Co <sup>2+</sup>	1.81
H <sub>2</sub> O <sub>2</sub> + 2H <sup>+</sup> + 2e <sup>-</sup>	⇌ 2H <sub>2</sub> O	1.78
MnO <sub>4</sub> <sup>-</sup> + 8H <sup>+</sup> + 5e <sup>-</sup>	⇌ Mn <sup>2+</sup> + 4H <sub>2</sub> O	1.51
Au <sup>3+</sup> + 3e <sup>-</sup>	⇌ Au(s)	1.4
Cl <sub>2</sub> (g) + 2e <sup>-</sup>	⇌ 2Cl <sup>-</sup>	1.36
Cr <sub>2</sub> O <sub>7</sub> <sup>2-</sup> + 14H <sup>+</sup> + 6e <sup>-</sup>	⇌ 2Cr <sup>3+</sup> + 7H <sub>2</sub> O	1.33
O <sub>2</sub> (g) + 4H <sup>+</sup> + 4e <sup>-</sup>	⇌ 2H <sub>2</sub> O	1.23
MnO <sub>2</sub> (s) + 4H <sup>+</sup> + 2e <sup>-</sup>	⇌ Mn <sup>2+</sup> + 2H <sub>2</sub> O	1.23
Br <sub>2</sub> + 2e <sup>-</sup>	⇌ 2Br <sup>-</sup>	1.09
NO <sub>3</sub> <sup>-</sup> + 4H <sup>+</sup> + 3e <sup>-</sup>	⇌ NO(g) + 2H <sub>2</sub> O	0.97
2Hg <sup>2+</sup> + 2e <sup>-</sup>	⇌ Hg <sub>2</sub> <sup>2+</sup>	0.92
Ag <sup>+</sup> + e <sup>-</sup>	⇌ Ag(s)	0.80
Fe <sup>3+</sup> + e <sup>-</sup>	⇌ Fe <sup>2+</sup>	0.77
O <sub>2</sub> (g) + 2H <sup>+</sup> + 2e <sup>-</sup>	⇌ H <sub>2</sub> O <sub>2</sub>	0.68
I <sub>2</sub> + 2e <sup>-</sup>	⇌ 2I <sup>-</sup>	0.54
Cu <sup>+</sup> + e <sup>-</sup>	⇌ Cu(s)	0.52
Cu <sup>2+</sup> + 2e <sup>-</sup>	⇌ Cu(s)	0.34
AgCl(s) + e <sup>-</sup>	⇌ Ag(s) + Cl <sup>-</sup>	0.22
AgBr(s) + e <sup>-</sup>	⇌ Ag(s) + Br <sup>-</sup>	0.10
2H <sup>+</sup> + 2e <sup>-</sup>	⇌ H <sub>2</sub> (g)	0.00
Pb <sup>2+</sup> + 2e <sup>-</sup>	⇌ Pb(s)	-0.13
Sn <sup>2+</sup> + 2e <sup>-</sup>	⇌ Sn(s)	-0.14
Ni <sup>2+</sup> + 2e <sup>-</sup>	⇌ Ni(s)	-0.25
Fe <sup>2+</sup> + 2e <sup>-</sup>	⇌ Fe(s)	-0.44
Cr <sup>3+</sup> + 3e <sup>-</sup>	⇌ Cr(s)	-0.74
Zn <sup>2+</sup> + 2e <sup>-</sup>	⇌ Zn(s)	-0.76
2H <sub>2</sub> O + 2e <sup>-</sup>	⇌ H <sub>2</sub> (g) + 2OH <sup>-</sup> (aq)	-0.83
Al <sup>3+</sup> + 3e <sup>-</sup>	⇌ Al(s)	-1.66
Mg <sup>2+</sup> + 2e <sup>-</sup>	⇌ Mg(s)	-2.36
Na <sup>+</sup> + e <sup>-</sup>	⇌ Na(s)	-2.71
Ca <sup>2+</sup> + 2e <sup>-</sup>	⇌ Ca(s)	-2.87
K <sup>+</sup> + e <sup>-</sup>	⇌ K(s)	-2.93
Li <sup>+</sup> + e <sup>-</sup>	⇌ Li(s)	-3.05

Figure 4: Electrochemical series of metals (redrawn from [8])

## 2.2 Fundamental thermodynamics

In general, there are two electrode interfaces in a cell, where the essential reactions take place, this can be represented for one electrode by



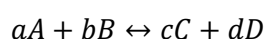
[Eq. 6]

and for the other by



[Eq. 7]

Resulting in the following overall reaction for both half-cell reactions



[Eq. 8]

At one electrode  $a$  molecules of  $A$  take up  $n$  electrons  $e^-$  to form  $c$  molecules of  $C$  whereby at the other electrode  $b$  molecules of  $B$  release  $n$  electrons  $e^-$  to form  $d$  molecules of  $D$ . [4] Summing up, during the discharge of a cell an oxidation process occurs at the negative active material, resulting in a release of electrons. The uptake of these electrons by the positive active material leads simultaneously to the reduction of itself. The generated electron current has to be balanced by an ion current within the electrolyte between the electrodes. The relationship between the electric current  $i$  and the mass  $m$  of the substance which donates/releases electrons, known as Faraday's first law, is given by [9] [5]

$$m = \frac{M}{z \cdot F} \cdot i \cdot t$$

[Eq. 9]

$$F = \frac{i \cdot t}{n} = \frac{Q}{n} = N_A \cdot e$$

[Eq. 10]

*m...active mass; M...molar mass; z...number of electrons exchanged; i...current; t...time; F...Faraday constant; Q...electric charge; n...numbers of electrons exchanged; e...elementary charge; N<sub>A</sub>...Avogadro constant*

Considering both, the anodic and cathodic processes of half-cells, Faraday recognized that at different electrode reactions and same amount of charge, the ratio of the reacting masses is equal to the ratio of the equivalent masses, which leads directly to the Faraday's second law [5]

$$\frac{m_A}{m_B} = \left( \frac{M_A | z_B |}{M_B | z_A |} \right)$$

[Eq. 11]

*m<sub>A</sub>...active mass (component A); M<sub>A</sub>...molar mass (component A); z<sub>A</sub>...number of electrons exchanged (component A); m<sub>B</sub>... active mass (component B); M<sub>B</sub>... molar mass (component B); z<sub>B</sub>... number of electrons exchanged (component B)*

The reaction free energy  $\Delta G$  represents the utilizable electrical energy of the electrochemical cell. [5] Furthermore, the change of  $\Delta G$  in the cell reaction is the driving force, which enables the cell to deliver electrical energy to an external circuit. [5] In this context, it is possible to calculate the cell voltage  $\Delta \varepsilon_{00}$  of an electrochemical cell from the reaction free energy  $\Delta G$ ,

instead of the direct measurement of the equilibrium cell voltage  $\Delta\varepsilon_{00}$  under standard conditions. [5] The reaction free energy  $\Delta G$  can be described by the following Gibbs-Helmholtz relation. [9]

$$\Delta G = \Delta H - T \cdot \Delta S$$

[Eq. 12]

$\Delta G$  ... reaction free energy (utilizable electrical energy);  $\Delta H$ ... reaction enthalpy (theoretical available energy);  
 $T$ ...temperature;  $\Delta S$ ...entropy;  $T \cdot \Delta S$ ...product of temperature and entropy (describes the amount of heat consumed or released reversible during the reaction)

If the following thermodynamic considerations are fulfilled

- All partial processes in a cell have to remain in equilibrium (reversible cell reaction)
- The current is kept infinitely small (cell voltage  $\Delta\varepsilon_0$  and the equilibrium cell voltage  $\Delta\varepsilon_{00}$  are equal)
- No concentration gradient in the electrolyte

it is possible to determine the reaction free energy of the cell as following [5]

$$\Delta G = -z \cdot F \cdot \Delta\varepsilon_{00}$$

[Eq. 13]

$\Delta\varepsilon_{00}$ ...equilibrium cell voltage

Additionally, it has to be mentioned that the potential difference or cell voltage under equilibrium conditions can be described by following equation

$$\Delta\varepsilon_{00} = E^0_{(positive\ electrode)} - E^0_{(negative\ electrode)}$$

[Eq. 14]

$\Delta\varepsilon_{00}$ ...equilibrium cell voltage;  $E^0_{(positive\ electrode)}$ ...standard electrode potential of the positive electrode;  
 $E^0_{(negative\ electrode)}$ ... standard electrode potential of the negative electrode

The equilibrium cell voltage  $\Delta\varepsilon_{00}$ , as well as the reaction free energy  $\Delta G$  under standard conditions, are related to the sum of the chemical potentials  $\mu_i$  of the involved substances and can be written as

$$-\frac{\Delta G}{z \cdot F} = \Delta\varepsilon_{00} = \frac{1}{z \cdot F} \sum v_i \cdot \mu_i$$

[Eq. 15]

$\mu_i$ ...chemical potentials of substance;  $v_i$ ...stoichiometric factor of  $i$  compound

If the chemical potential  $\mu_i$  of one half-cell depends on the concentration  $c_i$  of the reacting compounds at the electrode, then  $\mu_i$  is given by

$$\mu_i = \mu_{i,0} + R \cdot T \cdot \ln c_i$$

[Eq. 16]

$R$ ...universal gas constant;  $T$ ...temperature;  $c_i$ ...concentration of the compounds

Considering equation [Eq. 16], the standard electrode potential of the single half-cell is related to the concentration of the involved compounds. This correlation between concentration and potential is described by the Nernst equation.

$$\Delta\varepsilon_0 = \Delta\varepsilon_{00} + \frac{R \cdot T}{z \cdot F} \cdot \sum v_i \cdot \ln c_i$$

[Eq. 17]

Furthermore, the Nernst equation for a metal-ion electrode is written as follows

$$\Delta\varepsilon_0 = \Delta\varepsilon_{00} + \frac{R \cdot T}{z \cdot F} \cdot \ln \left( \frac{c_{Ox}}{c_{Red}} \right)$$

[Eq. 18]

Moreover, if a current flows, for instance while discharging an electrochemical cell, a shift in the potential of the single half-cell is measured. This shift in the potential is called over-potential  $\eta$ . Due to the fact that the sum of the occurred over-potentials decreases the real potential  $\Delta\varepsilon_{real}$  of the cell ([Eq. 19]), it is given by [5]

$$\Delta\varepsilon_{real} = \Delta\varepsilon_0 - \sum |\eta|$$

[Eq. 19]

*$\Delta\varepsilon_{real}$ ...real potential;  $\eta$ ...over-potential*

In detail the over-potentials in a cell can be subdivided in the following types [5]

- **Charge-transfer over-potential:** This kind of over-potential is caused by a limitation on the speed of charge transfer through the phase-boundary of electrode and electrolyte.
- **Diffusion over-potential:** At high current densities poor supply of the reacting substance can be originated. In this case the reaction is limited by the diffusion process or mass transport of the reacting substance to the electrode surface.
- **Reaction over-potential:** Compared to the charge-transfer and diffusion over-potentials, the reaction over-potential plays a tangential role. It originates if adsorption and desorption are the speed-limiting steps of the reaction.
- **Crystallisation over-potential:** The origin of this over-potential is an inhibited intercalation of metals ions into their lattice. Leading to a shift in the overall cell voltage and increasing the cell temperature, this over-potential plays an important role for all charge processes in secondary batteries.

In general, the overall current  $i$  of a cell can be written as

$$i = i_c + i_a$$

[Eq. 20]

$i$ ...overall current;  $i_c$ ...cathodic (reduction) current;  $i_a$ ...anodic (oxidation) current

$$j = j_c + j_a$$

[Eq. 21]

$j$ ...overall current density ( $A\ cm^{-2}$ );  $j_c$ ...cathodic (reduction) current density;  $j_a$ ...anodic (oxidation) current density

If the cell is in equilibrium and therefore no net current is detectable, the anodic and the cathodic currents are equal.

$$i_0 = |i_c| = i_a \quad \text{or} \quad j_0 = |j_c| = j_a$$

[Eq. 22]

$i_0$ ...exchange current;  $j_0$ ...exchange current density

Furthermore, the current of an electrode, which is directly related to the electrode potential, can be described by the Butler-Volmer equation, one of the fundamental relationships in the electrochemical kinetics. If the electrode reaction is only controlled by the electrical charge transfer at the electrode (*charge-transfer over-potential*) and the mass-transfer limitations are eliminated, the Butler-Volmer equation is given by [3]

$$i = i_0 \cdot \left[ \exp\left(\frac{-\alpha \cdot z \cdot F}{R \cdot T} \cdot \eta\right) - \exp\left(\frac{(1 - \alpha) \cdot z \cdot F}{R \cdot T} \cdot \eta\right) \right]$$

[Eq. 23]

$\alpha$ ...transfer coefficient (dimensionless)

In the case of a mass-transfer limited reaction the equation [Eq. 23] has to be extended by [3]

$$i = i_0 \cdot \left[ \frac{C_o(0,t)}{C_o^*} \cdot \exp\left(\frac{-\alpha \cdot z \cdot F}{R \cdot T} \cdot \eta\right) - \frac{C_r(0,t)}{C_r^*} \cdot \exp\left(\frac{(1-\alpha) \cdot z \cdot F}{R \cdot T} \cdot \eta\right) \right]$$

[Eq. 24]

$C_o(0,t)$ ... concentration of the oxidized species at the distance 0 from the electrode surface at the time  $t$ ;  
 $C_r(0,t)$ ... concentration of the reduced species at the distance 0 from the electrode surface at the time  $t$ ;  
 $C_o^*$ ... concentration of oxidized species;  $C_r^*$ ... concentration of reduced species

The exchange current  $i_0$  can be described as the rate of oxidation and reduction at an electrode under equilibrium conditions. [10] With regard to this, the higher the exchange current  $i_0$ , the lower the applied over-potential  $\eta$  will be in order to reach a defined current  $i$ . [6] The exchange current  $i_0$  can be experimentally determined by the use of the Tafel plot (Figure 5). It is given by the extrapolated intercept at zero over-potential  $\eta = 0$ . [11] [3]

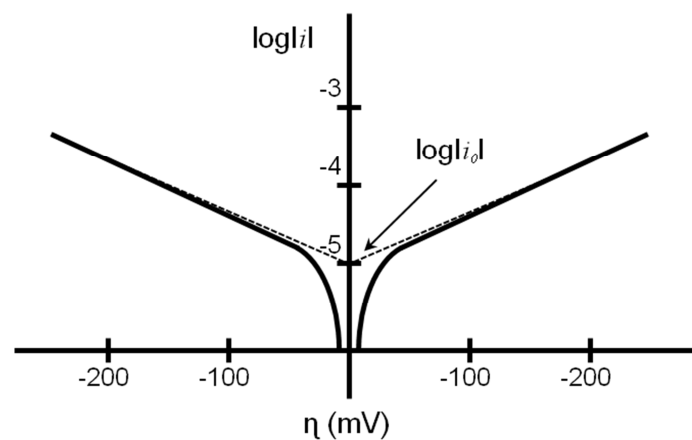


Figure 5: Tafel plot (redrawn from [12])

More specifically, the Tafel equation describes the correlation of the applied over-potential  $\eta$  to the current  $i$ , passing through the circuit. [3] [11]

$$\eta = \frac{R \cdot T}{\alpha \cdot F} \cdot \ln i_0 - \frac{R \cdot T}{\alpha \cdot F} \cdot \log i$$

[Eq. 25]

A simplified form of the equation [Eq. 25] is given by

$$\eta = a + b \cdot \log i$$

[Eq. 26]

*a and b...constants (derived of equation [Eq. 25])*

According to Figure 5 , the Tafel equation is limited by the reverse reaction at small over-potentials (<50mV) and by diffusion processes at very large over-potentials (>few hundred mV). [3] Taking into consideration that the Tafel plot is composed of an anodic branch for positive over-potentials and a cathodic branch for negative over-potentials, the transfer coefficient can be determined from the slope of the linear region of the Tafel plot as following. [3]

$$\text{reduction slope} = \frac{-\alpha \cdot F}{2.3 \cdot R \cdot T}$$

[Eq. 27]

$$\text{oxidation slope} = \frac{(1 - \alpha) \cdot F}{2.3 \cdot R \cdot T}$$

[Eq. 28]

As mentioned previously, at high current densities the charge-transfer over-potentials are negligible compared to the diffusion over-potentials. Because of that, the diffusion over-potential can be described according to the following equation. [5]

$$\eta_{diff} = \left| \frac{R \cdot T}{z \cdot F} \cdot \ln \left( 1 - \frac{j}{j_{limit}} \right) \right|$$

[Eq. 29]

*j<sub>limit</sub>...maximum current density; η<sub>diff</sub>...diffusion over-potential*

In consideration of equation [Eq. 19], a voltage, which exceeds to a certain amount of the equilibrium cell potential, is necessary to induce a current flow within the cell. The difference between cell potential and equilibrium cell potential is composed of the sum of the overpotentials of the single electrodes and the ohmic voltage drop ( $iR$ -drop). This  $iR$ -drop is caused by the current passing through the electrolyte. If a cell is on load and current flows, the cell voltage decreases, because the cell is not working reversibly and accordingly the cell is not able to provide the maximum work anymore. [13] The reduced cell voltage, caused by polarization and the internal  $iR$ -drop, can be written as follows [4]

$$E = E_0 - [(\eta_{ct})_a + (\eta_c)_a] - [(\eta_{ct})_c + (\eta_c)_c] - i \cdot R_i = i \cdot R$$

[Eq. 30]

$E_0$ ...open-circuit voltage of cell (in equilibrium);  $(\eta_{ct})_a$ ,  $(\eta_{ct})_c$ ...activation polarization or charge-transfer overvoltage at anode and cathode;  $(\eta_c)_a$ ,  $(\eta_c)_c$ ...concentration polarization at anode and cathode;  $i$ ...operating current of cell on load;  $R_i$ ...internal resistance of cell

The voltage of a cell under load is displayed in figure 6.

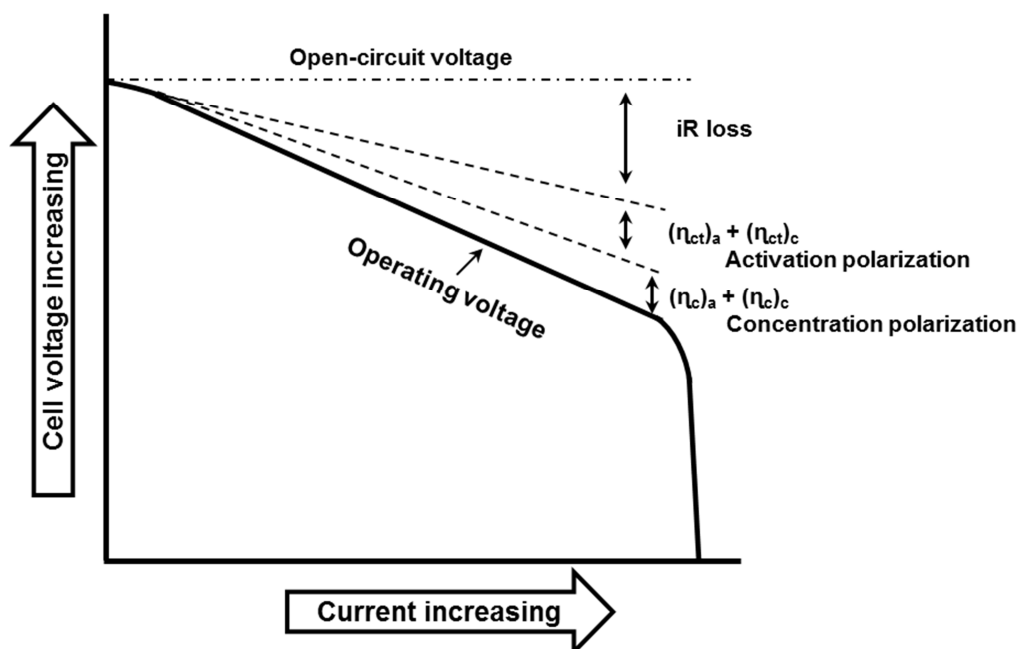


Figure 6: Cell polarization as function of operating current (redrawn from [4] [14])

Among others, factors, which influence the energy efficiency of a battery, are the electrode formulation and design, electrolyte conductivity, and the nature of the separator. Considering these factors, some rules exist in order to achieve a high operating efficiency combined with a minimal loss of energy for a battery system: [4]

- The conductivity of the electrolyte should be as high as possible in order to keep the  $iR$  polarization of the battery system low. The  $iR$ -drop due to electrolyte resistance can be further reduced by a high electrode/electrolyte interfacial area and a thin separator.
- It is of particular importance that the electrolyte salt and electrolyte solvents are electrochemically stable in order to avoid reactions with the anode and cathode material.
- Both electrode reactions should offer fast kinetics to keep the activation and the charge-transfer polarization low. The reduction of charge-transfer polarization can be achieved by a porous electrode design, thus providing a high electrode surface area and reducing the local current density.
- Furthermore, a high mass transport through the electrolyte towards and away from the electrode surface should be given, in order to avoid high concentration polarization. The mass-transfer in a battery system can be realised by proper porosity and pore sizes of the electrode, an adequate thickness and structure of the separator and a sufficient concentration of the reactants in the electrolyte.
- The current collector should consist of a material compatible with the electrode material and stable against electrolytic corrosion. The current collector design has to ensure a uniform current distribution, as well as a low contact resistance in order to minimize the electrode polarization.

## 2.3 Battery characteristics

### ***Open-circuit voltage (OCV) [V]:***

The open-circuit voltage displays the voltage realised in a battery at zero net current flow. [15]

### ***Energy density [Wh·l<sup>-1</sup>]:***

The energy density represents the achievable energy per unit volume of the cell. Its dimension depends on the density of the components and the design how the various materials are interfaced together. [16]

### ***Specific energy density [Wh·kg<sup>-1</sup>]:***

The specific energy density represents the energy per unit mass of the cell and derives from the product of the specific capacity and the operating voltage in one full discharge cycle. It can be described by the following equation [16]

$$E = \int U \cdot i \, dt$$

[Eq. 31]

*U · i dt...product of the voltage and the current over time*

### ***Power density [W·kg<sup>-1</sup>]:***

The power density of a battery represents the power per unit mass of the cell. According to LIB, at high power densities associating to higher currents, the specific energy density tends to fall off rapidly, therefore decreasing the capacity. The correlation of power density and energy density of various battery systems is shown in figure 7.

Generally, higher power density can be achieved by an increase of the effective surface area of the electrode at constant nominal area. Whereby it has to be considered that a higher effective surface may cause an increase of parasitic reactions. These parasitic reactions lead to lower cell capacity along with the shelf-life of the cell. [16]

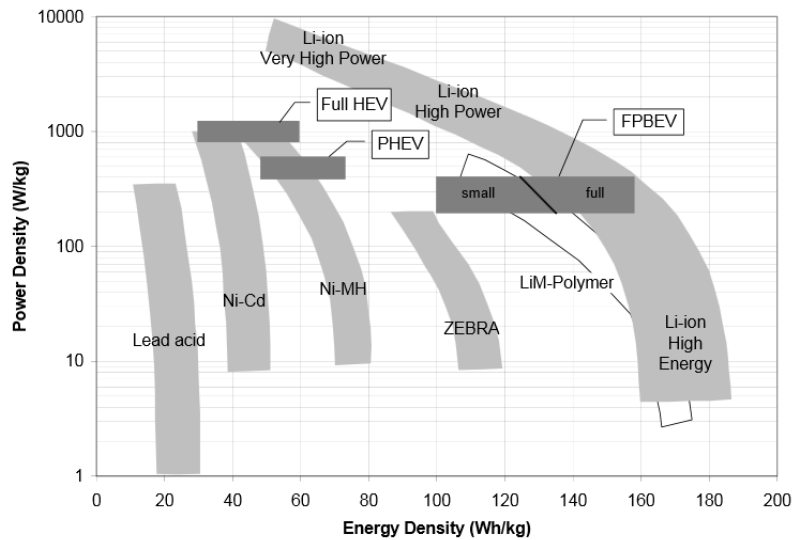


Figure 7: Illustration of Ragone plots of various battery systems [17]

### **Capacity [ $Ah \cdot kg^{-1}$ ]:**

The theoretical capacity of a battery is the total quantity of electricity, involved in the electrochemical reaction. It is directly associated with the quantity of electrons obtained from the electrochemical reactions of the active materials. [4]

### **Shelf-life [years]:**

Due to the fact that a battery must fulfil specific criteria within the first use, each battery has a limited storage period after manufacturing. Moreover, it is expected that a battery provides 90 percent of its original energy with the first load. The undesired self-discharge of a battery, even if it is not in use, is primary caused by parasitic reactions. [16].

### **Service life [hours]:**

The service life of a battery determines the time, in which a battery can be used at various loads and temperatures, before the capacity falls below an acceptable value. [16] [15]

### **Cycle life [cycles]:**

The cycle life is the number of charge/discharge cycles a battery is able to perform before it reaches 80% of the capacity. [16] [15]

## 3 Lithium-ion battery

### 3.1 Historical background of lithium-ion batteries

Since the 1990s the remarkable growth of the market for various types of portable equipments (mobile phones, lap-tops, digital cameras, etc.) mainly caused the rapid increase of the rechargeable battery market. Due to this great efforts were made for the further development of the high energy density primary lithium battery into a rechargeable battery. The successful development can be displayed in the commercialization of a rechargeable Li/MoS<sub>2</sub> battery in 1988. The initially great success of these batteries was quickly remained due to serious security hazards, caused by the use of metallic lithium as anode material. Among others, an accident in summer 1989, where a battery in a cellular phone burned during talking, was the decisive reason to replace the lithium metal as anode material by safer materials. This serious accident was attributed to an internal short circuit caused by dendritical contact of anode and cathode. These so called dendrites are formed by lithium, which is deposited in needle like structures on the surface of the anode during the charge process. [15]

Already in 1991 the company Sony Corporation was able to commercialize a safe, lithium metal-free battery. This battery was named by the company as “lithium-ion battery” (first described and published by Sony Corporation in JP02265167A2: Nonaqueous Electrolyte Secondary Battery in 1990 [18] ). [19] [20] The principle of such lithium-ion battery was first reported by M.S. Whittingham in 1976. [21] Among others the new battery was also named “rocking-chair battery” or “shuttle-cock battery”, but in the end the name “lithium-ion battery” prevailed even in scientific field. [15] This first lithium-ion battery (LIB) contained lithium cobalt oxide (LiCoO<sub>2</sub>) powders as positive active material and non-graphitized carbon as negative active material. [15] From the first commercially available lithium-ion battery to the presence, remarkable research and development was done, with special regards to new active materials, electrolytes, additives and safety management. An overview on the present state-of-the-art of LIB technologies will be provided within the following chapters.

### 3.2 Construction of a lithium-ion battery

The components of a LIB can be divided in active components, which are involved in the electrochemical process, and inactive components, which are not involved. The three key components of the LIB are the positive active material, the negative active material and the electrolyte. The remaining components of the system, like separator, current collectors, battery case, etc., are essential components for an adequate function of a battery. Although they are not involved in the electrochemical process, they still affect the battery performance.

In figure 8 the working principle of a lithium-ion battery is schematically illustrated. Considering a lithium-ion battery with graphite anode (negative active material) and  $\text{LiCoO}_2$  cathode (positive active material), both active materials are able to intercalate lithium-ions reversibly. Moreover, during the charge process of a LIB lithium-ions deintercalate from the cathode, migrate through the electrolyte and intercalate in the graphite anode. The extraction of lithium-ions from the cathode is directly related to the release of electrons at the cathode into the external circuit. These electrons move to the anode. The reverse of the before described processes takes place during the discharge of a LIB. [22] [23]

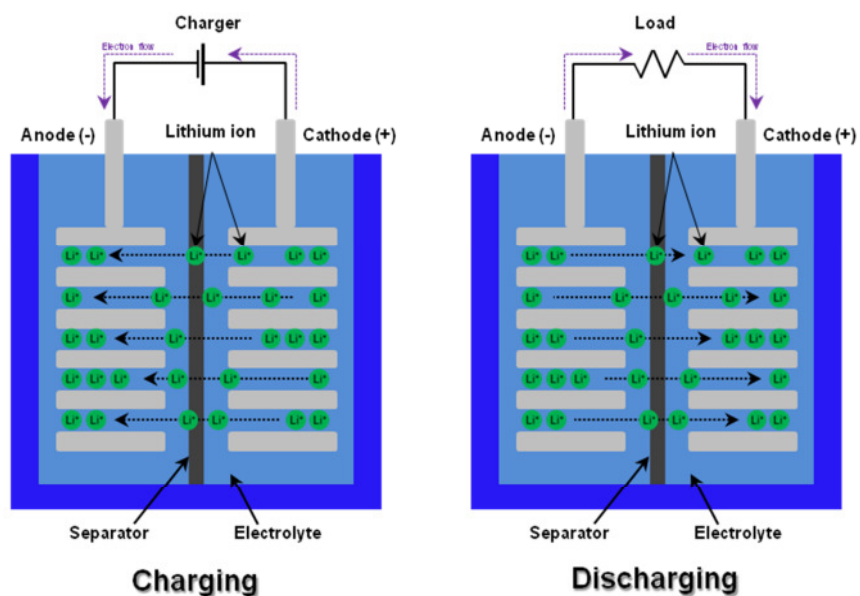


Figure 8: Schematic illustration of the working principle of a lithium-ion battery (redrawn from [24])

In general, LIBs are commercially available in cylindrical (small and large), prismatic and pouch formats. These three cell types are displayed in figure 9. It is important to note that the choice of the cell format depends on its application. A comparison of advantage and disadvantages of the various cell formats is represented in table 1. [25]

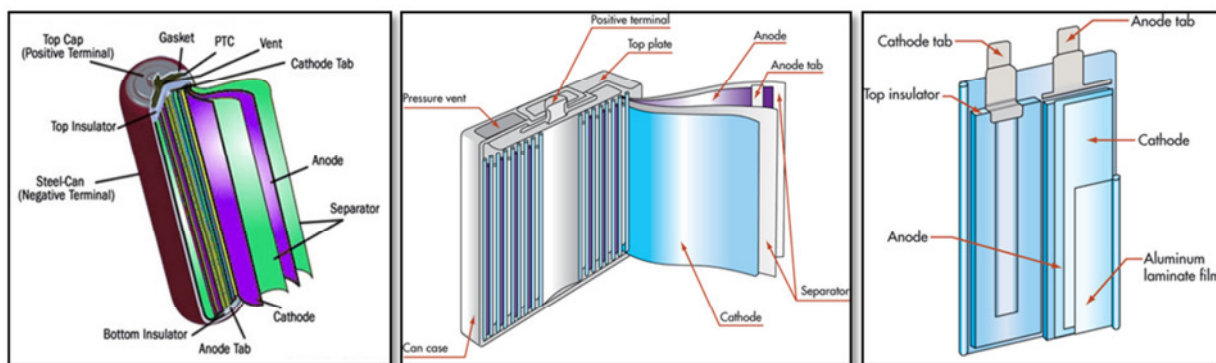


Figure 9: Cylindrical [26] (left), prismatic (middle) [27] and pouch (right) [27] format of lithium-ion batteries

Table 1: Comparison of available LIB cell formats (redrawn from [25])

	Small Cylindrical	Large Cylindrical	Prismatic	Pouch
Shape	Encased in a metal cylinder, usually 65 mm long	Encased in a metal or hard plastic cylinder	Encased in semihard plastic case	Contained in a soft bag
Connections	Welded nickel or copper strips or plates	Threaded stud for nut or threaded hole for bolt	Threaded hole for bolt	Tabs that are clamped, welded, or soldered
Retention against expansion when fully charged	Inherent from cylindrical shape	Inherent from cylindrical shape	Requires retaining plates at ends of battery	Requires retaining plates at ends of battery
Appropriateness for production runs	Good: welded connections are reliable	Good	Excellent	Good: high performance
Field replacement	Not possible	Possible but not easy	Easy	In general not possible
Notes	Best for retrofits, as small shape can be fit in all available space	Not widely available	Best availability, very little design effort required	High energy/power density (by themselves); significant design effort required: only appropriate for large production runs

### 3.3 Active materials for lithium-ion batteries

According to the equation [Eq. 31], the specific energy density of LIBs depends on the theoretical capacities of the electrode materials, as well as of the cell potential achievable by these materials. In summary, the intrinsic characteristics of the cell containing negative active material (anode) and positive active material (cathode) influence the energy, capacity and cell potential of a given battery system. Furthermore, the cycle life and safety of a LIB are directly related to the nature and stability of the electrode-electrolyte interfaces, as well as to the structural stability of the active materials. [15] In order to maximize the cell potential of the battery the anode potential should be as low as possible while the cathode potential should be as high as possible. Commercial LIBs mainly contain  $\text{LiCoO}_2$  with an average discharge potential of 3.9 V versus metallic lithium as cathode material. This material is combined with graphite as anode material, which provides a potential of <1 V versus metallic lithium. [28]

Figure 10 gives an overview on active materials for LIBs, summarizing state-of-the-art materials and future materials. More specifically, the figure displays the potential of positive and negative active materials plotted versus their theoretical capacities. In order to maximize the cell voltage, the 5 V positive active materials are more advantageous than the commercially used  $\text{LiCoO}_2$ , due to the higher positive potential versus metallic lithium. But it has to be considered that a commercial use of these 5 V materials is only conceivable in case of long-term stability of both, the electrolyte and the cathode material at this high potential. At the present time poor electrolyte and cathode material stability strongly affects the battery safety and thus its usability. [28]

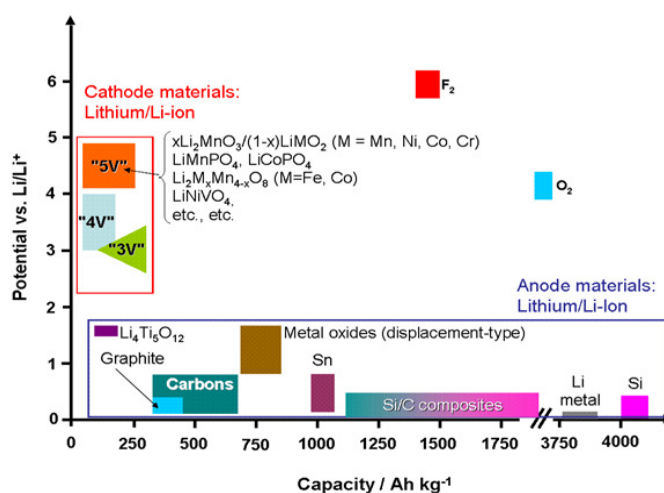


Figure 10: Potentials and theoretical capacities of negative and positive active materials for LIBs [29]

Comparing the theoretical capacity of graphite with  $372 \text{ mAh}\cdot\text{g}^{-1}$  and metallic lithium with  $3860 \text{ mAh}\cdot\text{g}^{-1}$ , it becomes obvious that the replacement of the metallic lithium anode material by the insertion material graphite caused a very high loss of the total battery system's energy density. [28] But due to the serious safety issue caused by formation of dendrites, it was necessary to find an alternative to metallic lithium. These dendrites are able to grow from the anode to the cathode surface and cause thereby internal short circuits between the electrodes. Furthermore, the dendritically-grown lithium may dissolve from the anode surface and subsequently exist as electrochemically isolated "dead lithium" in the LIB system (Figure 11).

A lithium-ion permeable passivation layer on the surface of the metallic lithium avoids an oxidation of the metal, which is, due to its high reactivity, unstable in all commonly known organic solvent-based electrolytes. The formation of a protective surface film can be observed for both, negative and positive active materials and is described in more detail in chapter 3.4.2. [15]

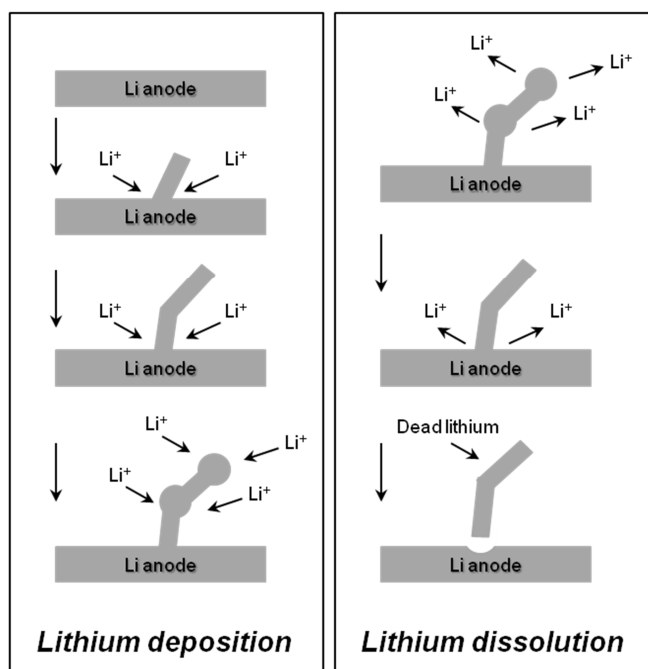
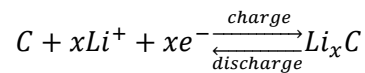


Figure 11: Possible mechanisms for lithium deposition and dissolution (redrawn from [5])

### 3.3.1 Negative active materials: Carbonaceous-based insertion materials

As mentioned before, in 1991, the first 4 V class rechargeable LIB, with carbon as negative electrode and  $\text{LiCoO}_2$  as positive electrode was commercialized. In this time, low-crystalline carbon-based materials were used, but nowadays anode materials mainly consists of synthetic or natural graphitic carbon due to the higher achievable capacity. [30] [31] [32] [33]

Considering that lithium-ions can be reversibly intercalated into most carbonaceous materials during the charge and discharge process, these materials are ideal for anode materials. The intercalation and deintercalation process is described by the following reaction equation.



[Eq. 32]

Generally, carbonaceous negative active materials for LIBs are divided in two groups, the graphitic and the non-graphitic (disordered) carbons.

The graphitic carbons have a layered structure and are constructed of hexagonal sheets of  $\text{sp}^2$ -hybridized carbon atoms, which are also called graphene sheets. Along the c-axis, these graphene sheets are weakly bonded together by Van-der-Waals forces in an AB stacking order (Figure 13). Furthermore, these graphitic carbons can be divided in natural and artificial graphites. Artificial graphites are synthesized by a treatment of pyrolysed carbons at temperatures around 3000 °C. [30]

The group of non-graphitic carbons can be distinguished between graphitizable (soft carbon) and non-graphitizable (hard carbon) carbons. Whereby, non-graphitic carbons have mainly a planar hexagonal carbon atoms network without far-reaching crystallographic order in c-direction. This arrangement leads to material structures with amorphous areas cross-linked with graphitic areas. Non-graphitic carbons are mainly synthesized by heat treatment of pyrolysed organic polymers at temperatures from ~1500 to ~3000 °C, or of hydro-carbon precursors at temperatures below ~1500 °C. [33] An example for soft and hard carbon structures is displayed in figure 12. In contrast to hard carbons, soft carbons develop graphite structure during the heating process. This is possible because the structure segments of soft carbons are mobile enough to form graphite-like crystallites as crosslinking

between them is weak. [34]. In case of hard carbons the carbon layers are immobilized by strong crosslinking and therefore, they develop no graphite structure, not even at high temperature (2500-3000 °C). [34] [33] [30] [32]

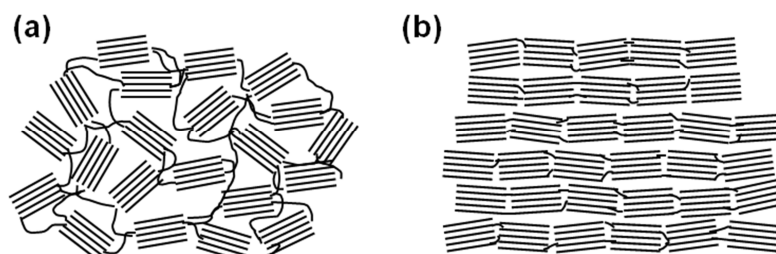


**Figure 12: Schematic illustration of (a) hard (non-graphitizable) and (b) soft (graphitizable) carbons (redrawn from [35] [36])**

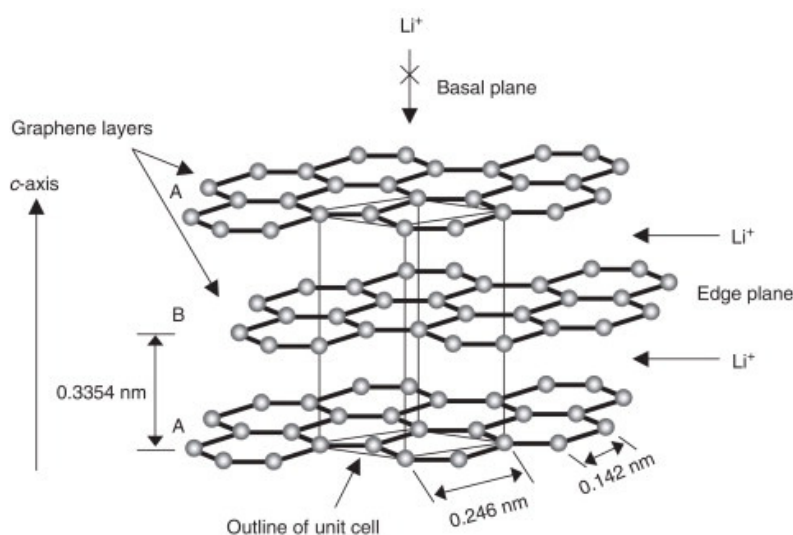


**Figure 13: Schematic illustration of the crystal structure of hexagonal graphite showing AB layer stacking sequence and the corresponding unit cell [30]**

If lithium-ions intercalate between the graphene sheets of the graphite, the so called lithium-graphite intercalation compounds (Li-GICs) are formed. These intercalation processes of lithium-ions occur stepwise, leading to a gradual formation of a periodic array of unoccupied layer gaps at low concentration of intercalates. Such stage formations of Li-GICs are schematically illustrated in figure 14. According to figure 14, the maximum of lithium-ion intercalation is reached at the formation of stage I Li-GIC ( $\text{LiC}_6$ ). Based on this, a theoretical capacity of  $372 \text{ mAh}\cdot\text{g}^{-1}$  can be achieved, which comes along with an anisotropical volume expansion of approximately 10 %. [33] [30]

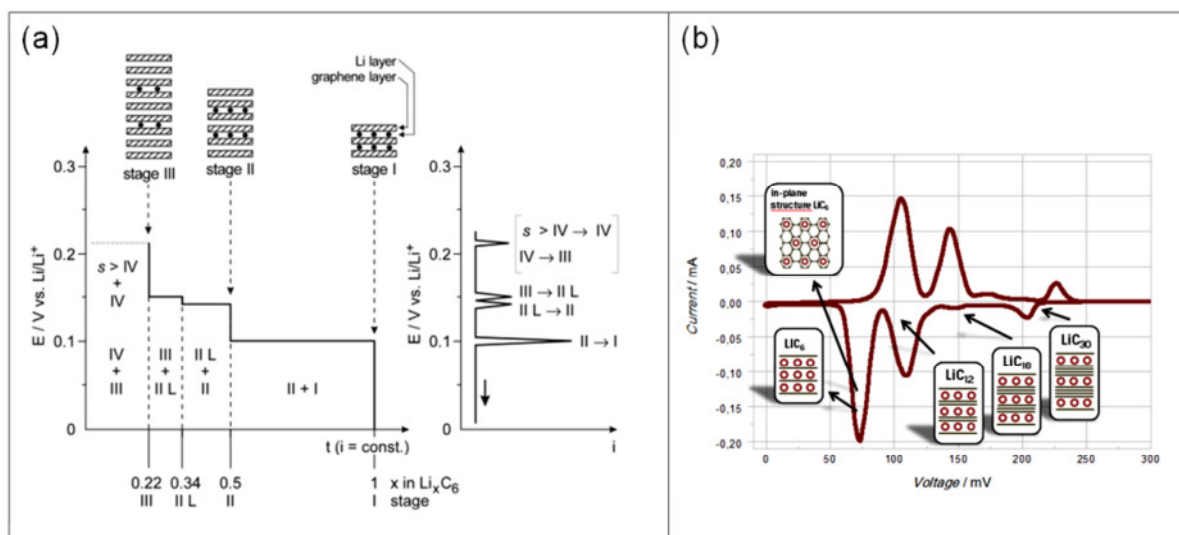
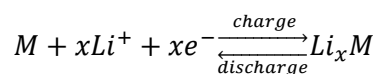


Figure 14: (a) Stage formation and structure of lithium-graphite intercalation compounds [33] [37] and (b) cyclic voltammogram of lithium intercalation into highly crystalline graphite [38]

### 3.3.2 Negative active materials: Lithium alloys

Further candidates for negative active materials in LIBs were found in form of metals  $M$  ( $M = \text{Si}, \text{Sn}, \text{Al}, \text{Ge}, \text{Sb}, \text{As}, \text{Zn}, \text{etc.}$ ), as they are able to form well-defined intermetallic phases ( $\text{Li}_x\text{M}$ ) with lithium at room temperature. The formation of such intermetallic phases is only possible, if the metal is polarized to a sufficiently negative potential in a lithium-ions containing liquid organic electrolyte. The lithiation and delithiation process of a metal  $M$  is given by the following reaction [39]



[Eq. 33]

The commonly used carbon-based insertion compounds like graphite ( $\text{LiC}_6$ ) show significant lower gravimetric as well as volumetric capacities, compared to lithium alloys (Figure 15). This lithium alloys allow to achieve packing densities  $\text{PD}_{\text{Li}}$  in range of the metallic lithium  $\text{PD}_{\text{Li}}$  or even slightly higher. [39]

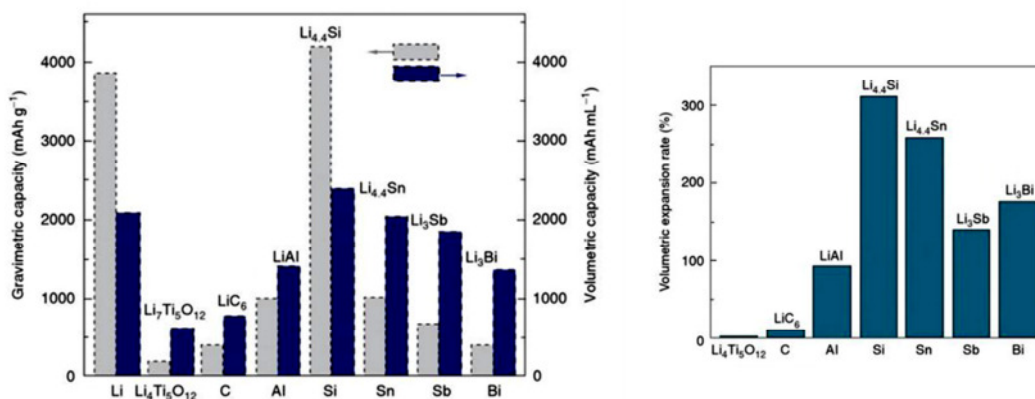


**Figure 15: (left) gravimetric and volumetric capacity of various full lithiated negative active materials (volume expansion but no lithium weight is included) and (right) volumetric expansion rates of these full lithiated materials [40]**

Actually, the remarkable high capacities of lithium alloys make them ideal candidates for negative electrodes and should allow an improvement of the battery performance. But the enormous structure and volume changes of these materials during the lithium alloying and dealloying processes prevent any commercial use until now. The volume expansion rates of lithium alloys are in the order of 100 to 300 % (Figure 15) and mainly caused by the additionally gain of negative charges to the lithium-ions. Due to the gain of electrons by the neutral host metal atoms  $M^0$ ,  $M^{x-}$  ions are formed according to the charge transfer reaction  $M^0 + xe^- \leftrightarrow M^{x-}$ . The resulting  $M^{x-}$  ions are remarkably larger than the neutral  $M^0$  atoms. Furthermore, the formed  $Li_x^+M^{x-}$  phases possess a highly ionic character and are more brittle than the unlithiated metal host. [39] [41] [42]

According to the described facts above, the high volume changes of lithium alloys is attached to high mechanical stresses. This results in a rapid decrease of the mechanical stability of the electrode, ending up in pulverisation of the electrode. Consequently the active material particles lose their electrical contacts. [39] [43] [44] [33]

### 3.3.2.1 Lithium alloys: Silicon

As mentioned before, silicon is able to form an alloy with lithium. Within the first investigation of this metal, the formation of the following silicon-lithium phases during the alloying process (at 415°C) was observed: [45] [2]

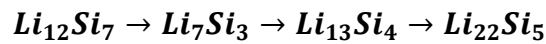


Table 2: Stoichiometry and potential range E (open circuit voltage/electromotive force) of the four Li-Si phases (at 415°C), plotted in Figure 16 [46]

Stoichiometry		Potential range (OCV) [mV]
$Li_{12}Si_7$	$Li_{1,71}Si$	332-288
$Li_7Si_3$	$Li_{2,33}Si$	288-158
$Li_{13}Si_4$	$Li_{3,25}Si$	158-44
$Li_{22}Si_5$	$Li_{4,4}Si$	44-2

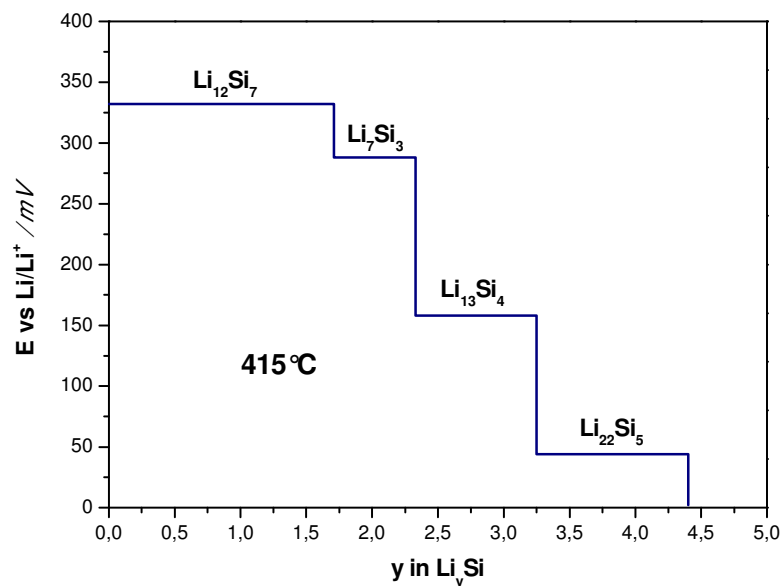


Figure 16: Coulometric titration curve for the lithium-silicon system at temperature of 415°C (redrawn from [46])

According to table 2 and figure 16, the fully lithiated  $\text{Li}_{22}\text{Si}_5$  phase, with a theoretical capacity of  $4200 \text{ mAh}\cdot\text{g}^{-1}$ , is achieved, if each silicon atom accommodates 4.4 lithium atoms. Recently, Obrovac and Krause et al. [47] showed that the fully lithiated silicon is only able to form a  $\text{Li}_{15}\text{Si}_4$  phase at room temperature and not the  $\text{Li}_{22}\text{Si}_5$  phase, as it is popular belief. In contrast to the  $\text{Li}_{22}\text{Si}_5$  phase, the  $\text{Li}_{15}\text{Si}_4$  phase only allows to achieve a capacity of  $3579 \text{ mAh}\cdot\text{g}^{-1}$ . [47] [48] [49] Moreover, during the formation of  $\text{Li}_{15}\text{Si}_4$  phase, silicon undergoes a volume expansion of  $\sim 280\%$  [47]. [50]

In the following some approaches to compensate the high volume changes during the alloying/dealloying process with lithium, will be presented: [2]

➤ ***Reduction of the silicon particle sizes:***

The decrease of the particle sizes into nano-scale range results in lower absolute volume change and thereby the electrode performance can be improved. [51] [52] [50]

➤ ***Embedding of the silicon particles into an inactive matrix:***

An approach to compensate the huge volume expansion of silicon during the lithiation process is to embed the silicon particle in an inactive matrix. The inactive matrix of these composite materials is responsible for avoiding the pulverisation of the electrode by buffering destabilizing volume changes of the silicon particles. The inactive matrix should possess high mechanical strength to resist the volume expansion of the reactive phase during the cycling. Furthermore, it should guarantee high electrical conductivity in order to enable the charge transfer. [2] Some examples for such inactive matrix compounds are TiN [53],  $\text{TiB}_2$  [54], SiC [55], TiC [56], etc. Another category of composite materials, where the inactive host matrix is formed during the lithiation process, are  $\text{FeSi}_2$ ,  $\text{NiSi}_2$ ,  $\text{SiB}_3$ ,  $\text{CoSi}_2$  [57],  $\text{CaSi}_2$  [58],  $\text{SiO}_x$  [59] etc. [2]

➤ ***Embedding of the silicon particles into an active matrix:***

The beneficial of an active matrix compared to an inactive one is the prevention of decreasing theoretical specific charge capacity and density due to increasing inactive mass. [39] In contrast to the inactive matrix, the active matrix is also able to react with lithium. But the active matrix is either less reactive or, due to good mechanical strength and ductility, able to compensate the volume changes of the reactive phase. One of such multiphase composite materials with two active materials, wherein one is less reactive, is represented by the Sn/SnSb composite material. The principle of the

Sn/SnSb composite material is based on the different potential, when the alloying starts to take place. In this context, the less reactive Sn phase (~650 - 700 mV vs Li/Li<sup>+</sup>) is able to buffer the volume expansion of the more-reactive SnSb phase (~800 - 850 mV vs Li/Li<sup>+</sup>) during its lithium alloying process. [39] [43] [44]

Further promising composite materials are Silicon/Carbon (Si/C) composites. Due to the softness, relatively low mass, good electrical conductivity, adequate lithium insertion ability and the small volume expansion rate of carbon, it presents an appropriate active matrix. Regarding to Si/C composite materials a lot of research has been done. Whereby, mainly Si/C composite materials consist of silicon embedded/coated with pyrolysed polymer precursors [60] [61] [60] [62], silicon graphite embedded/coated with carbon matrix (formation of carbon matrix with pyrolysed polymer precursors or chemical/thermal vapor deposition) [63] [64] and pure silicon graphite electrodes [65] [66] are reported in literature. [2]

➤ ***Improvement by use of an optimal binder for Si electrodes:***

Generally, the binder in an electrode is responsible for proper particle conductivity and the binding of the particles to the current collector. Today, mainly thermoplastic Polyvinylidene difluoride (PVdF) binders are used for anode fabrication. The low ductility and the interaction of this weakly polar binder with polar solvents lead to swelling and the decrease of its binding ability. Due to these facts, the binder is only suitable for graphite active materials with low volume expansion. Due to the high volume expansion of silicon during the lithiation and delithiation processes, the use of PVdF binder is not advisable. [40] Therefore, intensive research was performed to find new types of binder, with the focus on a low swelling character and elevated binding strength. A significant improved cycle life of silicon based electrodes was reported by the use of a mixture of styrene butadiene rubber (SBR) and sodium carboxy methyl cellulose (Na-CMC) [67] [68] and pure Na-CMC binder [69] [70].

### 3.3.3 Positive active materials

Positive active materials can be roughly divided in the type of lithium-ion diffusion and the working potential of each material. According to the structure, the types of lithium-ion diffusion are divided in 1-dimensional (e.g.  $\text{LiFePO}_4$  olivine-type), 2-dimensional (e.g.  $\text{LiCoO}_2$  layered-type) and 3-dimensional (e.g.  $\text{LiMn}_2\text{O}_4$  spinel-type) materials. Furthermore, the potentials of such materials can be subdivided in 3V, 4V and 5V areas (Figure 10). [33]

In general, a high positive potential for positive materials is desirable due to the enhanced cell energy. Nowadays the increase of potential is limited by the stability of known electrolytes.

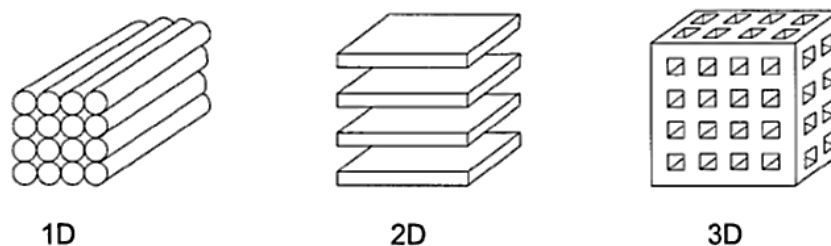


Figure 17: Schematic illustration of 1-, 2- and 3-dimensional Li-host materials [33]

#### 3.3.3.1 Layered transition metal oxides $\text{LiMO}_2$

The  $\alpha\text{-NaFeO}_2$ -type structure of layered transition metal oxides  $\text{LiMO}_2$  ( $M=\text{Co}, \text{Ni}, \text{Fe}, \text{Cr}, \text{V}$ ), such as  $\text{LiCoO}_2$  and  $\text{LiNiO}_2$ , allows 2D delithiation and lithiation of lithium-ions. According to figure 18, the lithium-ions are located in octahedral coordination between the  $\text{MO}_2$  layers within these materials. This leads to alternating (111) planes and a slightly hexagonal distortion of the lattice. A full delithiation results in the formation of a thermodynamically unstable  $\text{CdCl}_2$  structure. [71] [33] The delithiation/lithiation of  $\text{LiMO}_2$  materials is given by the following reaction equation.



[Eq. 34]

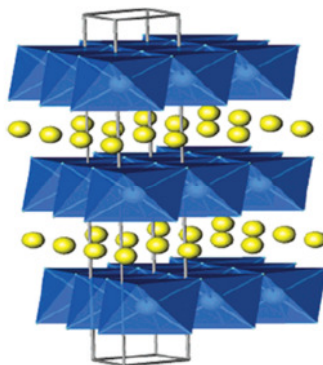


Figure 18: 2D layered structure of  $\text{LiMO}_2$  ( $\alpha\text{-NaFeO}_2$ -type) [72]

#### Lithium cobalt oxide $\text{LiCoO}_2$ :

$\text{LiCoO}_2$  represents the most widely used positive active material for lithium-ion batteries. It provides a working voltage of 3.5 - 4.2 V (vs.  $\text{Li/Li}^+$ ) and a gravimetric theoretical capacity of  $\sim 140 \text{ mAh}\cdot\text{g}^{-1}$ . Overcharging of this material to potential of 5.2 V (vs.  $\text{Li/Li}^+$ ) causes the formation of the thermodynamically unstable cobalt(IV)oxide  $\text{CoO}_2$ , which decomposes under oxygen release to lower cobalt oxides. [71] In summary, only  $x=0.5$  lithium-ions per  $\text{Li}_{1-x}\text{CoO}_2$  can be reversibly extracted. Further extractions lead to a structure distortion from hexagonal to monoclinic and accordingly potential is limited to 4.2 V ( $\text{Li}_{0.5}\text{CoO}_2$ ). [28]

#### Lithium nickel oxide $\text{LiNiO}_2$ :

With around 4 V (vs.  $\text{Li/Li}^+$ )  $\text{LiNiO}_2$  provides a slightly lower redox-potential than  $\text{LiCoO}_2$ , while the theoretical capacity is about 30 % higher. A serious safety hazard of this material is based on an exothermic oxidation of the collapsing delithiated  $\text{Li}_x\text{NiO}_2$  with the organic electrolyte. Because of this, the cell voltage has to be limited below 3.6 V (vs.  $\text{Li/Li}^+$ ). [71]

#### Lithium oxide solid solution $\text{Li}(\text{Ni}_{1-y-z}\text{Mn}_y\text{Co}_z)\text{O}_2$ :

To stabilize the  $\text{LiMO}_2$  structure as well as to reduce the expensive cobalt content, composite materials like  $\text{Li}(\text{Ni}_{0.3}\text{Mn}_{0.3}\text{Co}_{0.3})\text{O}_2$ , were introduced. At the fully lithiated state of these compounds, cobalt is trivalent, nickel predominantly divalent and manganese tetravalent. In case of this material mainly nickel is electrochemically active and only at later stages cobalt is active as well. Manganese doesn't participate in the electrochemical process, but it's responsible for the structural stabilisation. A very promising compound, which is already commercially available, represents the material  $\text{Li}(\text{Ni}_{0.3}\text{Mn}_{0.3}\text{Co}_{0.3})\text{O}_2$ . [72]

### 3.3.3.2 Spinel type compound $\text{LiMn}_2\text{O}_4$

Due to the structure of the lithium manganese spinel  $\text{LiMn}_2\text{O}_4$  material a 3-dimensional lithium-ions intercalation/deintercalation is possible, resulting in fast insertion processes. [71] A reversible lithium extraction occurs at around 4 V (vs.  $\text{Li}/\text{Li}^+$ ). [33]  $\text{LiMn}_2\text{O}_4$  has a gravimetric theoretical capacity of 100 - 120  $\text{mAh}\cdot\text{g}^{-1}$ . [71] Additional to the reversible insertion and extraction of lithium-ion in the 4 V region, where the cubic symmetry of the structure is retained, this material undergoes a further structure-destructive lithium-ions insertion/deinsertion in the 3 V region. This asymmetric lattice expansion is attributed to the Jahn Teller effect of the  $\text{Mn}^{3+}$  ion, which causes a transformation of the cubic crystal into a tetragonal symmetry. A further disadvantage of this material is the dissolution of manganese ( $\text{Mn}^{2+}$ ) within the electrolyte, caused by overcharging or use at elevated temperatures. The dissolved ions are able to poison the negative electrode in the cell system. [33] [71]

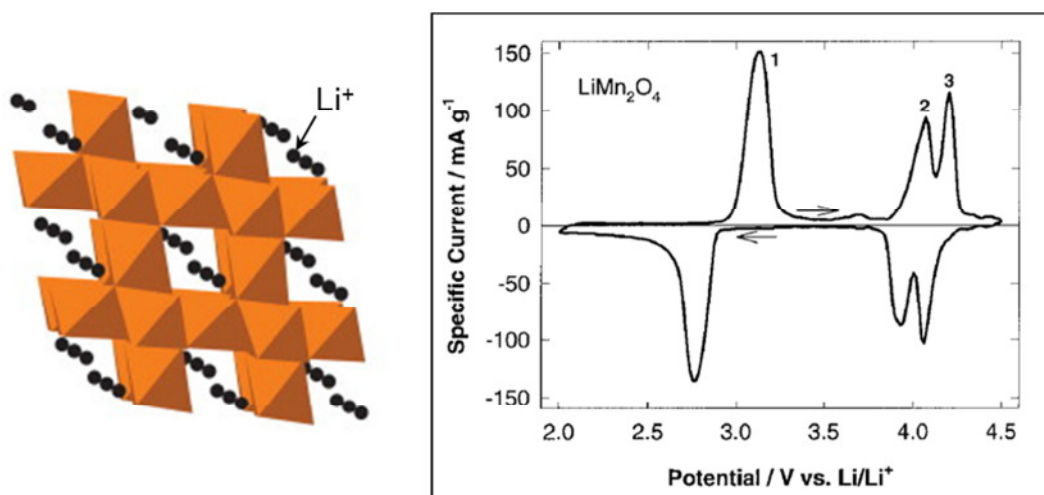


Figure 19: (left) Schematical illustration of  $\text{LiMn}_2\text{O}_4$  structure [71] and (right) cyclic voltammogram of  $\text{LiMn}_2\text{O}_4$  [33]

### 3.3.3.3 Olivine type compounds $\text{LiMPO}_4$

#### Lithium iron phosphate $\text{LiFePO}_4$ :

$\text{LiFePO}_4$  is a low cost, long life and environmental-friendly material with a discharge potential around 3.45 V (vs.  $\text{Li}/\text{Li}^+$ ) (for bulk  $\text{LiFePO}_4$  [22]) and a gravimetric theoretical capacity of 170  $\text{mAh}\cdot\text{g}^{-1}$ . [73] The olivine structure of  $\text{LiFePO}_4$  (Figure 20) contains slightly distorted hcp anion oxygen arrays with half of the octahedral sites occupied by Fe and

one eighth by Li. [22] In literature three different paths of lithium diffusion into the  $\text{LiFePO}_4$  host, with a favoured diffusion along b-axis were proposed. [74] [75] [76] Furthermore, in 2008 it was reported by S. Nishimura et al. [77] that the lithium diffusion path along the (010) is a curved one dimensional chain. [22] Generally,  $\text{LiFePO}_4$  shows an excellent thermal and chemical stability compared to  $\text{LiCoO}_2$ . The poor rate capability of this material is caused by the low 1D ionic and electrical conductivity. To improve this low conductivity the following approaches are used: [22] [71]

- Surface modification (i.e. particle coating with conductive film)
- Size modification (a decrease of particle sizes lead to shorter lithium-ion diffusion length)
- Doping with other metal ions (either Li or Fe sites)

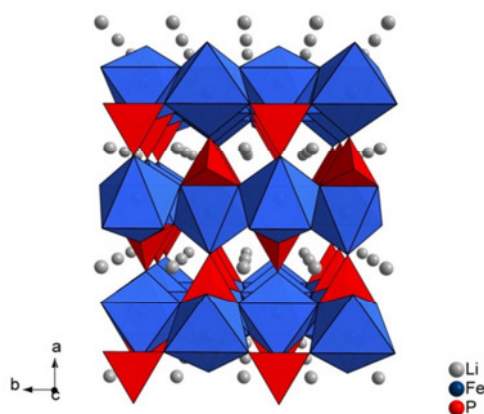


Figure 20: Schematical illustration of the  $\text{LiFePO}_4$  structure (1D mobility of  $\text{Li}^+$ ) [78]

#### High voltage $\text{LiCoPO}_4$ and $\text{LiNiPO}_4$ materials:

Due to the remarkable potentials of 4.8 V (vs.  $\text{Li}/\text{Li}^+$ ) in case of  $\text{LiCoPO}_4$  [79] and 5.1 V (vs.  $\text{Li}/\text{Li}^+$ ) in case of  $\text{LiNiPO}_4$  [80], these materials would represent ideal candidates for LIB cathodes. Unfortunately the improved battery energy density by the use of these materials is nowadays prohibited due to the fact that no stable electrolytes in this voltage region are available. [73]

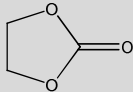
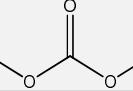
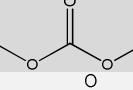
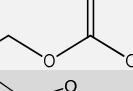
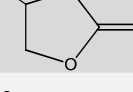
### 3.4 Nonaqueous liquid electrolytes for lithium-ion batteries

As mentioned before, the electrolyte has the important function to ensure the charge transfer ( $\text{Li}^+$ ) between the negative and positive electrode. Commonly used electrolytes are composed of one (or more) lithium salt, which is dissolved in a mixture of two or more organic solvents. [81] A mixture of organic solvents is primary necessary in order to fulfil the following requirements for electrolyte solvents: [81]

- First of all, the solvent should possess a high dielectric constant to solve lithium salt in dissociated form in adequate concentration.
- Furthermore, a low viscosity is demanded to support the ion transport.
- Generally, the solvent should be inert against all cell components, with special regard to the charged surfaces of anode and cathode.
- The melting point should be as low as possible and the boiling point as high as possible in order to maintain the liquid state of the solvent in a wide temperature range.
- The solvent has to be safe (high flash point), nontoxic and economical.

Nowadays, these requirements are realised within a mixture of cyclic and linear esters or ethers. While cyclic and linear ethers have similar moderate dielectric constants and low viscosities, completely different properties are shown by cyclic and linear esters. Cyclic esters such as ethylene carbonate (EC) possess high dielectric constants as well as high viscosities. The opposite properties can be observed for linear esters, as they are less polar but more fluid. [71] [81] Some commonly used solvents for LIBs are shown in table 3.

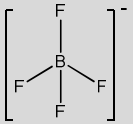
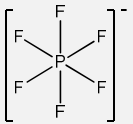
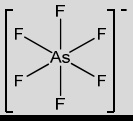
Table 3: Organic solvent used for LIB electrolytes [81] [82]

Solvent	Structure	$T_m$ (°C)	$T_b$ (°C)	$\eta$ (cP) 25 °C	$\epsilon$ 25 °C	$T_f$ (°C)	
Ethylene carbonate	EC		36.4	248	1.90 (40 °C)	89.78	160
Dimethyl carbonate	DMC		4.6	91	0.59 (20 °C)	3.107	18
Diethyl carbonate	DEC		-74.3	126	0.75	2.805	31
Ethylmethyl carbonate	EMC		-53	110	0.65	2.958	/
Propylene carbonate	PC		-48.8	242	2.53	64.92	132
Dimethoxyethane	DME		-58	84	0.46	7.2	0

$T_m$ ...melting point;  $T_b$ ...boiling point,  $\eta$ ...viscosity;  $\epsilon$ ...dielectric constant;  $T_f$ ...flash point

Due to the excellent dissolution and dissociation properties in nonaqueous solvents and the ability to passivate the positive electrode surfaces and current collectors, lithium salts with fluorine anions are the most commonly used conductive salts in LIBs. In this context, especially lithium hexafluorophosphate ( $\text{LiPF}_6$ ) has to be mentioned. Big disadvantages of these lithium salts are the high moisture-sensitivity, as well as the rising reactivity at elevated temperature. [82] In table 4, some examples for conductive salts are listed.

Table 4: Conductive salts used in LIB electrolytes [81] [82]

Solvent	Structure	$T_m$ (°C)	$T_{\text{decomp.}}$ (°C) in solution	$\sigma$ (mS $\text{cm}^{-1}$ , 1.0 mol $\cdot$ l $^{-1}$ , 25 °C)		$E_{\text{ox}}$ (V)*	
				in PC	in EC/DMC		
Lithium tetrafluoroborate	$\text{LiBF}_4$		293 (d)	>100	3.4	4.9	4.7
Lithium hexafluorophosphate	$\text{LiPF}_6$		200 (d)	~80	5.8	10.7	4.65
Lithium hexafluoroarsenate	$\text{LiAsF}_6$		340	>100	5.7	11.1	4.7

$T_m$ ...melting point;  $T_{\text{decomp.}}$ ...decomposition point;  $\sigma$ ...conductivity;  $E_{\text{ox}}$ ...anion oxidation potential; (d)...decomposition without melting; \*...vs.  $\text{Li/Li}^+$  on porous carbon electrode in EC/DMC ( $\text{Et}_4\text{N}^+$  salt)

In addition to the solvents and salt also additives can be found in common electrolytes. They can mainly be classified in agents for optimized anode SEI formation, for cathode protection, for overcharge protection and others. [83]

### 3.4.1 Separators

A separator fulfils primarily two functions. Firstly, it is responsible for the storage of the electrolyte, which ensures the ion transfer and secondly, it gurantees the separation of the positive and negative electrode. Summarizing, a separator material has to possess the following properties:

- 1) Electrically insulating
- 2) Affinity to the electrolyte
- 3) Microporous structured

Due to the fact that the LIB contains active lithium compounds, flammable organic solvents and is able to achieve high energy densities, the separator has additionally to fulfil the following demands regarding to safety: [84]

- **chemically stable** against the electrolyte components and electrochemically inert during the charge and discharge processes and unreactive against side reaction products (i.e. decomposition components).
- **mechanically stable** against internal and mechanical stresses, resulting in the cell assembling process (Separator is positioned between positive and negative electrode and subsequently wound together to form a jelly roll).
- **thin** in order to increase the cell capacity and to minimize the cell impedance.
- **the ability of current shutdown** to prevent a possible unsafe battery mode (thermal runaway). The separator closes the microporous structure at defined temperature, which leads to a current flow cut. Additionally, the separator has to maintain its dimension and strength to prevent an electrical contact of both electrodes.
- **a satisfying electrolyte holding-capacity** to avoid an electrolyte depletion.

In commercial lithium-ion batteries primary thin (<math><30\ \mu\text{m}</math>), microporous, polyolefin membranes are used. They are made of polyethylene (PE), polypropylene (PP) or laminates of polyethylene and polypropylene. The porosity of commercial membranes is around 30 - 50 %, with pore sizes in the range of 0.03 - 0.1  $\mu\text{m}$ . Generally, the melting point of PE ( $m_p = 135\ \text{°C}$ ) and PP ( $m_p = 165\ \text{°C}$ ) is different, which is exploited in multilayer separators. In a trilayer PP/PE/PP material [85], like it was developed by Celgard, PE acts with its lower melting point as current shutdown fuse. The PP layers, with their higher melting point, are responsible to maintain the shape of the separator to prevent a contact between the electrodes and the resulting internal short circuit. [86]

### 3.4.2 Electrolyte/electrode interphases

Due to the wide operating potential of LIBs an oxidative as well as reductive decomposition of electrolytes take place. The decomposition of electrolyte leads to the formation of passivating layers on the electrode surfaces. These passivating layers prevent further decomposition of the electrolyte. In figure 21 electrochemical processes are shown, which can occur on the surface of a gold electrode in a Li-salt/alkyl carbonate solution ( $\text{LiClO}_4/\text{PC}$ ). [87]

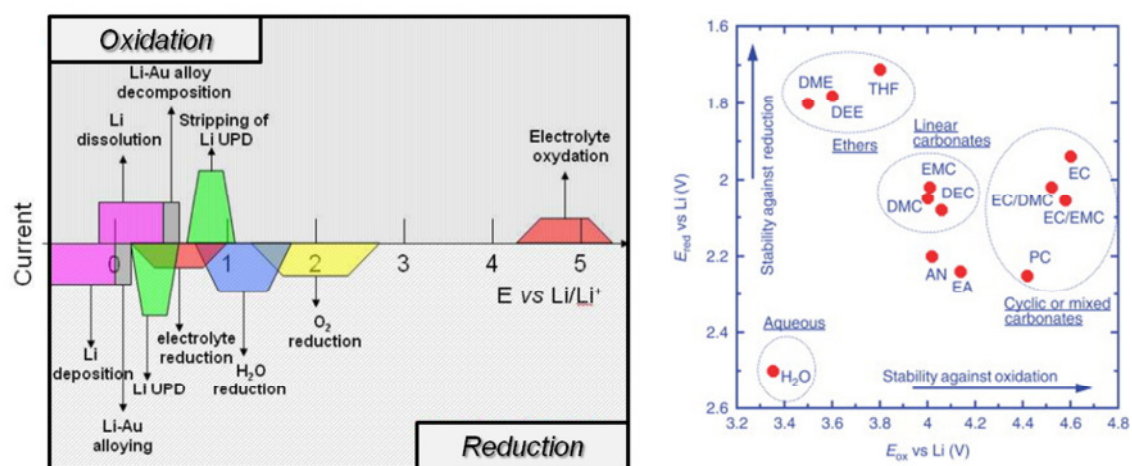
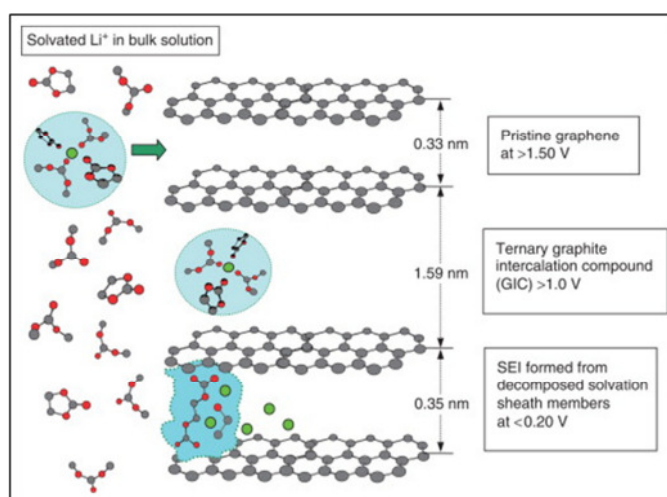


Figure 21: (left) Schematic illustration of oxidative and reductive reactions taking place on Au electrode in Li-salt/alkyl carbonate solution ( $\text{LiClO}_4/\text{PC}$ ) depending on the applied potential [87] and (right) electrochemical stability window of some solvents (measured on M20 porous carbon electrode with 1 mol/l  $\text{Et}_4\text{NPF}_6$  as salt) [82]

The irreversible reductive decomposition of liquid organic electrolytes, including solvents and salt, starts around 1 V vs. Li/Li<sup>+</sup> (depends on the compounds; typically ~0.7 V vs. Li/Li<sup>+</sup> for most electrolytes). This decomposition results in the formation of an ionically conductive and electrically insulating passivation layer on the negative electrode surface. This passivation layer is also called solid electrolyte interphases (SEI). Due to the fact, that the cycle stability, life time, power, rate capability as well as safety of LIBs are influenced by the SEI properties, it is not surprising that a lot of research work on the SEI formation and its composition was done. In contrast to the passivating layer on the negative electrode, less information on the interface layer of the positive electrode can be found in literature. The reason therefore is mainly the difficult experimental implementation caused by the formation of a very thin passivating layer. [87]

In case of carbonaceous materials, the formed SEI layer has the task to avoid the intercalation of solvated lithium-ions, additionally to the prevention of further electrolyte decomposition. The solvation shell of the Li<sup>+</sup>-ions is stripped off during its diffusion through the SEI layer. This is very important because an intercalation of solvated lithium-ions causes an expansion of the graphitic matrix, leading to exfoliation of the graphite layers and reduced capability of the graphite material. [33] A schematical representation of the lithium-ion intercalation process into graphite is displayed in figure 22. This figure nicely sums up the processes described above.



**Figure 22: Schematical illustration of an graphene interlayer without Li<sup>+</sup> intercalate, with a solvated Li<sup>+</sup> intercalate (solvated (ternary) graphite intercalation compound GIC) and desolvated Li<sup>+</sup> intercalates (graphite intercalation compound GIC) [88] (interlayer distance data of ternary GIC formed in PC-electrolyte [89])**

As previously mentioned, the SEI consists of electrolyte decomposition products. More precisely, the reductive decomposition of the salt anions produces inorganic (LiF, Li<sub>2</sub>O) compounds. Furthermore, partial or complete decomposition of the solvents produces Li<sub>2</sub>CO<sub>3</sub>, semicarbonates, alkoxides and polymeric compounds. Additionally, the chemical composition, the thickness and the formation-voltage of the SEI depend on the electrolyte composition, temperature, charge-current density and the type of electrode. [90] [91] [92]

### 3.5 Ageing mechanisms in lithium-ion batteries

The requirements on calendar life-time and cycle life of LIBs are constantly increasing. Therefore, much research was performed to understand the complex ageing processes during storage as well as during operation of this battery system. However, ageing processes like capacity decrease and power fading are complex processes, which involve several processes and their interactions. Due to the fact, that the ageing mechanisms are strongly influenced by the nature of the active materials, electrode design, electrolyte composition, impurities etc., it is difficult to generalize the results for the great variety of cell systems and setups. [93]

Usually, the calendar life of LIBs is primarily influenced by ageing effects, which take place during storage (e.g. self-discharge, impedance rise). The cycle life of a battery is additionally affected by the ageing effects occurring during operation (e.g. mechanical degradation, lithium plating). [93] [94]

It is assumed that the ageing processes of a battery mainly lead to changes of the electrode/electrolyte interface, the electrolyte, the active materials as well as the composite electrode (binder, current collector, conductive additives, etc.). [93]

A schematical illustration of the ageing mechanism in carbonaceous electrodes is given in figure 23.

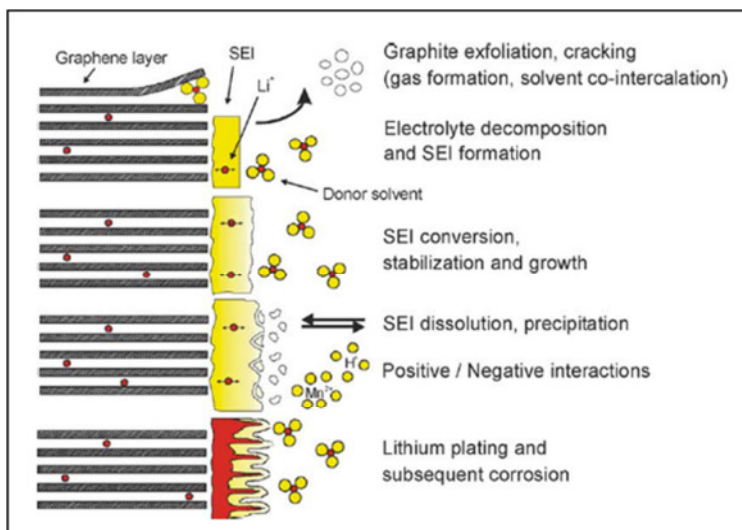


Figure 23: Schematical illustration of changes at carbonaceous electrode/electrolyte interface [93]

Furthermore, a summary of the ageing causes, effects, and influences as well as possible preventions with regard to negative electrodes in LIBs can be found in table 5.

Table 5: Causes, effects and influences of LIB anode ageing (redrawn) [93]

Cause	Effect	Leads to	Reduced by	Enhanced by
Electrolyte decomposition (→SEI) (Continuous side reaction at low rate)	Loss of lithium Impedance rise	Capacity fade Power fade	Stable SEI (additives) Rate decreases with time	High temperatures High SOC (low potential)
Solvent co-intercalation, gas evolution and subsequent cracking formation in particles	Loss of active material (graphite exfoliation) Loss of lithium	Capacity fade	Stable SEI (additives) Carbon pre-treatment	Overcharge
Decrease of accessible surface area due to continuous SEI growth	Impedance rise	Power fade	Stable SEI (additives)	High temperatures High SOC (low potential)
Changes in porosity due to volume changes, SEI formation and growth	Impedance rise Over-potentials	Power fade	External pressure Stable SEI (additives)	High cycling rate High SOC (low potential)
Contact loss of active material particles due to volume changes during cycling	Loss of active material	Capacity fade	External pressure	High cycling rate High DOD
Decomposition of binder	Loss of lithium Loss of mechanical stability	Capacity fade	Proper binder choice	High SOC (low potential) High temperatures
Current collector corrosion	Over-potentials Impedance rise Inhomogeneous distribution of current and potential	Power fade Enhances other Ageing mechanisms	Current collector pre-treatment	Overdischarge Low SOC (high potential)
Metallic lithium plating and subsequent electrolyte decomposition by metallic lithium	Loss of lithium (Loss of electrolyte)	Capacity fade (Power fade)	Narrow potential window	Low temperature High cycling rates Poor cell balance Geometric misfits

In addition it has to be considered, that ageing processes also occur at the positive electrode side and are often initiated or enhanced by ageing mechanisms on the negative electrode. An overview on possible ageing mechanisms at the positive electrode are described and schematically represented in figure 24 and figure 25.

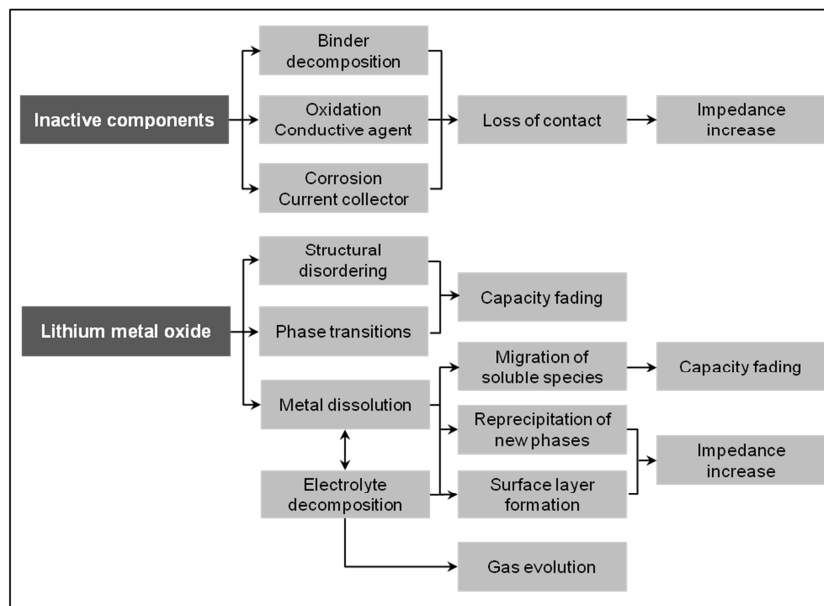


Figure 24: Causes and effects of the ageing mechanisms in case of cathode materials (redrawn from [95])

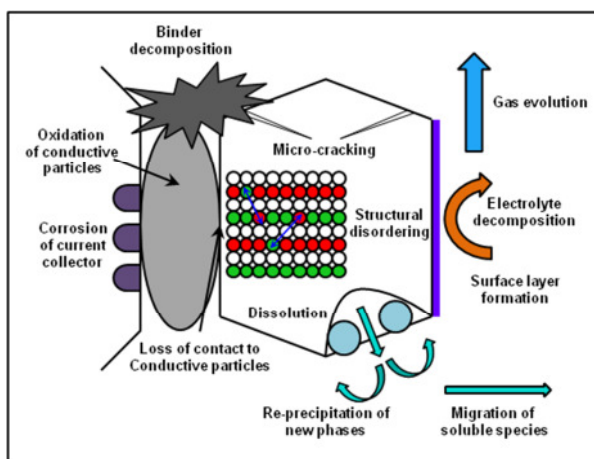


Figure 25: Schematical illustration of cathode ageing mechanisms (redrawn from [93])

**Summary of battery ageing:**

The ageing of LIBs is caused by multiple and complex processes and is responsible for cell impedance rise, power fading and capacity loss in the overall battery system. Furthermore, the ageing of a battery and therefore its performance and life time are influenced by active materials properties, surface chemistry of the electrodes as well as storage and cycling conditions. Regarding the storage and cycling condition, negative effects on the battery performance and life time were reported for both, low and high state of charges (SOC) as well as for low and elevated temperatures. Additionally, the ageing of a battery can also be affected by its designs, mainly due to inhomogeneities in the electrodes. [93] [96]

## 4 Experimental Part

### 4.1 Electrode fabrication and measurement setup

All electrode preparations were carried out by slurry-technique. Therefore a viscous solution, the so called electrode slurry, consisting of binder, conductivity additive, active material and a slurry solvent, was coated on a copper current collector by an automated doctor blade. After drying, electrodes with a diameter of 12 mm were punched out from the electrode foil. Thereafter a further drying step under vacuum, the electrodes were weighed, dried again and electrochemically characterized.

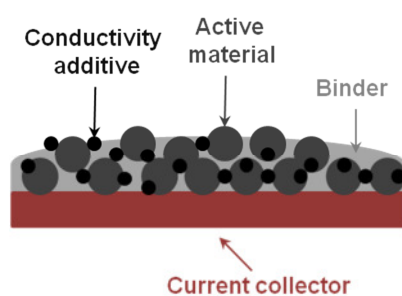


Figure 26: Copper current collector foil coated with electrode-slurry

For the electrode slurry preparation the following components and compositions were used.

Table 6: Electrode slurry composition used in this thesis

Components		Composition [wt%]
<i>Binder:</i>	Sodium-carboxymethyl cellulose	7
<i>Conducting additive:</i>	Carbon nanotubes / carbon black mixture	5
Active material		88
Deionised water as solvent (+ 1 drop surfactant)		

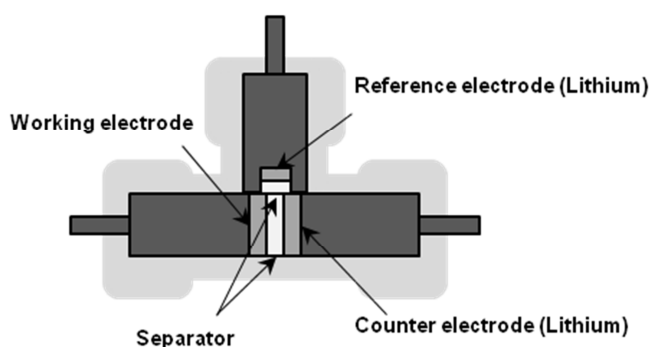


Figure 27: Schematical illustration of a measurement cell type Swagelok®

### ***Measurement cell setup type Swagelok®:***

Electrochemical measurements within this work were performed in Swagelok® half-cell. Accordingly, lithium metal is used as counter-electrode providing the lithium-ions demand, in order to investigate lithium-free anode materials. The reference electrode in the 3 electrodes arrangement of the used T-cell type Swagelok® also consists of lithium metal and is positioned vertically between working- and counter-electrode. The separator, which prevents of internal short circuits by contact of the working- and counter-electrode and additionally acts as carrier of the electrolyte reservoir, is settled between counter- and working-electrode. A further separator separates the reference-electrode and working/counter-electrode.

## **4.2 Electrochemical characterisation**

All electrochemical characterisations in this thesis were carried out by cyclic voltammetry (CV) and constant current charging (CCC) measurement methods. Moreover, a description of the used programs for CV and CCC measurements can be found in table 7 and table 8.

### **Program used for CV measurements:**

Table 7: Program used for CV measurements

<b>CV program (CV1)</b>	
Start point	OCV
Voltage limits of the cycles [V]	0-1.5
Scan rate [ $\mu\text{V}\cdot\text{s}^{-1}$ ]	30

**Program used for CCC measurements:**

Table 8: Program used for CCC measurements

Rest step for 6h		
Process conditions		(x)
<b>Formation</b>		
Step 1	Lithiation*	C-rate of 0.1
	Additional lithiation**	4h
	Delithiation***	C-rate of 0.1
Step 2	Lithiation	C-rate of 0.2
	Additional lithiation	3h
	Delithiation	C-rate of 0.2
Step 3	Lithiation	C-rate of 0.3
	Additional lithiation	2h
	Delithiation	C-rate of 0.3
<b>Cyclization</b>		
Lithiation		C-rate of 0.5
Additional lithiation		1h
Delithiation		C-rate of 0.5

\* Lithiation...with (x) C-rate until the cut-off voltage of 5mV is reached

\*\* Additional lithiation...holding at the voltage of 5mV for (x) hours

\*\*\* Delithiation... with (x) C-rate until the cut-off voltage of 1500mV is reached

### 4.3 Particle characterisation

The particle characterisation with transmission electron microscopy (TEM), energy filtered - TEM (EF-TEM) and focused ion beam (FIB) technique were carried out by the Austrian Center for Electron Microscopy and Nanoanalysis (FELMI-ZFE).

Furthermore, the BET surface measurements were carried out by the Research Center Pharmaceutical Engineering.

At least the SEM pictures and all particle size distributions measurements were carried out with devices from the company Varta Micro Innovation GmbH.

A list of devices is represented in the appendix.

## 4.4 Active material fabrication: Fluidized bed reactor

In this type of reactor, a fluidization of a granular solid material by a fluid (gas or liquid) takes place. Especially in pharmaceutical, chemical, cosmetic and food industries, fluidized bed reactors are often used for changes or improvement of material properties (colour, taste, flowability etc.) by surface coating. [97] [98]

The so called wurster-configuration represents a more advanced method for particle coating using a fluidized bed reactor. This method is a very efficient equipment to obtain high quality particle coatings. [99] [100] A schematical illustration of such wurster-configuration is given in figure 28.

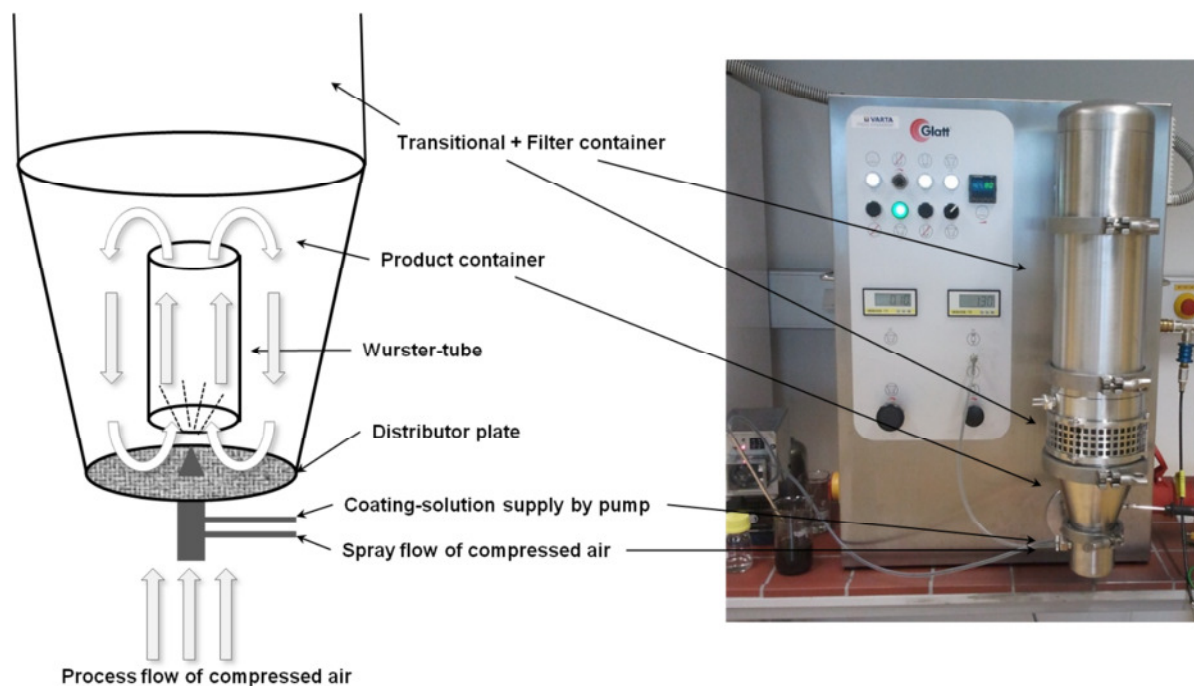


Figure 28: Fluidized bed reactor (Mini Glatt) wurster-configuration

The main difference of fluidized bed reactors with wurster-configuration compared to the classical fluidized bed reactors is displayed by the presence of a wurster-tube. The wurster-tube is directly located above the spray nozzle, which is placed in the middle of the distributor plate at the bottom of the material container. The spray nozzle delivers the coating suspension in form of fine drops, which are subsequently wetting the particle surfaces. The reactor can be differentiated in the following three main zones: [98]

- The coating zone is located in the inner wurster-tube, where the particles are accelerated, like in a pneumatic transport. During the transport through the tube the particles are first wetted with the coating solution and in addition continuously dried on the way to the end of the tube.
- Arriving at the end of the tube, the particles are slowed down, due to the decreased air velocity at the offered, enlarged space. In this zone, where the particles fall back to the bottom, the drying process of the particles has to be sufficiently completed in order to avoid an agglomeration of the particles.
- In the zone of the bottom of the reactor above the distributor plate the particles form a very dense bed and return again in the coating zone for further cycles.

With this circulating coating principle, it is possible to create a very uniform particle coating layer. [101] [102] An overview of the principle of the whole particle coating process is given in figure 29.

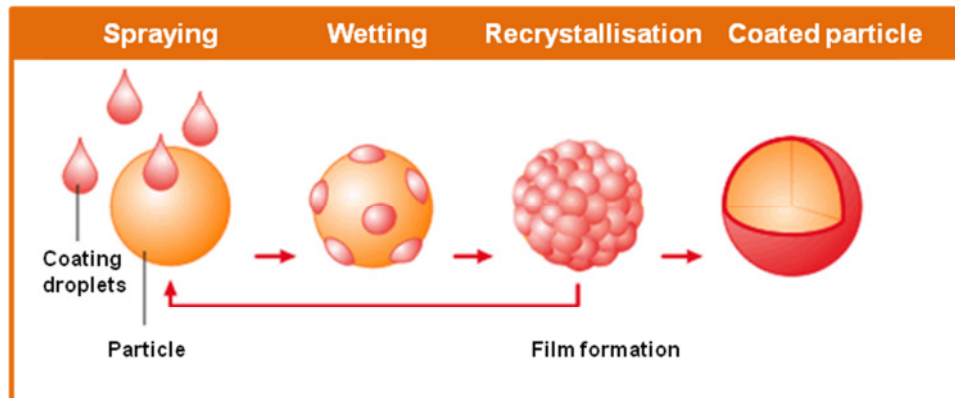
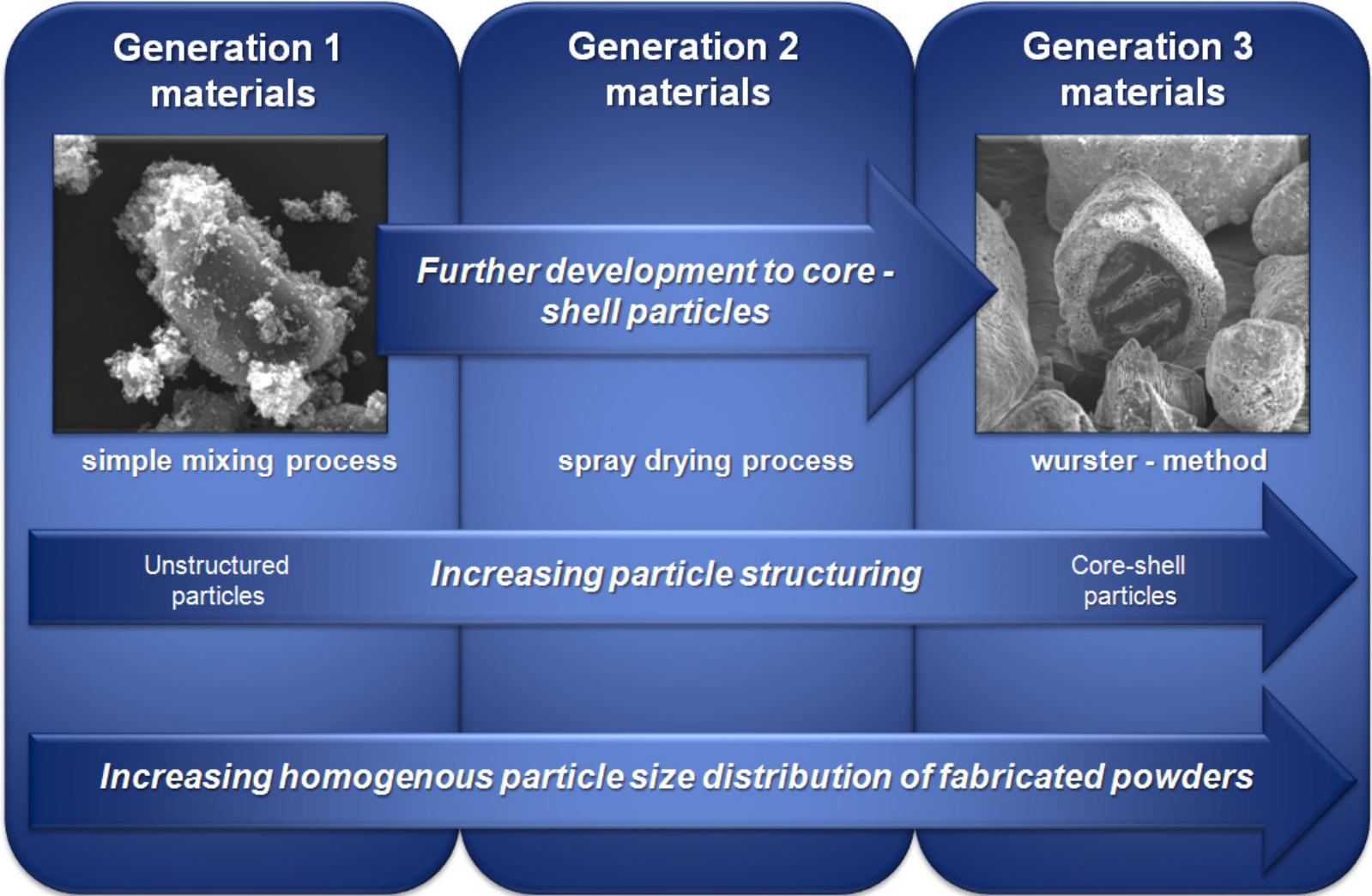


Figure 29: Particle coating principle [102]

Overview of the experimental part



## 4.5 Introduction

The commercial application of silicon as anode material for lithium-ion batteries is currently limited due to low cycle stability caused by an enormous volume- and structure change during the lithiation/delithiation process. A strategy to compensate these volume- and structure changes was developed in the context of this doctoral thesis.

One method to improve the cycle stability is to create a nano-sized silicon-graphite composite active material with a core-shell structure, where the silicon particles are located in the shell and embedded in a carbonaceous matrix. This matrix should compensate the volume changes during the lithiation/delithiation process, reduce the surface area of the overall particles and enhance the conductivity of the particles. The carbonaceous matrix for structural stabilisation is produced by adding an initially inactive polymer precursor to the active materials during the active material fabrication and pyrolysing this initial precursor to form the carbonaceous matrix at the second process step. After all fabrication steps the polymer precursor is mainly/completely converted into a carbonaceous matrix, which improves the cycle stability of the active material by compensating the huge structural changes of the silicon particles. Furthermore, the embedding of the silicon particles reduces the contact area to the electrolyte, and therefore decreases the irreversible capacity, caused by SEI formation within the first cycles. [103]

As mentioned before, the aim of the present doctoral thesis is to develop a core-shell material, which is illustrated in figure 30. The core is made up of a graphite particle and the shell contains silicon particles, which are embedded in a carbonaceous matrix. This carbonaceous matrix is built up of pyrolysed polymer precursor, which may additionally enclose carbon black particles.

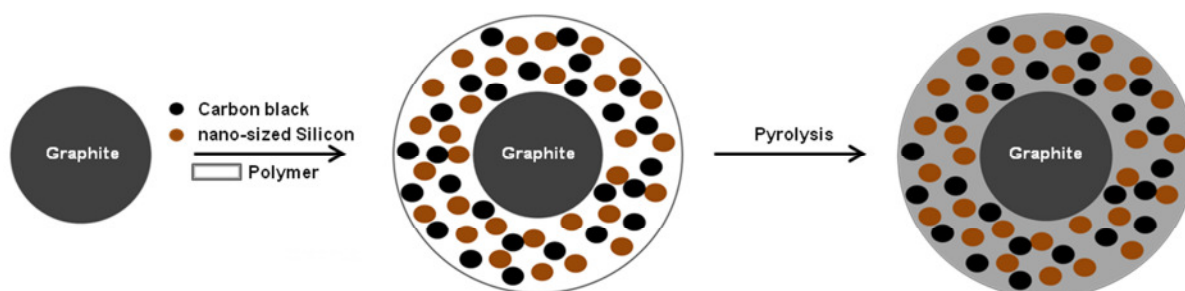


Figure 30: Schematic diagram of particle design

At first, a polymer had to be found, which was soluble and unreactive against the active material as well as able to achieve a high pyrolysis yield. A variety of different polymer precursors were tested and the molecule with the most promising results was used for further research on the structural design of the desired core-shell compound.

## 4.6 Research on polymer precursors

As previously described, the main target was to develop a new structural design for silicon-graphite composite materials with core-shell composition, where ideally a graphite particle acted as core and silicon particles, embedded in an amorphous carbonaceous matrix, acted as shell. To realise this structure an adhesive had to be added, which should guarantee an initially good adhesion between the core and shell particles, as well as a good electrical conductivity and structural stability by the formation of a carbonaceous matrix after a pyrolysis step. Furthermore, the adhesive had to fulfil the following requirements:

- solubility in solvents
- non-reactiveness against the active material during the pyrolysis
- provision of a pure carbonaceous matrix after the pyrolysis [104]

In this context, polymers were attractive candidates to act as an adhesive in first place and allowing pyrolysis afterwards.

Due to the satisfying solubility as well as good pyrolysis behaviour, polyvinylidene difluoride (PVdF), tar and epoxy resin were tested as polymer precursors.

Therefore, silicon-graphite composite electrodes were fabricated with these polymers according to the procedure shown in table 9. The fabricated electrodes were electrochemically characterized by cyclic voltammetry (CV).

Table 9: Active material and electrode fabrication procedure of SiC\_Tar, SiC\_PVdF and SiC\_EP

Name	Used polymer
SiC_Tar	Tar
SiC_PVdF	Polyvinylidene difluoride
SiC_EP	Epoxy resin

Active material (AM)	
Composition (before pyrolysis) + procedure	20 wt% Polymer precursor
	80 wt% CNP* <ul style="list-style-type: none"> <li>20 wt% nano-sized Silicon</li> <li>10 wt% Carbon black</li> <li>70 wt% Graphite</li> </ul> <ul style="list-style-type: none"> <li>➤ Mixing of components at room temperature with stirring magnet</li> <li>➤ Removing the solvent</li> <li>➤ Pyrolysing the product at 900 °C for 2h under Argon atmosphere in a tube furnace</li> </ul>

Electrode preparation	
Slurry composition + procedure	Binder: 7 wt% Sodium-carboxymethylcellulose (Na-CMC) Conductive additive: 5 wt% Carbon nanotubes (CNT)/carbon black Active material: 88 wt% Active material Solvent: H <sub>2</sub> O + 1 drop of surfactant
	<ul style="list-style-type: none"> <li>➤ First the binder was dissolved completely in the solvent</li> <li>➤ All other components were added in the binder solution and stirred over night</li> </ul>
Electrode preparation	<ul style="list-style-type: none"> <li>➤ The prepared slurry was coated on a copper current collector by the use of an automated doctor blade and dried at 60 °C in a compartment dryer</li> <li>➤ Electrodes with a diameter of 12 mm were punched out and dried in vacuum at 120 °C for 12 h, weighted and again dried for 4 h</li> <li>➤ Electrochemical measurements (CV) were performed in Swagelok® T-cells</li> </ul>

\*CNP... Components that are not pyrolysed

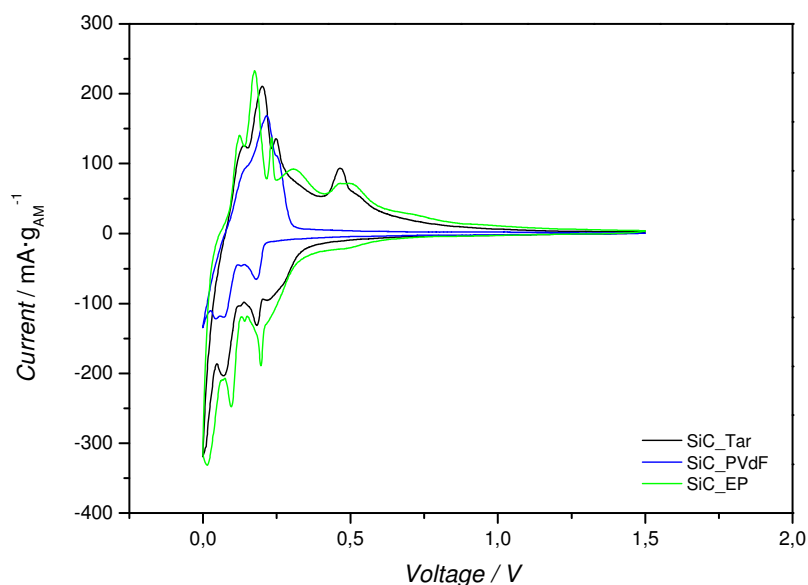


Figure 31: Comparison of 3rd cycle of CV experiments of electrodes with different polymer precursors (CV1)

Table 10: Corresponding delithiation/lithiation capacities and efficiencies of CV measurements (Figure 31)

SiC_Tar				
Electrolyte:	Cycle	Delithiation [mAh·g <sub>AM</sub> <sup>-1</sup> ]	Lithiation [mAh·g <sub>AM</sub> <sup>-1</sup> ]	Efficiency [%]
EC:EMC 3:7 1M LiPF <sub>6</sub> + 2% VC	1	328	572	57
CNP <sub>after pyrolysis</sub> [wt%]:	2	424	458	93
87	3	490	518	95
SiC_PVdF				
Electrolyte:	Cycle	Delithiation [mAh·g <sub>AM</sub> <sup>-1</sup> ]	Lithiation [mAh·g <sub>AM</sub> <sup>-1</sup> ]	Efficiency [%]
EC:EMC 3:7 1M LiPF <sub>6</sub> + 2% VC	1	204	378	54
CNP <sub>after pyrolysis</sub> [wt%]:	2	214	231	92
80	3	218	230	95
SiC_EP				
Electrolyte:	Cycle	Delithiation [mAh·g <sub>AM</sub> <sup>-1</sup> ]	Lithiation [mAh·g <sub>AM</sub> <sup>-1</sup> ]	Efficiency [%]
EC:EMC 3:7 1M LiPF <sub>6</sub> + 2% VC	1	617	906	68
CNP <sub>after pyrolysis</sub> [wt%]:	2	793	889	89
93	3	848	923	92

Table 11: Calculated capacities of SiC\_Tar, SiC\_PVdF and SiC\_EP materials

Name	Capacity [mAh·g <sub>AM</sub> <sup>-1</sup> ]
SiC_Tar	957
SiC_PVdF	880
SiC_EP	1023

As shown in table 11, both the SiC\_Tar and the SiC\_PVdF electrodes did not achieve the calculated capacities (Table 11). Only the performance of the SiC\_EP electrode was satisfactory in terms of capacity.

Due to the considerably better electrochemical results of the SiC\_EP electrode, epoxy resin was chosen as polymer precursor for further work.

The next project step was to figure out the optimum mixture of polymer precursor and active material as well as an optimum pyrolysis temperature.

## 4.7 Generation 1 of silicon-graphite composite materials

Within this project the generation 1 (Gen1) represented a preliminary stage of the composite material. In this project phase, a more detailed understanding of the optimum ratio of initial epoxy resin (EP) to silicon/graphite/carbon black (CNP) and the ideal pyrolysis temperature was gained. Fabrication of Gen1 materials was done by mixing silicon, graphite and carbon black as well as the precursor polymer, followed by a subsequent pyrolysis of the product.

### 4.7.1 Fabrication procedure

The composition and fabrication procedure of Gen1 materials are represented in table 12 and table 13.

Table 12: Composition of Gen1 materials

EP/CNP ratio	EP and CNP composition	
x wt% EP*	80 wt%	Araldite <sup>®</sup> 506
	20 wt%	3-Dimethylamino-propylamin (DAPA)
x wt% CNP	20 wt%	nano-sized Silicon
	10 wt%	Carbon black
	70 wt%	Graphite
<b>1-Methoxy-2-propanol as solvent</b>		

\*EP... Epoxy resin precursor

**Table 13: Procedure of Gen1 material fabrication**

Step 1	The Araldite <sup>®</sup> 506 (uncured epoxy resin) was dissolved in 1-methoxy-2-propanol at room temperature
Step 2	The desired quantities of silicon, carbon black and graphite were added into the Araldite <sup>®</sup> 506 solution, after the solution was stirred at room temperature for 12 h
Step 3	The epoxy resin hardener 3-Dimethylamino-propylamin (DAPA) was added to the product solution and stirred for 2 h at room temperature
Step 4	The product slurry was dried and the containing Araldite <sup>®</sup> 506 was cured in a compartment dryer at 60 °C for several days (depending on initial epoxy resin content). After this curing step it was crushed to small particles by the use of an agate mortar
Step 5	The resulting product was transferred in a tube furnace, where the product was pyrolysed and afterwards crushed again with an agate mortar to obtain a fine-grained powder for the electrode slurry preparation
Step 6	Electrode preparation according to table 9

#### 4.7.2 Optimization of EP/CNP composition

To identify the optimum composition ratio of EP and CNP, Gen1 powders with different EP to CNP compositions were produced (Table 15). CNP represented a mixture of the electrochemically active materials like silicon and graphite and the conductive additive carbon black. After mixing with a specified amount of EP the product mixture was pyrolysed. In this step, the epoxy resin precursor was decomposed and converted into carbonaceous matrix accompanied with a weight loss of the obtained pyrolysed product. Due to this procedure the amount of CNP increased in the final product (Table 15).

In case of Gen1, where the crushing of pyrolysed product was figured out with an agate mortar, the powders with initial epoxy resin precursor content above 40 wt% were greatly coarse-grained and due to this an electrode preparation wasn't possible. By this reason, only powders with initial epoxy resin content until 40 wt% were electrochemically characterized.

**Table 14: Pyrolysis parameters of Gen1 materials introduced in table 15**

Step 5: Tube furnace parameters	
Heating rate [°C min <sup>-1</sup> ]	10
Process temperature [°C]	900
Process time [h]	2
Process atmosphere	Argon

Table 15 sums up the EP/CNP ratios before and CM/CNP ratios after pyrolysis of different Gen1 materials.

**Table 15: Composition ratios before and after pyrolysis of Gen1 materials with different EP content**

Name	Before pyrolysis		After pyrolysis	
	EP wt%	CNP wt%	CM* wt%	CNP wt%
Gen1_0	0	100	0	100
Gen1_1	10	90	3	97
Gen1_2	20	80	4	96
Gen1_3	30	70	10	90
Gen1_4	40	60	11	89
Gen1_5	50	50	11	89
Gen1_6	60	40	13	87

\*CM...Carbonaceous matrix formed by pyrolysed epoxy resin precursor (EP)

Considering the CM/CNP ratios after pyrolysis of the fabricated Gen1 powders (Table 15), a tendency of decreasing pyrolysis product yield at increasing EP content can be observed (Gen1\_1 with a 10 wt% EP content obtained 3 wt% CM and Gen1\_6 with a significant higher EP content of 60 wt% only obtained 13 wt% CM). This tendency of decreasing pyrolysis product yield by increasing the initial epoxy resin content is also present at generation 2 (Gen2) and generation 3 (Gen3) materials.

In addition, the manufactured powders containing different CM/CNP composition ratios were fabricated to electrodes and electrochemically characterized by CCC measurement.

**Table 16: Electrode weights of the following CCC measurements and calculated capacities of Gen1 materials fabricated with different EP contents**

Used Gen1 material	Electrode weight [ $\text{mg}\cdot\text{cm}^{-2}$ ]	Capacity* [ $\text{mAh}\cdot\text{g}_{\text{AM}}^{-1}$ ]
Gen1_1	0.858	1067
Gen1_2	0.837	1056
Gen1_3	0.760	990
Gen1_4	0.955	979
Gen1_0	0.822	1100

\*The capacity of each manufactured powder was determined by the contained silicon and graphite content

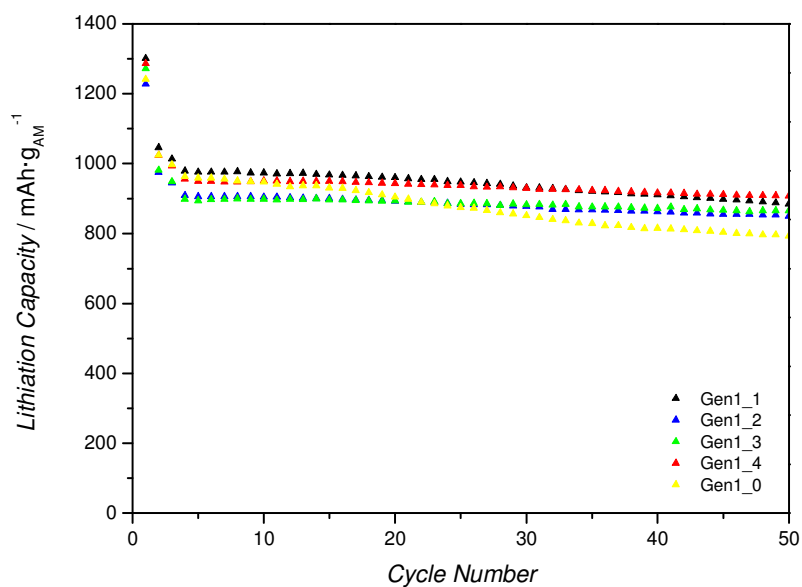


Figure 32: Lithiation capacities received in CCC measurements of electrodes containing different Gen1 materials (CCC1)

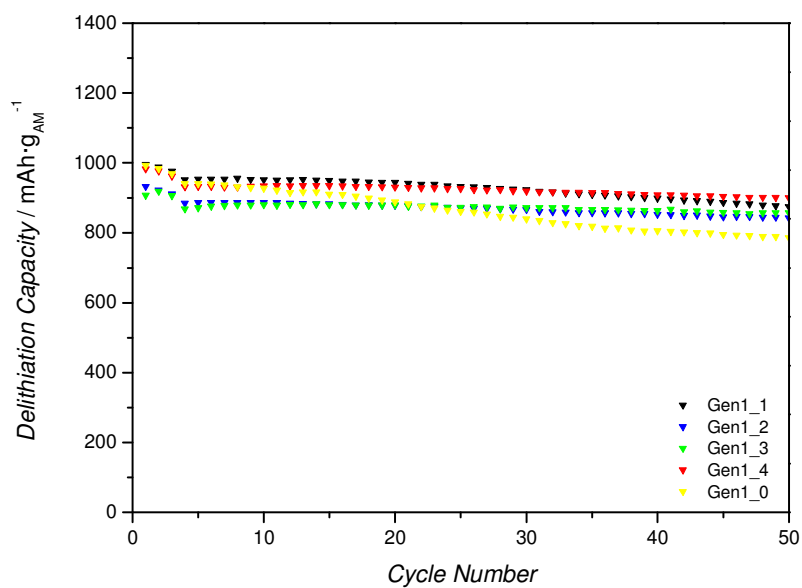
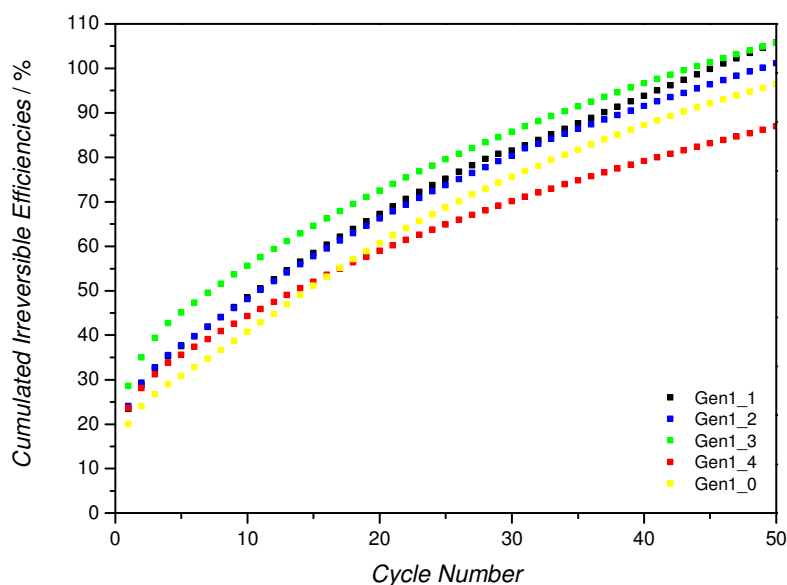


Figure 33: Delithiation capacities received in CCC measurements of electrodes containing different Gen1 materials (CCC1)



**Figure 34: Cumulated irreversible efficiencies received in CCC measurements of electrodes containing different Gen1 materials (CCC1)**

The lithiation and delithiation capacities of Gen1\_0 electrode, which was fabricated without initial epoxy resin precursor, shows high capacity fading comparable to the capacity fading of standard nano-sized silicon-graphite composite anodes, mainly caused by contact loss of the expanded silicon particles. In case of Gen1 electrodes, which were fabricated with an initial epoxy resin precursor, this high capacity fading is not present due to compensation of the huge volume changes of the silicon particles by the carbonaceous matrix.

Gen1\_4 electrode achieves the highest and Gen1\_2 electrode the lowest reversible capacities compared to their theoretical capacities (Table 16). Comparing the electrode performance of Gen1\_1 electrode with the lowest and Gen1\_4 electrode with the highest content of carbonaceous matrix it becomes obvious that Gen1\_1 electrode suffers from a higher capacity fading than Gen1\_4 electrode. The higher capacity fading of Gen1\_1 electrode compared to Gen1\_4 electrode can be explained by the lower structural stabilisation due to the weaker (lower content) carbonaceous matrix.

In summary, the best electrode performance after 50 cycles can be achieved by using the composition Gen1\_4 and therefore it was used for further temperature test to optimize the pyrolysis process.

### 4.7.3 Optimization of the pyrolysis process

The powder composition used for the pyrolysis test is shown in table 17.

**Table 17: Powder composition for pyrolysis tests**

EP/CNP ratio	EP and CNP composition	
40 wt% EP	80 wt%	Araldite <sup>®</sup> 506
	20 wt%	DAPA
60 wt% CNP	20 wt%	nano-sized Silicon
	10 wt%	Carbon black
	70 wt%	Graphite
1-Methoxy-2-propanol as solvent		

**Table 18: Composition ratios before and after pyrolysis of Gen1 materials fabricated at different pyrolysis temperatures**

Name	Pyrolysis	Before pyrolysis		Before pyrolysis	
	temperature [°C]	EP wt%	CNP wt%	CM wt%	CNP wt%
Gen1_7	700	40	60	9	91
Gen1_8	800	40	60	10	90
Gen1_9	900	40	60	11	89
Gen1_10	1000	40	60	14	86
Gen1_11	1100	40	60	16	84

According to table 21, it is apparent that the pyrolysis product yield of Gen1 materials increases with higher pyrolysis temperature. The data has to be interpreted carefully because the increasing pyrolysis product yield may also be caused by silicon carbide and not only by desired carbonaceous matrix formation. It is mostly reported in relevant literature that the pyrolysis range without silicon carbide formation is set between 700 °C to 1200 °C [60] [105] [106] [107] [108]. Although there are also reports on silicon carbide formation at pyrolysis temperature under 1200 °C, depending on the used organic precursor (700 °C with PVdF as polymer precursor [109]).

However, a formation of silicon carbide in these composite materials at higher pyrolysis temperature could not be clearly determined within this thesis and has to be clarified in further work.

In order to investigate the influences of the pyrolysis temperature CCC measurements were carried out for Gen1\_7 to Gen1\_11 materials (Figure 35).

**Table 19: Electrode weights of the following CCC measurements and calculated capacities of Gen1 materials fabricated with different pyrolysis temperatures**

Used Gen1 material	Electrode weight [ $\text{mg}\cdot\text{cm}^{-2}$ ]	Capacity [ $\text{mAh}\cdot\text{g}_{\text{AM}}^{-1}$ ]
Gen1_7	0.911	1001
Gen1_8	1.140	990
Gen1_9	0.955	979
Gen1_10	0.707	946
Gen1_11	1.226	924

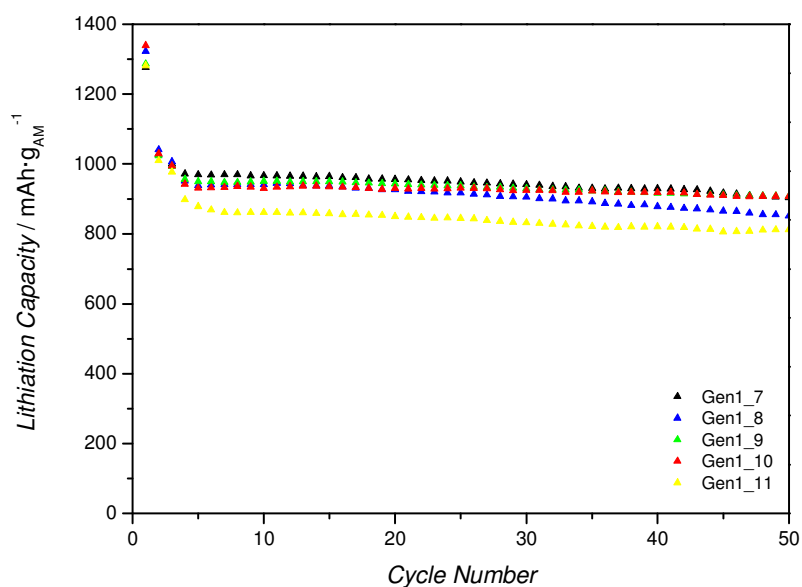


**Figure 35: Lithiation capacities received in CCC measurements of electrodes containing Gen1 materials fabricated with different pyrolysis temperatures (CCC1)**

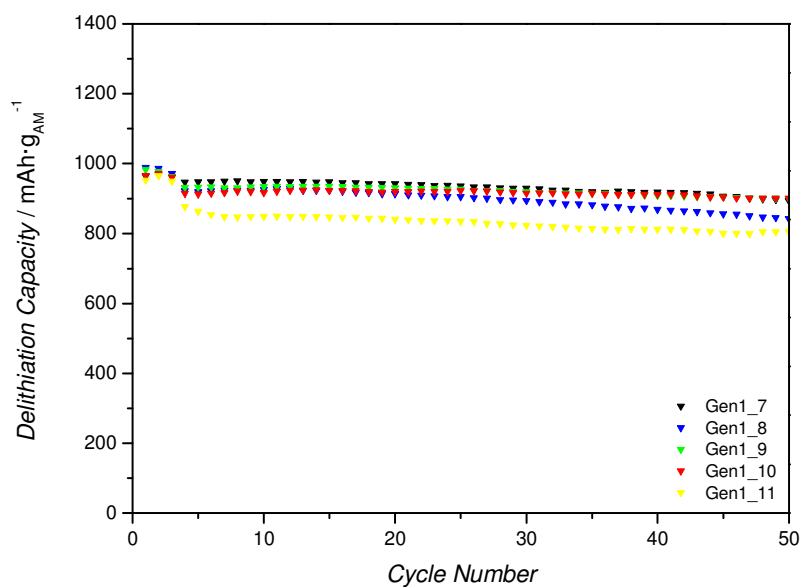


Figure 36: Delithiation capacities received in CCC measurements of electrodes containing Gen1 materials fabricated with different pyrolysis temperatures (CCC1)

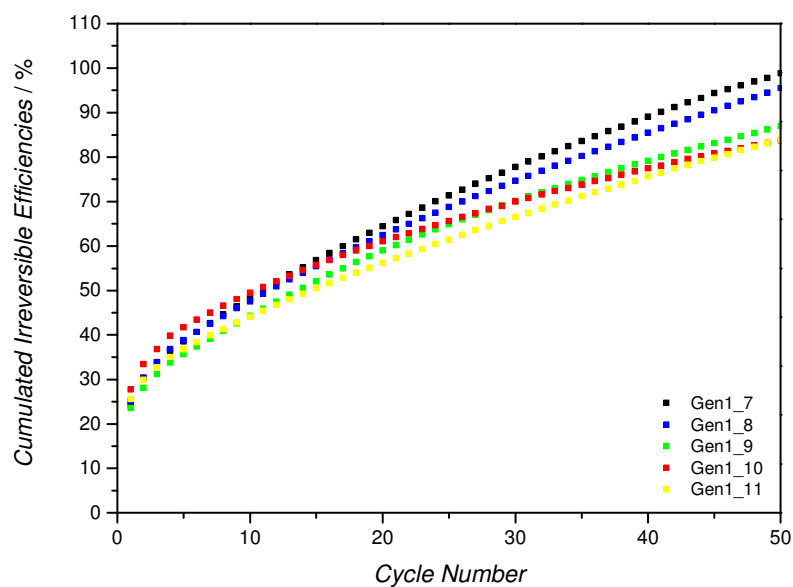


Figure 37: Cumulated irreversible efficiencies received in CCC measurements of electrodes containing Gen1 materials fabricated with different pyrolysis temperatures (CCC1)

Compared to its theoretical capacity lower lithiation/delithiation capacities are achieved by Gen1\_11 electrode after the initial cycles, which can be attributed to the excessively high

pyrolysis temperature. Gen1\_7 and Gen1\_8 electrodes exhibit the highest increases on cumulated irreversible efficiencies (Figure 37), due to non-sufficient pyrolysis and carbonaceous matrix formation, respectively. According to these results the ideal pyrolysis temperature is between 900 °C and 1000 °C.

## 4.8 Generation 2 of silicon-graphite composite materials

The main disadvantages of the Gen1 fabrication technique were the long period of time for the curing step and the increasing agglomeration due to the high epoxy resin content, which led to an undesired coarse-grained powder. These two main problems of Gen1 fabrication method could be solved by further development to Gen2 fabrication method. For these Gen2 powders spray drying technique was used for the powder fabrication and with help of this method the long curing step of Gen1 materials could be eliminated by directly curing in a heated airflow. Furthermore, this method fabricated very fine-grained powders because the particles were passing a two component nozzle, which distributed them in small droplets, before they were cured in the heated airflow. This prevented the formation of large compact agglomerates.

This new fabrication technique was realised by using a fluidized bed reactor (Figure 38).

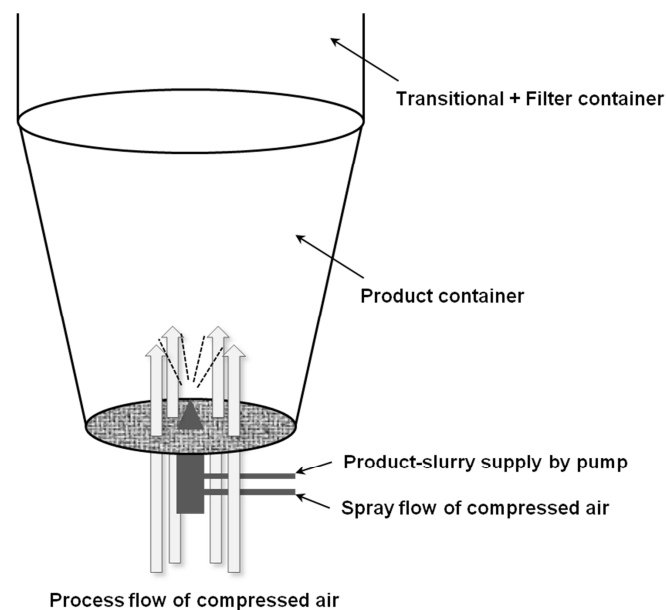


Figure 38: Schematic illustration of spray drying process

### 4.8.1 Fabrication procedure

The steps 1 to 3 of Gen2 fabrication were analogous to Gen1 fabrication steps 1 to 3, while in step 4 the long-term curing was replaced by direct spray drying in case of Gen2 materials. An accurate procedure description is represented in table 20.

**Table 20: Procedure of Gen2 material fabrication**

Step 1 to 3	Step 1 to 3 were equal to step 1 to 3 of Gen1 fabrication (see table 13)
Step 4	The product slurry was directly dried and cured by spraying it into the heated air flow of the fluidized bed reactor through a two component nozzle
Step 5	The cured fine-grained product powder was transferred in a tube furnace where the product was pyrolysed (Tube furnace parameters according to table 14)
Step 6	Electrode preparation according to table 9

The fabricated Gen2 powders were structurally characterized by SEM and in following some selected SEM pictures of Gen2 materials are shown. The fine-grained Gen2 powder, which is shown in figure 39, contains graphite particles with the desired shell of silicon, carbon black and pyrolysed epoxy resin (Figure 40). Nevertheless, a huge quantity of small graphite-free silicon/amorphous carbon agglomerates can also be found.

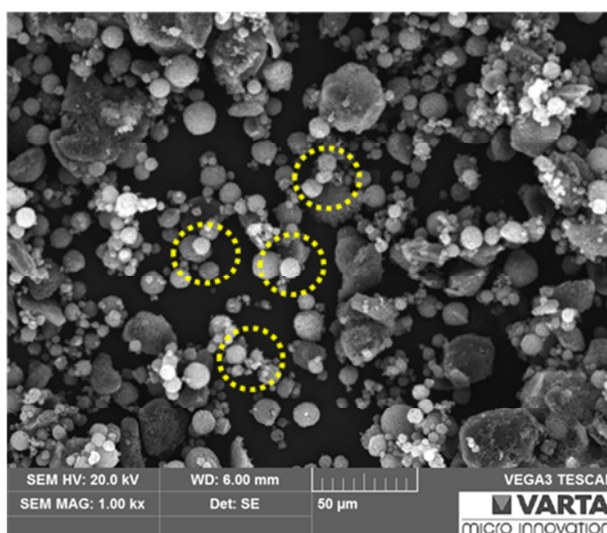


**Figure 39: SEM picture of a Gen2 powder (some of the small graphite-free silicon/amorphous carbon agglomerates are yellow framed)**

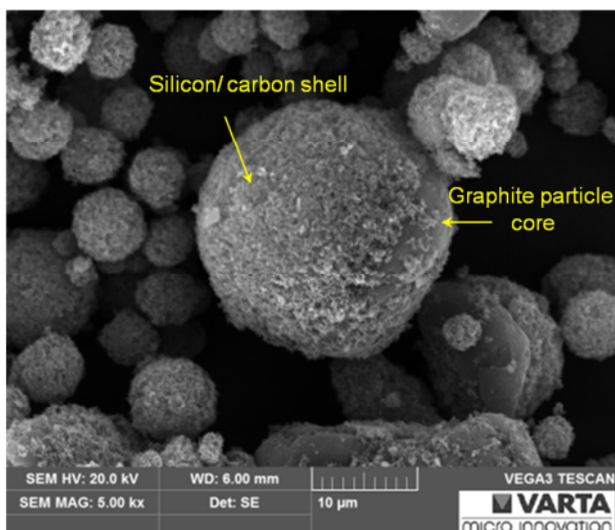


Figure 40: Gen2 graphite particle coated with silicon/amorphous carbon

To clarify the structure of the small graphite-free silicon/amorphous carbon agglomerates (Figure 39) and to prove the graphite absence in the centre of these agglomerates one of them was cut with the help of focused ion beam technique (FIB) (Figure 41).

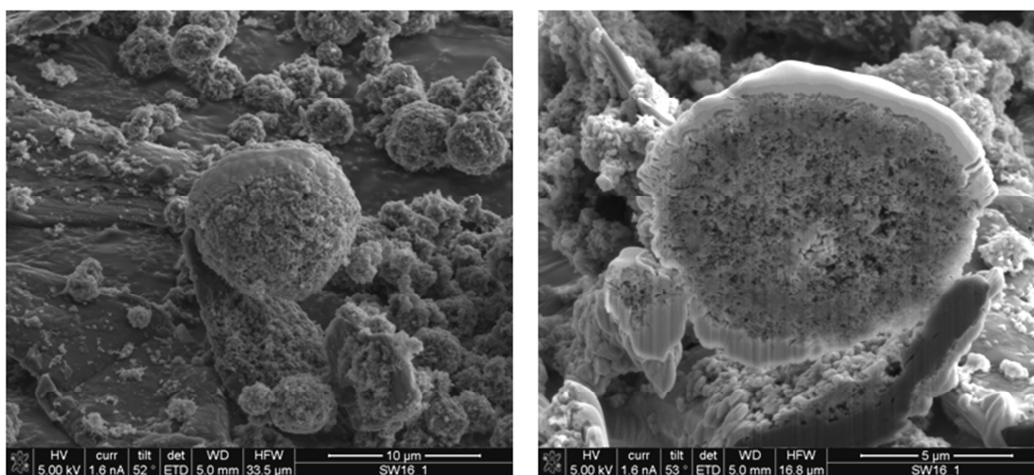
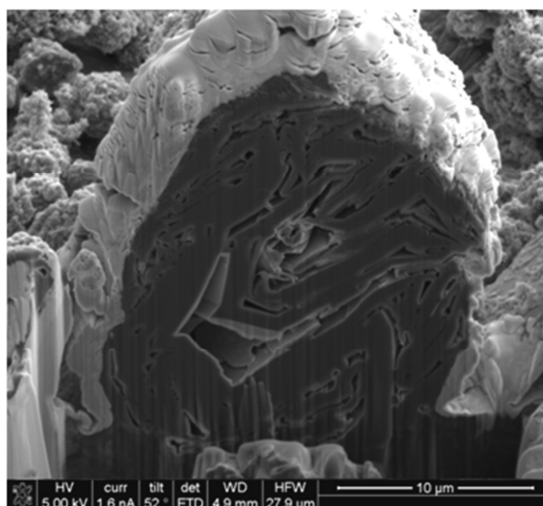


Figure 41: SEM pictures of an unsliced (left) and a FIB sliced (right) silicon/amorphous carbon agglomerate



**Figure 42: FIB sliced graphite particle**

The consistently porous structure of the FIB sliced agglomerate, which is shown in figure 41, shows that these agglomerates aren't containing a graphite particle. The desired particle, however, would contain a graphite particle in the centre, like the FIB sliced particle shown in figure 42.

To prove the prevention of massive compact agglomerate formation, by using the Gen2 method, the particle size distribution (PSD) of a Gen2 material was measured and compared with the PSD of pure graphite and a Gen1 material. This comparison, shown in figure 43, indicates that the Gen1 material has a broad PSD, containing larger and smaller particle sizes. By comparing these results with the PSD of pure graphite, it is obvious that the Gen1 powder contains a noticeable quantity of bigger agglomerates as well as very small silicon/amorphous carbon agglomerates (almost bare silicon/carbon black particles). In case of the Gen2 PSD, only a minor shift to larger particle sizes is observed compared to pure graphite, which can be lead back to the coating of the particles. In contrast to the Gen1 powder no huge agglomerates can be found in the Gen2 material, according to its PSD. This indicates the prevention of large, compact agglomerate formation by the use of Gen2 preparation method. The noticeably higher quantity of small particles within the Gen2 material compared to the pure graphite is caused by the small silicon/amorphous carbon agglomerates, which are still contained in Gen2 powders.

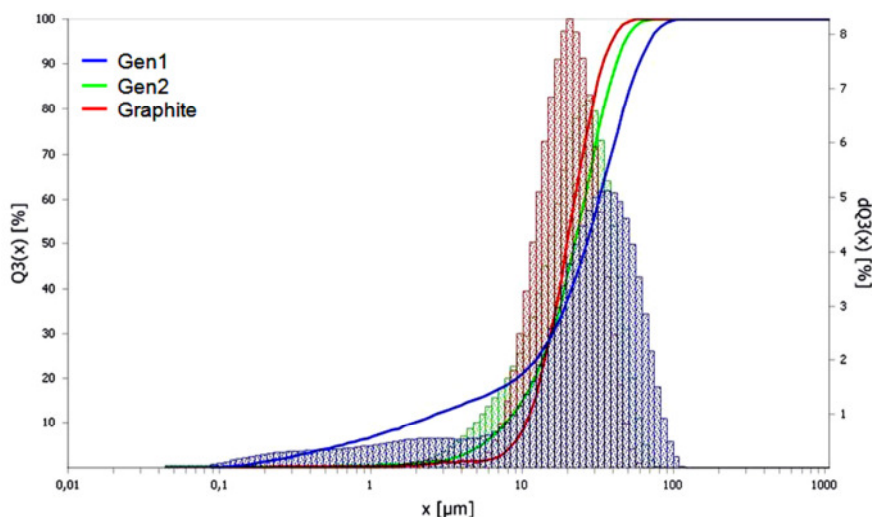


Figure 43: Particle size distribution of a Gen1, Gen2 powder and pure graphite

### 4.8.2 Optimization of the EP/CNP composition

To figure out the optimal EP to CNP ratio for ideal electrode performance, Gen2 powders with different EP to CNP compositions were produced (Table 21 and table 22). Subsequently these fabricated Gen2 powders were prepared to electrodes and electrochemically characterized with CCC measurement.

Table 21: Composition ratios before and after pyrolysis of Gen2 materials with different EP contents

Name	Before pyrolysis		After pyrolysis	
	EP [wt%]	CNP [wt%]	CM [wt%]	CNP [wt%]
Gen2_1	10	90	5	95
Gen2_2	20	80	8	92
Gen2_3	30	70	11	89
Gen2_4	40	60	14	86

Table 22: Additional composition information for table 21

EP/CNP ratio	EP and CNP composition	
x wt% EP	80 wt%	Araldite®506
	20 wt%	DAPA
x wt% CNP	20 wt%	nano-sized Silicon
	10 wt%	Carbon black
	70 wt%	Graphite
1-Methoxy-2-propanol as solvent		

According to table 21, the pyrolysis product yield of Gen2 materials also decreases with increasing initial epoxy resin content, as in case of Gen1 materials. This means that in case of 10 wt% initial epoxy resin to 90 wt% CNP a pyrolysis product yield (CM) of 5 wt% is obtained, while for Gen2\_4 an initial epoxy resin content of 40 wt% only leads to a pyrolysis product yield of approximately 14 wt%.

The used spray drying parameters for the materials Gen2\_1 to Gen2\_4 are displayed in table 23.

Table 23: Spray drying parameters for Gen2 materials with different EP/CNP ratios

Parameter	Gen2_1 – Gen2_4
Process compressed air [bar]	0.07
Spray compressed air [bar]	1
Pump speed [rpm]	03
Temperature [°C]	49-50
Heating time at 80 °C [h]	2
Nozzle diameter [mm]	0.5

Table 24: Electrode weights of the following CCC measurements and calculated capacities of Gen2 materials fabricated with different EP contents

Used Gen2 material	Electrode weight [mg·cm <sup>-2</sup> ]	Capacity [mAh·g <sub>AM</sub> <sup>-1</sup> ]
Gen2_1	0.966	1045
Gen2_2	0.911	1012
Gen2_3	0.875	979
Gen2_4	0.924	946

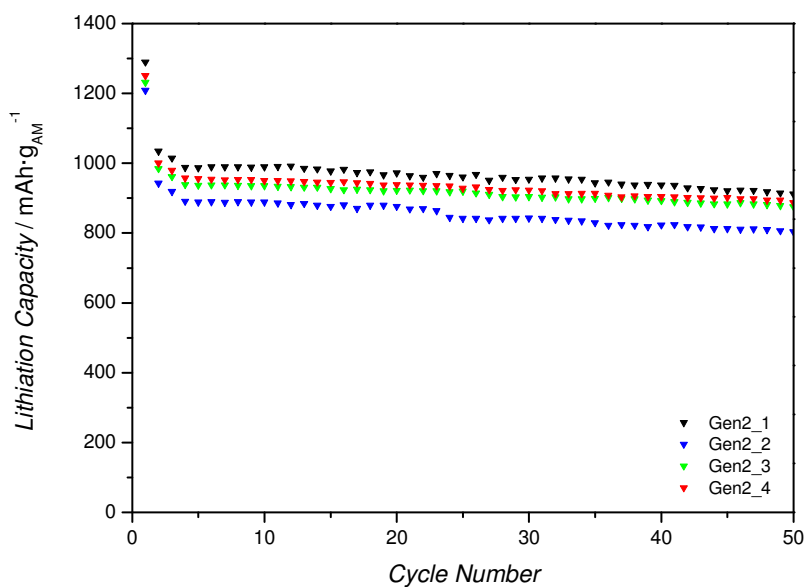


Figure 44: Lithiation capacities received in CCC measurements of electrodes containing Gen2 materials fabricated with different EP content (CCC1)

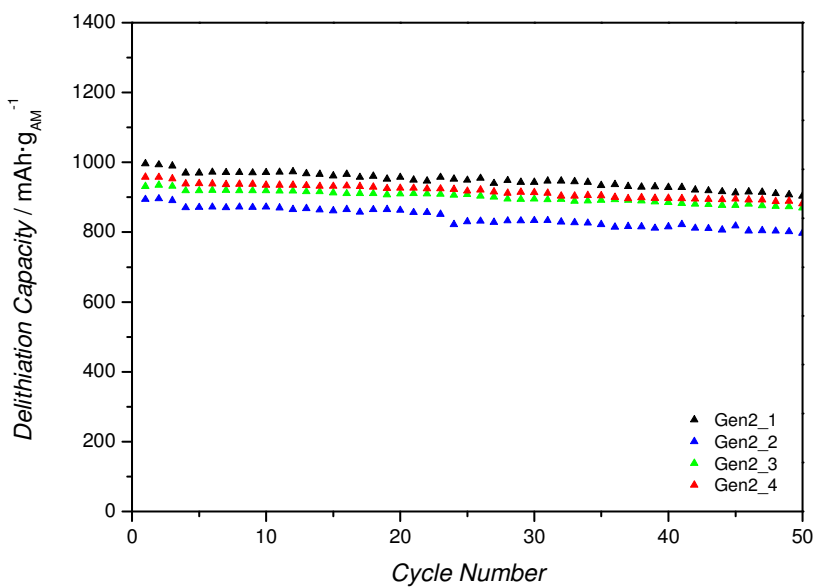
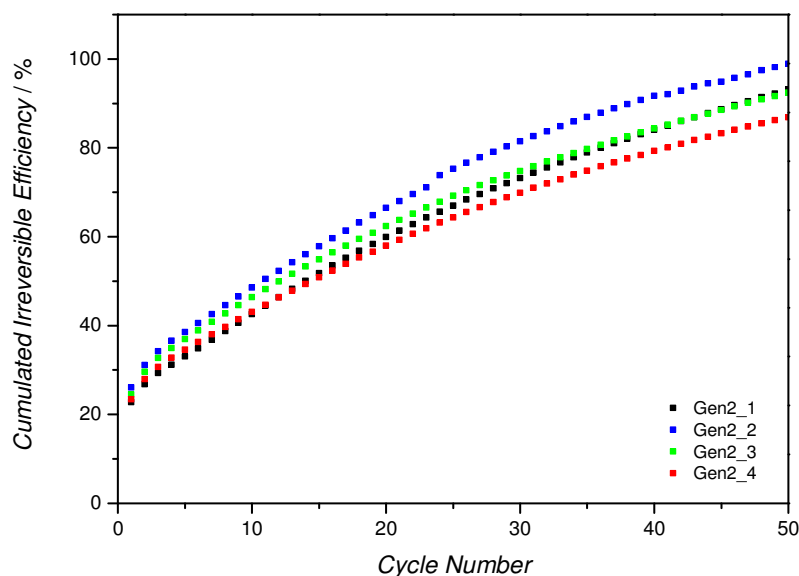


Figure 45: Delithiation capacities received in CCC measurements of electrodes containing Gen2 materials fabricated with different EP content (CCC1)



**Figure 46: Cumulated irreversible efficiency received in CCC measurements of electrodes containing Gen2 materials fabricated with different EP content (CCC1)**

Comparing the CCC results, the Gen2\_2 material exhibits poor performance, which is shown by the lowest achieved capacities compared to its theoretical capacity as well as by the highest increase of the cumulated irreversible efficiency. However, the materials Gen2\_1, Gen2\_3 and Gen2\_4 achieve remarkable good capacities (compared to their theoretical capacities).

The poor efficiency performance of the Gen2\_1 material results in the highest increase of the cumulated irreversible efficiency after 50 cycles, which can be explained by lower structural stabilization. This means that more particles lose the electrical contact to the electrode due to the high volume changes and the associated mechanical stress of the silicon particles during lithiation and delithiation processes. Moreover, this leads to further SEI formation during cycling, because of new surfaces are exposed to the electrolyte, which further decreases the efficiency of the electrode. Therefore, the Gen2\_4 material with highest carbonaceous matrix content shows the lowest increase of the cumulated irreversible efficiency, which indicates a successful structural stabilisation and the most effective prevention of conductivity loss of particles during cycling.

### 4.8.3 Optimization of the spray drying process

To improve the spray drying process of Gen2 materials and to determine the ideal process parameters, Gen2 powders with the same composition but different spray drying parameters were produced and electrochemically characterized. The varied parameters of the spray drying process concerned the spray flow of compressed air for the two component nozzle as well as the pump speed. For technical reason, the process temperature couldn't be varied.

Due to the low weight of the educts, it was necessary to choose the lowest possible process air flow in the lab-sized fluidized bed reactor. This was necessary in order to keep the particles in the product container and to prevent them from plugging the filters.

An illustration of the spray drying process can be found in figure 38.

For the powders fabricated with varied spray drying parameters, an EP/CNP ratio of 40/60 was used (Table 21 and table 22). In order to get a good overview on the process parameter, first, Gen2 materials were fabricated with constant pump speed and varied spray flow of the compressed air. Afterwards, the spray flow was kept constant and the pump speed was varied.

**Table 25: Varied parameters of the spray drying process**

Constant Pump Speed				
Name	Gen2_0.5_03	Gen2_1_03	Gen2_1.5_03	Gen2_2_03
Process compressed air [bar]	0.07			
<b>Spray compressed air [bar]</b>	<b>0.5</b>	<b>1</b>	<b>1.5</b>	<b>2</b>
<b>Pump speed [rpm]</b>	<b>03</b>			
Temperature [°C]	49	46	42	44
Heating time at 80 °C [h]	2			
Nozzle diameter [mm]	0.8			
Constant Spray Flow				
Name	Gen2_1_01	Gen2_1_05	Gen2_1_10	Gen2_1_20
Process compressed air [bar]	0.07			
<b>Spray compressed air [bar]</b>	<b>1</b>			
<b>Pump speed [rpm]</b>	<b>01</b>	<b>05</b>	<b>10</b>	<b>20</b>
Temperature [°C]	49	46	50	46
Heating time at 80 °C [h]	2			
Nozzle diameter [mm]	0.8			

**Table 26: Electrode weights of the following CCC measurements and calculated capacities of Gen2 materials fabricated with varied spray flow and constant pump speed**

Used Gen2 material	Electrode weight [ $\text{mg}\cdot\text{cm}^{-2}$ ]	Capacity [ $\text{mAh}\cdot\text{g}_{\text{AM}}^{-1}$ ]
Gen2_0.5_03	0.879	935
Gen2_1_03	0.932	935
Gen2_1.5_03	0.997	946
Gen2_2_03	0.966	957

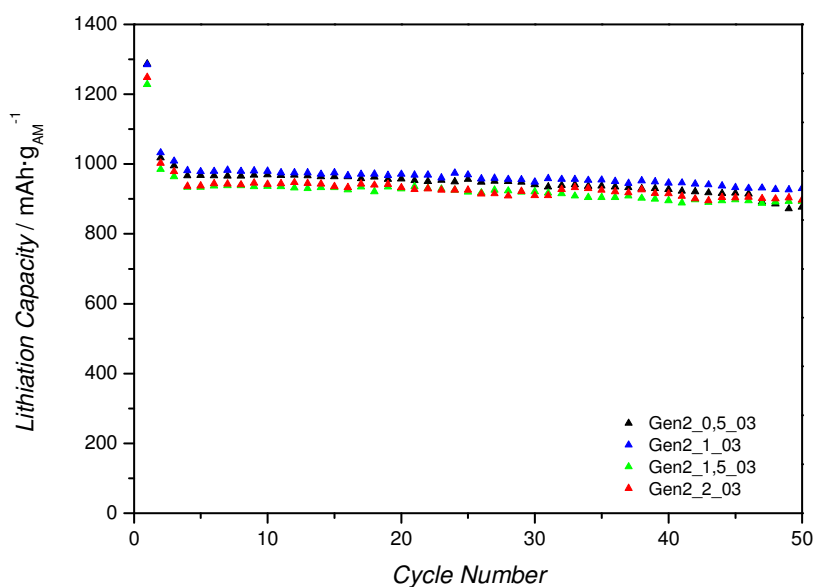


**Figure 47: Lithiation capacities received in CCC measurements of electrodes containing Gen2 materials fabricated with varied spray flow and constant pump speed (CCC1)**

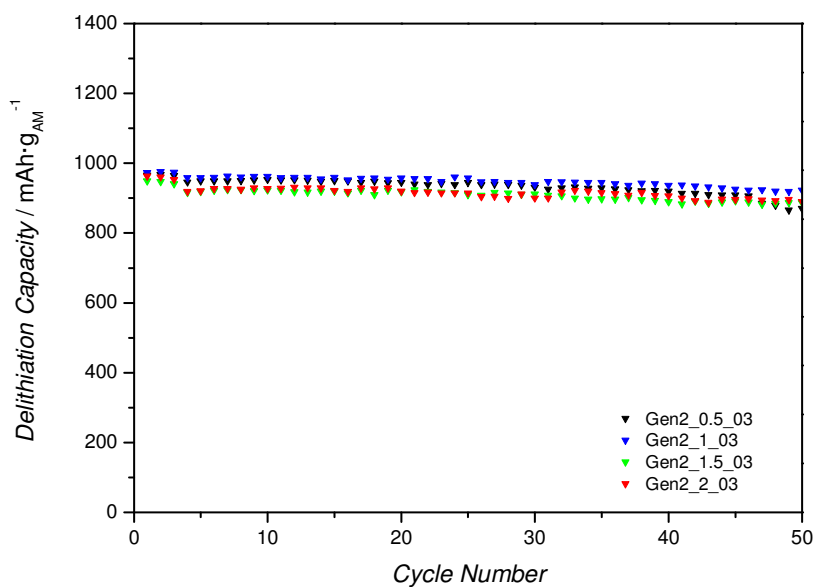


Figure 48: Delithiation capacities received in CCC measurements of electrodes containing Gen2 materials fabricated with varied spray flow and constant pump speed (CCC1)

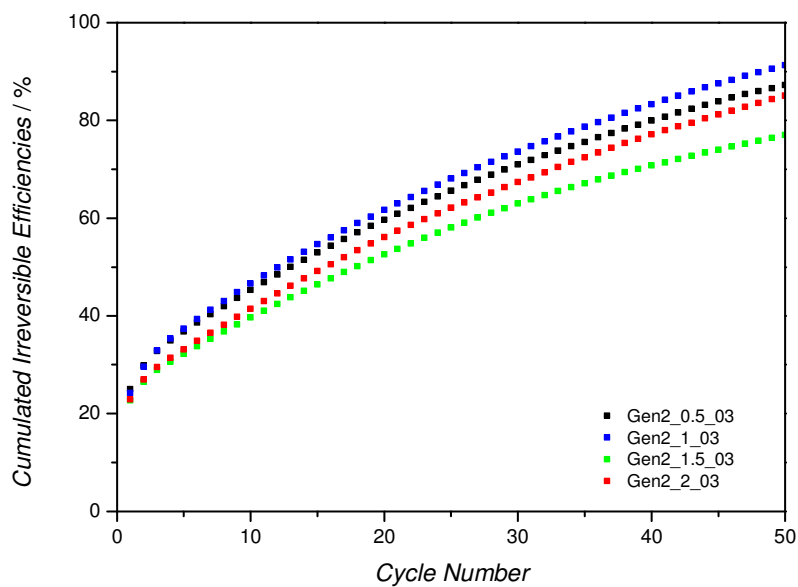


Figure 49: Cumulated irreversible efficiencies received in CCC measurements of electrodes containing Gen2 materials fabricated with varied spray flow and constant pump speed (CCC1)

The achieved capacities of the Gen2\_1\_03 material are slightly higher than the capacities of the Gen2\_1.5\_03 and Gen2\_2\_03 materials compared to their theoretical capacities. Furthermore, the lowest increase of the cumulated irreversible efficiencies is displayed by the Gen2\_1.5\_03 material, while Gen2\_1\_03 material shows the highest increase. Overall the differences in the electrochemical performances of all four materials are not remarkable.

As the results did not indicate significant differences, the studies on the optimal pump speed were carried out with spray flow of 1 bar. This spray flow proved to be ideal to prevent blocking of the nozzle with cured product as well as plugging the filters.

**Table 27: Electrode weights of the following CCC measurements and calculated capacities of Gen2 materials fabricated with constant spray flow and varied pump speed**

Used Gen2 material	Electrode weight [mg·cm <sup>-2</sup> ]	Capacity [mAh·g <sub>AM</sub> <sup>-1</sup> ]
Gen2_1_01	0.801	946
Gen2_1_05	0.829	913
Gen2_1_10	0.805	957
Gen2_1_20	0.667	979
Gen2_1_03	0.932	935

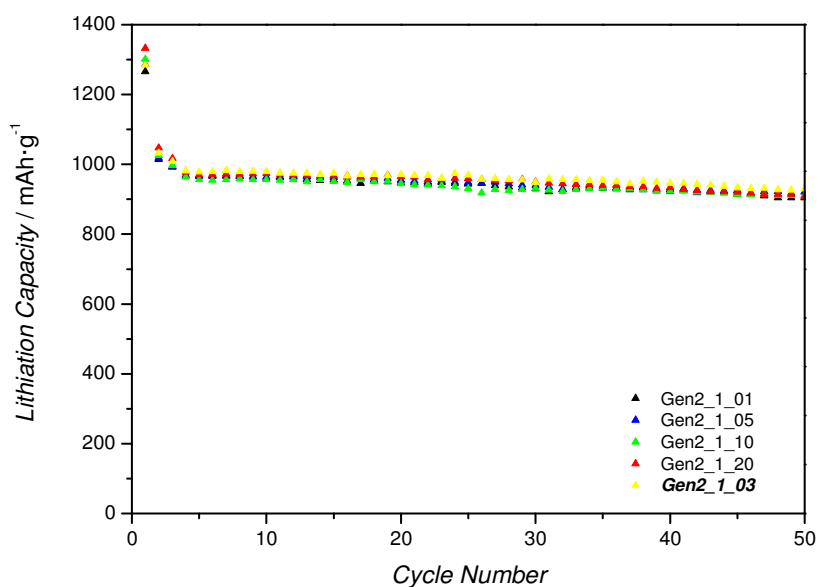


**Figure 50: Lithiation capacities received in CCC measurements of electrodes containing Gen2 materials fabricated with constant spray flow and varied pump speed (CCC1)**

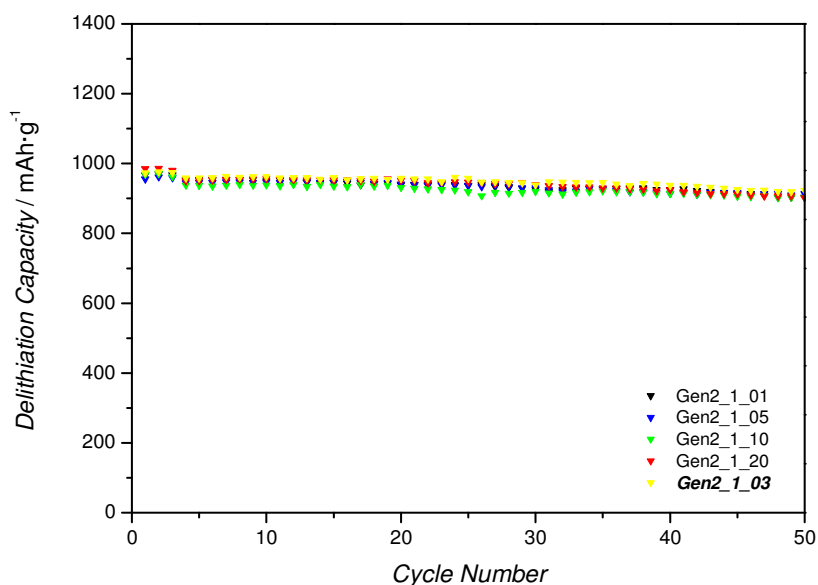


Figure 51: Delithiation capacities received in CCC measurements of electrodes containing Gen2 materials fabricated with constant spray flow and varied pump speed (CCC1)

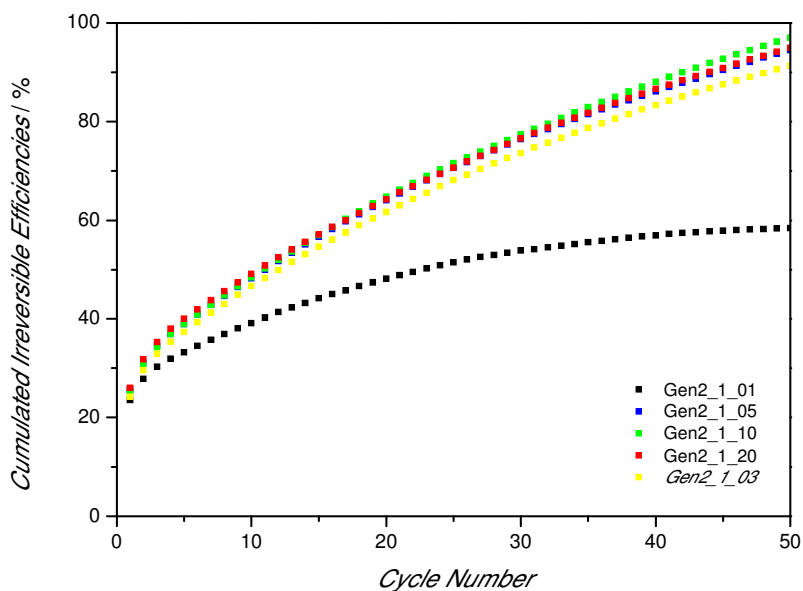


Figure 52: Cumulated irreversible efficiencies received in CCC measurements of electrodes containing Gen2 materials fabricated with constant spray flow and varied pump speed (CCC1)

According to the CCC measurement results above, the electrodes have almost the same reversible capacity performance. A very positive tendency of electrode performance is shown

by Gen2\_1\_01 material due to obviously lower cumulated irreversible efficiencies. This result allows the assessment that a low pump speed has a positive influence to the nature of the obtained active material.

#### 4.8.4 Influence of varied shell compositions

In this chapter the influence of varied shell compositions on Gen2 materials with regard to their electrochemical performance is represented. The following tests were carried out:

- Instead of nano-sized silicon particles in the range of 30-50 nm, silicon particles with an average particle size of 130 nm were used (Gen2\_Si130n)
- The silicon content was increased from 20 wt% of CNP to 25 wt% (Gen2\_Si25%)
- The 10 wt% carbon black of CNP was replaced by 10 wt% CNT/carbon black mixture (Gen2\_CNT)
- A material without initial carbon black was produced (Gen2\_0C)

**Table 28: Electrode weights of the following CCC measurements and calculated capacities of Gen2 materials fabricated with varied shell compositions**

Used Gen2 material	Electrode weight [mg·cm <sup>-2</sup> ]	Capacity [mAh·g <sub>AM</sub> <sup>-1</sup> ]
Gen2_4	0.924	946
Gen2_Si130n	0.847	891
Gen2_25%Si	0.943	1111
Gen2_0%C	0.911	1068
Gen2_CNT/C	1.088	935

**Table 29: Spray drying parameters of Gen2\_Si130n, Gen2\_Si25%, Gen2\_0C and Gen2\_CNT materials**

Parameter	
Process compressed air [bar]	0.07
Spray compressed air [bar]	1
Pump speed	03
Temperature [°C]	48-50
Heating time at 80 °C [h]	2
Nozzle diameter [mm]	0.5

#### 4.8.4.1 Influence of increasing silicon particle sizes

As mentioned above, for this test a powder was produced by using the Gen2 spray drying process and instead of the 30-50 nm silicon particles, particles with an average size of 130 nm were used. The fabricated powder (Gen2\_130n) was electrochemically characterized with CV and CCC measurements and subsequently compared to the analogously produced Gen2 material.

**Table 30: Composition of Gen2\_Si130n material**

EP/CNP ratio	EP and CNP composition	
40 wt% EP	80 wt%	Araldite <sup>®</sup> 506
	20 wt%	DAPA
60 wt% CNP	20 wt%	(APS 130nm) Silicon
	10 wt%	Carbon black
	70 wt%	Graphite
<b>1-Methoxy-2-propanol as solvent</b>		

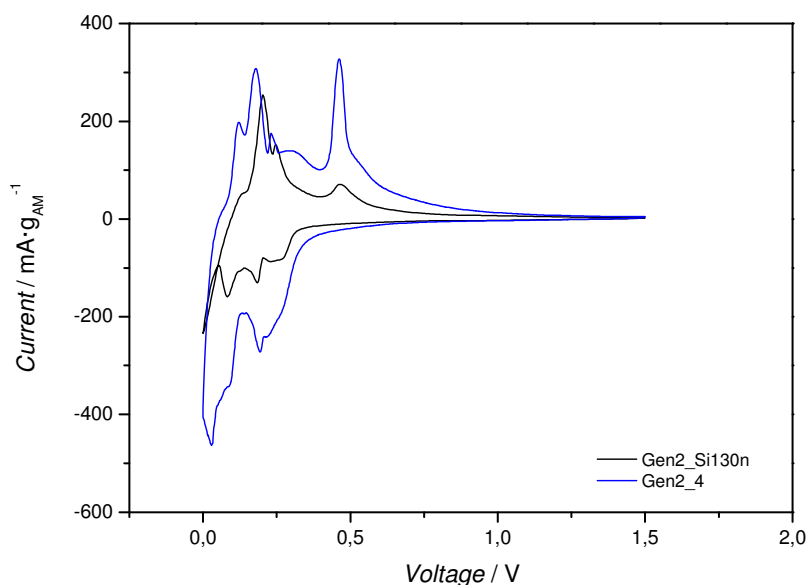


**Figure 53: Comparison of 3rd cycle of CV experiments of electrodes containing Gen2 materials with varied silicon particle sizes (CV1)**

Table 31: Corresponding delithiation/lithiation capacities and efficiencies of CV measurements (Figure 53)

Gen2_4				
Electrolyte: EC:DEC 3:7 1M LiPF <sub>6</sub> + 2% VC	Cycle	Delithiation [mAh·g <sub>AM</sub> <sup>-1</sup> ]	Lithiation [mAh·g <sub>AM</sub> <sup>-1</sup> ]	Efficiency [%]
El. weight [mg·cm <sup>-2</sup> ]: 1.024	1	723	942	77
	2	872	931	94
CNP <sub>after pyrolysis</sub> [wt%]: 86	3	895	936	96
	4	903	937	96
	5	912	942	97
Gen2_Si130n				
Electrolyte: EC:DEC 3:7 1M LiPF <sub>6</sub> + 2% VC	Cycle	Delithiation [mAh·g <sub>AM</sub> <sup>-1</sup> ]	Lithiation [mAh·g <sub>AM</sub> <sup>-1</sup> ]	Efficiency [%]
El. weight [mg·cm <sup>-2</sup> ]: 0.874	1	253	422	60
	2	351	403	87
CNP <sub>after pyrolysis</sub> [wt%]: 81	3	415	459	90
	4	451	490	92
	5	462	497	93

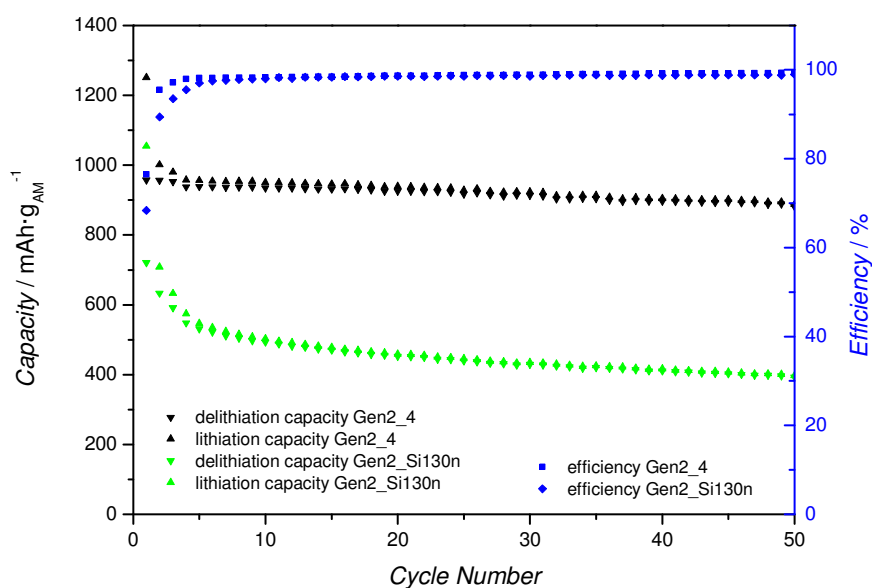


Figure 54: Delithiation/lithiation capacities and efficiencies received in CCC measurements of electrodes containing Gen2 materials with varied silicon particle sizes (CCC1)

The change of the silicon particle size from 30-50 nm to 130 nm had an enormous impact on the electrochemical behaviour of the material. The CV as well as the CCC measurement results show that the capacities of Gen2\_Si130n material start lower and achieve only approximately the half of the capacities of Gen2\_4 material. Both, the efficiencies and the capacity fading of Gen2\_Si130n electrode indicate that the material is less effective to store

lithium-ions reversibly. One reason for the poor electrochemical performance compared to Gen2\_4 is caused by the fact that larger-sized silicon particles undergo higher absolute volume changes, which leads to an increase of pulverisation and results in conductivity loss of the silicon particles. [110]

#### 4.8.4.2 Influence of increasing silicon content

In this chapter the change in the electrochemical behaviour of Gen2 materials due to increasing content of the silicon is represented.

**Table 32: Composition of Gen2\_Si25% material**

EP/CNP ratio	EP and CNP composition	
40 wt% EP	80 wt%	Araldite <sup>®</sup> 506
	20 wt%	DAPA
60 wt% CNP	25 wt%	nano-sized Silicon
	10 wt%	Carbon black
	65 wt%	Graphite
<b>1-Methoxy-2-propanol as solvent</b>		

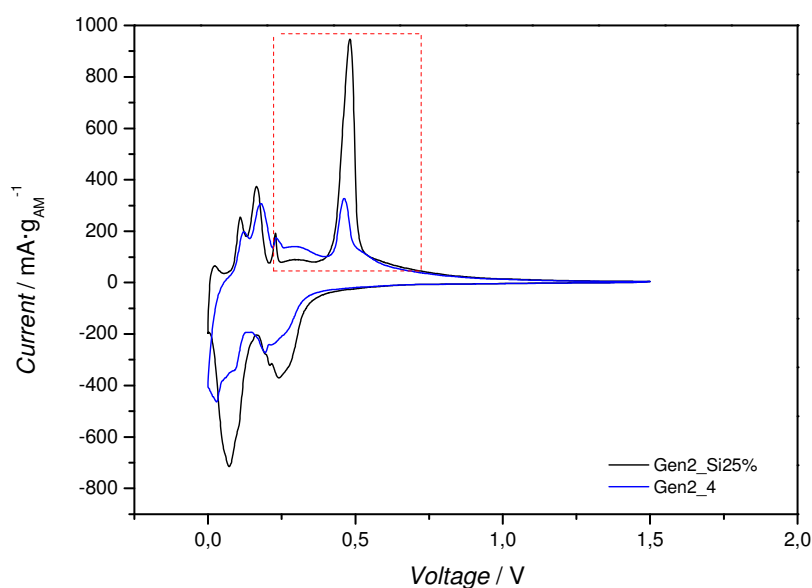


**Figure 55: Comparison of 3rd cycle of CV experiments of electrodes containing Gen2 materials with varied silicon contents (CV1)**

Table 33: Corresponding delithiation/lithiation capacities and efficiencies of CV measurements (Figure 55)

Gen2_4				
Electrolyte: EC:DEC 3:7 1M LiPF <sub>6</sub> + 2% VC	Cycle	Delithiation [mAh·g <sub>AM</sub> <sup>-1</sup> ]	Lithiation [mAh·g <sub>AM</sub> <sup>-1</sup> ]	Efficiency [%]
El. weight [mg·cm <sup>-2</sup> ]: 1.024	1	723	942	77
	2	872	931	94
CNP <sub>after Pyrolysis</sub> [wt%]: 86	3	895	936	96
	4	903	937	96
	5	912	942	97
Gen2_Si25%				
Electrolyte: EC:DEC 3:7 1M LiPF <sub>6</sub> + 2% VC	Cycle	Delithiation [mAh·g <sub>AM</sub> <sup>-1</sup> ]	Lithiation [mAh·g <sub>AM</sub> <sup>-1</sup> ]	Efficiency [%]
El. weight [mg·cm <sup>-2</sup> ]: 0.973	1	954	1143	83
	2	1107	1187	93
CNP <sub>after Pyrolysis</sub> [wt%]: 86	3	1092	1135	96
	4	1086	1123	97
	5	1080	1119	97

The silicon delithiation peaks (red framed area) are rising with the increasing silicon content in case of Gen2\_Si25% material, as can be seen from figure 55.

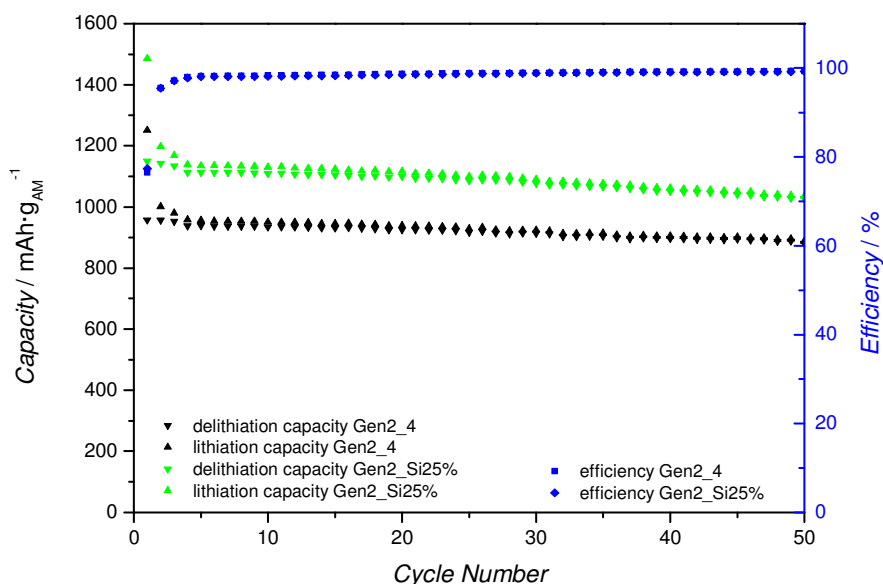


Figure 56: Delithiation/lithiation capacities and efficiencies received in CCC measurements of electrodes containing Gen2 materials with varied silicon contents (CCC1)

Both, the Gen2\_4 material as well as Gen2\_Si25% material achieve respectable capacity retention close to their theoretical capacities. A slight tendency of increasing capacity fading is measurable in case of the Gen2\_Si25% material compared to the Gen2\_4 material. This increasing capacity fading can be explained by the higher content of electrochemically active silicon compared to the structural stabilizing carbonaceous matrix.

#### 4.8.4.3 Influence of varied carbonaceous matrix compositions

The influence of changed carbonaceous matrix compositions on the electrochemical behaviour of Gen2 materials was determined with the help of the following two powders.

1. Therefore, a powder was fabricated that contained 10 wt% carbon nanotubes (CNT)/carbon black mixture instead of the 10 wt% carbon black (in the CNP).
2. Furthermore, a powder, which didn't contain any carbon black (in the CNP), was produced according to the Gen2 procedure.

**Table 34: Compositions of Gen2\_CNT and Gen2\_0C materials**

Gen2_CNT/C			Gen2_0C		
40 wt% EP	80 wt%	Araldite <sup>®</sup> 506	40 wt% EP	80 wt%	Araldite <sup>®</sup> 506
	20 wt%	DAPA		20 wt%	DAPA
60 wt% CNP	20 wt%	nano-sized Silicon	60 wt% CNP	22 wt%	nano-sized Silicon
	10 wt%	CNT/carbon black mixture		78 wt%	Graphite
	70 wt%	Graphite			
1-Methoxy-2-propanol as solvent			1-Methoxy-2-propanol as solvent		

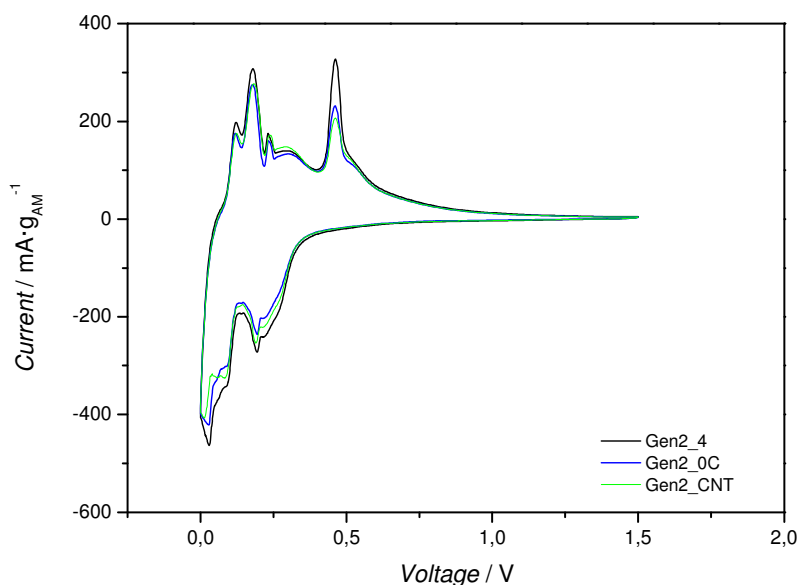


Figure 57: Comparison of 3rd cycle of CV experiments of electrodes containing Gen2 materials with varied carbonaceous matrix compositions (CV1)

Table 35: Corresponding delithiation/lithiation capacities and efficiencies of CV measurements (Figure 57)

Gen2_4				
Electrolyte: EC:DEC 3:7 1M LiPF <sub>6</sub> + 2% VC	Cycle	Delithiation [mAh·g <sub>AM</sub> <sup>-1</sup> ]	Lithiation [mAh·g <sub>AM</sub> <sup>-1</sup> ]	Efficiency [%]
El. weight [mg·cm <sup>-2</sup> ]: 1.024	1	723	942	77
	2	872	931	94
CNP <sub>after pyrolysis</sub> [wt%]: 86	3	895	936	96
	4	903	937	96
	5	912	942	97
Gen2_OC				
Electrolyte: EC:DEC 3:7 1M LiPF <sub>6</sub> + 2% VC	Cycle	Delithiation [mAh·g <sub>AM</sub> <sup>-1</sup> ]	Lithiation [mAh·g <sub>AM</sub> <sup>-1</sup> ]	Efficiency [%]
El. weight [mg·cm <sup>-2</sup> ]: 0.937	1	629	871	72
	2	815	872	93
CNP <sub>after pyrolysis</sub> [wt%]: 88	3	878	919	96
	4	901	935	96
	5	917	946	97
Gen2_CNT				
Electrolyte: EC:DEC 3:7 1M LiPF <sub>6</sub> + 2% VC	Cycle	Delithiation [mAh·g <sub>AM</sub> <sup>-1</sup> ]	Lithiation [mAh·g <sub>AM</sub> <sup>-1</sup> ]	Efficiency [%]
El. weight [mg·cm <sup>-2</sup> ]: 1.026	1	621	858	72
	2	776	827	94
CNP <sub>after pyrolysis</sub> [wt%]: 85	3	809	845	96
	4	824	853	97
	5	829	854	97

Comparing the results obtained from the CV measurements of Gen2\_4, Gen2\_0C and Gen2\_CNT/C, all electrodes achieve capacities close to their theoretical capacities (Table 28). More precisely, the Gen2\_4 material displays a slightly higher and Gen2\_0C material slightly lower capacity performance.

This tendency to higher capacities of Gen2\_4 material can also be confirmed by the CCC measurement results (Figure 58 and figure 59). Concerning the cumulated irreversible efficiency after 50 cycles the best results can be obtained by Gen2\_CNT/C material. In contrast to Gen2\_0C material exhibits the highest cumulated irreversible efficiency.

This result allows the interpretation that initial conductivity additives like carbon black and CNT/C mixture improve the particle conductivity and support the embedding of the silicon particles.

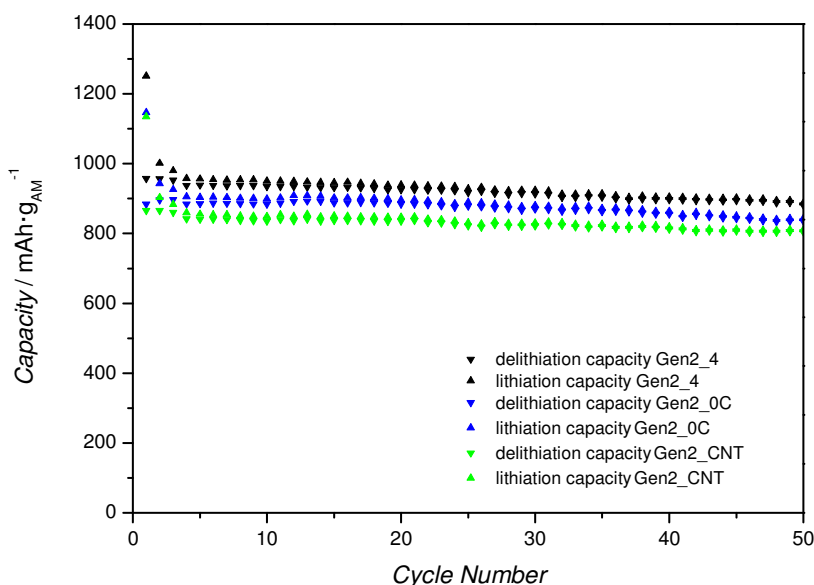


**Figure 58: Delithiation/lithiation capacities received in CCC measurements of electrodes containing Gen2 materials with varied carbonaceous matrix compositions (CCC1)**

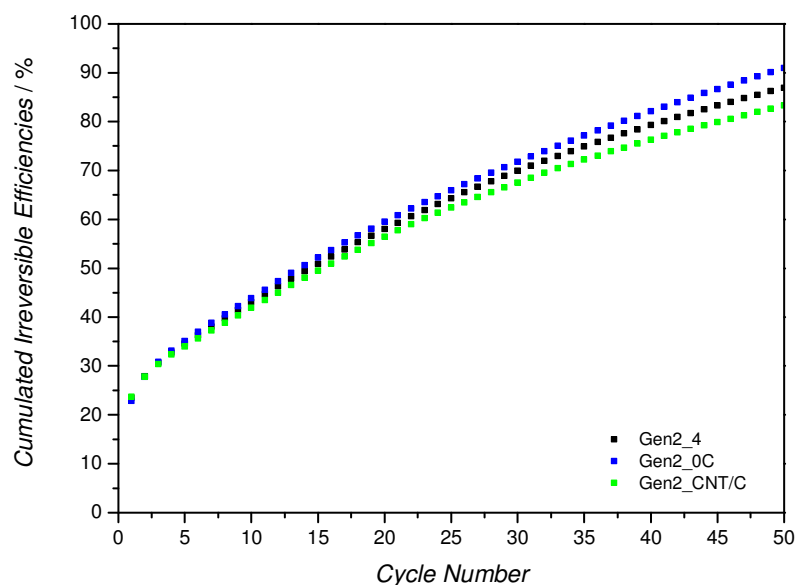


Figure 59: Cumulated irreversible efficiencies received in CCC measurements of electrodes containing Gen2 materials with varied carbonaceous matrix compositions (CCC1)

#### 4.8.5 Further development of Gen2 materials

The inhomogeneous PSD, obvious in figure 60 and figure 61, is an undesired effect of Gen2 materials. This means that the Gen2 materials consist of graphite particles coated with various qualities of the silicon/amorphous carbon shells and small pure silicon/amorphous carbon agglomerates. Furthermore, this inhomogeneous distribution in case of Gen2 materials may cause unequal electrochemical activities at different electrode areas as well as varied electrode surface or porosity. To prevent this broad PSD and to fabricate high homogenous particles a new fabrication technique was applied. For this new material fabrication technique (Gen3) a special method (“wurster-method”) for particle coating in a fluidized bed reactor was used. The research on these new Gen3 materials will be described in the following chapters.

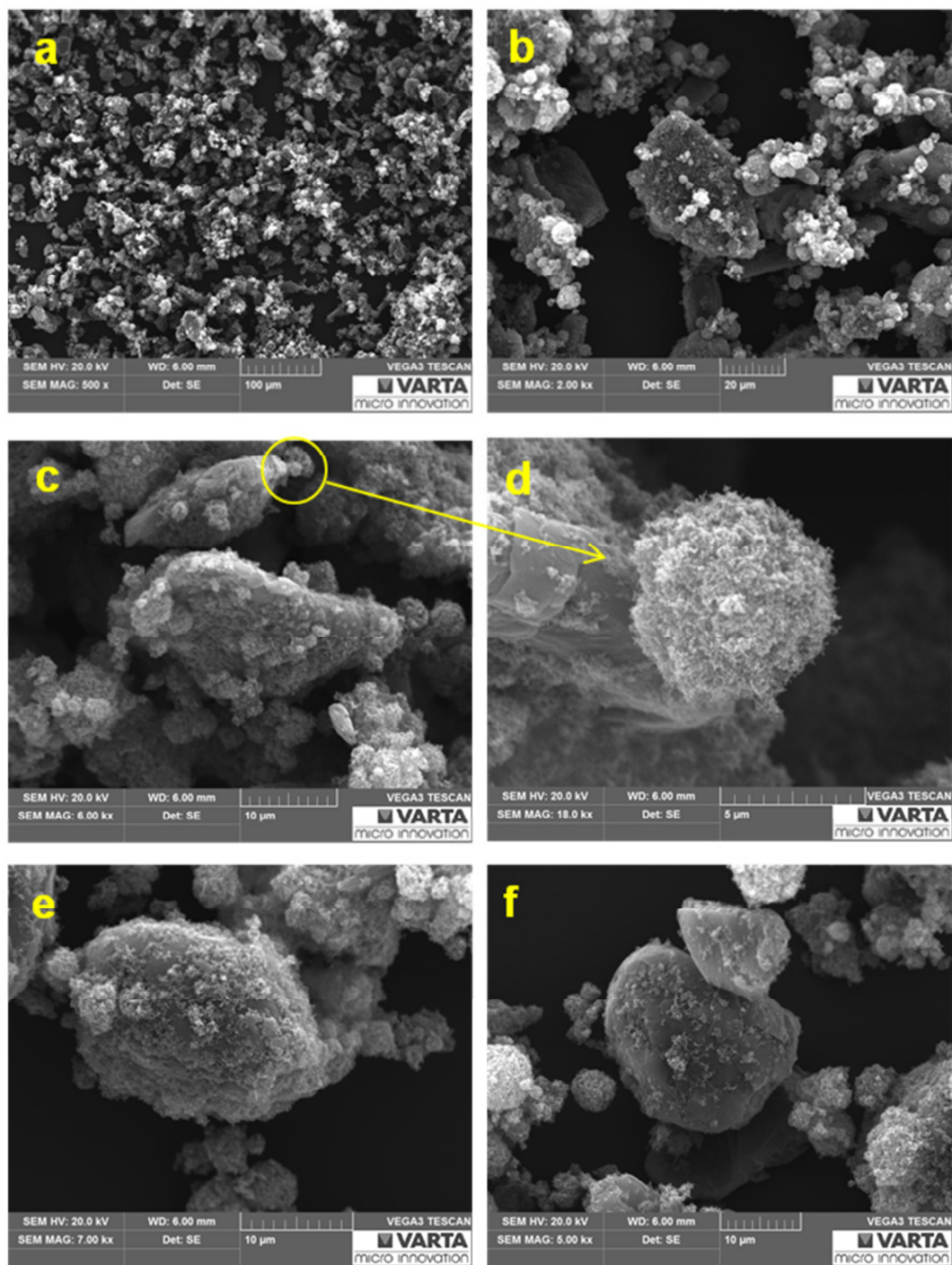


Figure 60: SEM pictures of Gen2\_4 powder (a) with 500x (b) with 2000x magnification (c)+(e) with high quality coated graphite particles, (d) small pure silicon/amorphous carbon agglomerate and (f) poor coated graphite particle

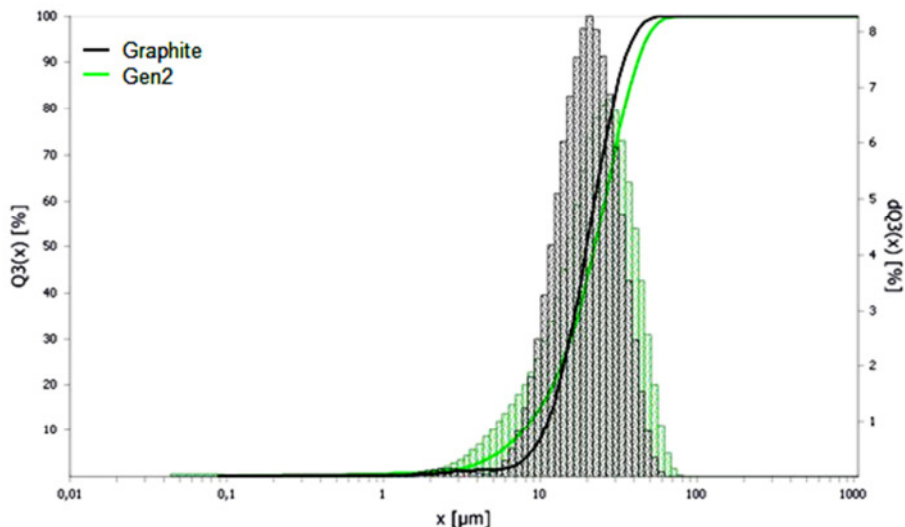


Figure 61: Particle size distributions of a Gen2 material and graphite

### 4.9 Generation 3 of silicon-graphite composite particles

The main focus of the further development of materials was to achieve a uniform graphite particle coating with a homogenous core-shell structure. To reach such homogenous particle coating the “wurster-method” was used instead of spray drying. A detailed description of the “wurster-method” can be found in chapter 4.4. In figure 62 an example of one Gen3 material is displayed.



Figure 62: SEM pictures of a Gen3 powder

### 4.9.1 Fabrication procedure

Table 36 describes the main fabrication process steps for Gen3 materials.

**Table 36: Procedure of Gen3 materials fabrication**

Step 1 to 3	Step 1 to 3 were equal to step1 to step3 of Gen1 fabrication (except step3 for 3h instead of 2h) (see table 13)
Step 4	Coating process (according to wurster-method): <ul style="list-style-type: none"> <li>➤ The graphite was submitted in the fluidized bed reactor</li> <li>➤ The process was started and heated for 3h to get stabilized cycling of the graphite particles. Thereafter, the coating material solution, consisting of the mixture of epoxy resin, silicon and carbon black, was dissolved in 1-methoxy-2-propanol and sprayed into the fluidized graphite bed</li> </ul>
Step 5	The dried and cured particles were transferred into a tube furnace and pyrolysed (Tube furnace parameters according to table 14)
Step 6	Electrode preparation according to table 9

### 4.9.2 Varying parameters and their influences on Gen3 materials

Unfortunately an adaption of the optimized material composition of the Gen2 fabrication process was not possible for Gen3 materials, due to the limitation of the wurster-method by the maximum amount of EP. At an EP content of 30 wt% to 70 wt% CNP the entire product agglomerated on the bottom of the product container and thereby blocked the distributor plate and the two component nozzle. Most likely the blockage was caused by slow curing of the initial epoxy resin due to too high content, which acted as a quasi-adhesive and caused huge agglomeration of the particles. Figure 63 displays the product obtained by preparation of a Gen3 powder with an initial epoxy resin of 30 wt%. It is clearly evident that in this case the graphite particles were not coated.

To get an overview on electrochemical differences of varied coated graphite particles, Gen3 powders were fabricated with various shell thicknesses and compositions. Powders, synthesized according to the Gen3 technique, are listed in table 37.

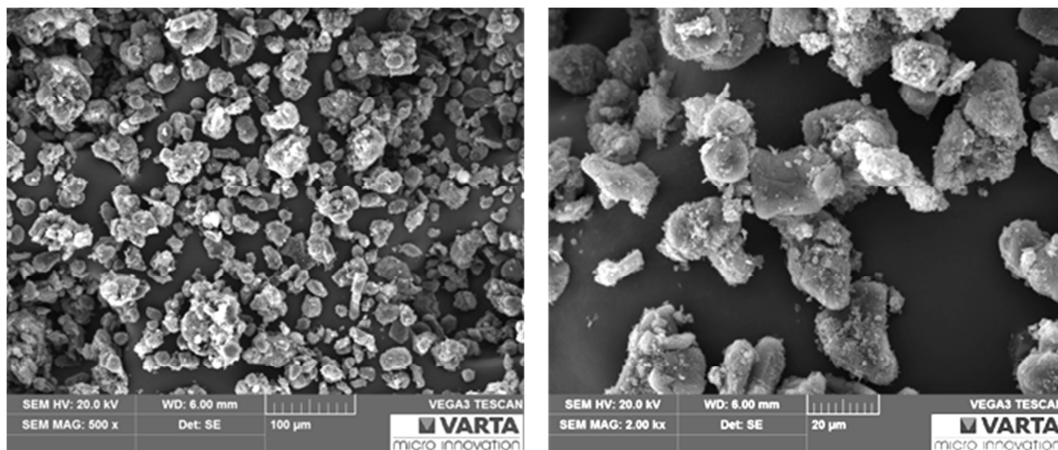


Figure 63: SEM pictures of Gen3 powder fabricated with an initial epoxy resin content of 30 wt%

Table 37: Compositions before pyrolysis of different Gen3 materials

<i>Gen3_1</i>			
2 wt% EP		98 wt% CNP	
Araldite	80 wt%	Graphite	97 wt%
DAPA	20 wt%	nano-sized Silicon	2.5 wt%
		Carbon black	0.5 wt%
<i>Gen3_2</i>			
4 wt% EP		96 wt% CNP	
Araldite	80 wt%	Graphite	94 wt%
DAPA	20 wt%	nano-sized Silicon	5 wt%
		Carbon black	1 wt%
<i>Gen3_3</i>			
8 wt% EP		92 wt% CNP	
Araldite	80 wt%	Graphite	87 wt%
DAPA	20 wt%	nano-sized Silicon	11 wt%
		Carbon black	2 wt%
<i>Gen3_4</i>			
20 wt% EP		80 wt% CNP	
Araldite	80 wt%	Graphite	70 wt%
DAPA	20 wt%	nano-sized Silicon	20 wt%
		Carbon black	10 wt%
<i>Gen3_5</i>			
20 wt% EP		80wt% CNP	
Araldite	80 wt%	Graphite	60 wt%
DAPA	20 wt%	nano-sized Silicon	30 wt%
		Carbon black	10 wt%
<i>Gen3_6</i>			
20 wt% EP		80 wt% CNP	
Araldite	80 wt%	Graphite	80 wt%
DAPA	20 wt%	nano-sized Silicon	20 wt%
		Carbon black	0 wt%

Table 38: EP/CNP ratios before and CM/CNP ratios after pyrolysis of different Gen3 materials

Name	Before pyrolysis		After pyrolysis	
	EP [wt%]	CNP [wt%]	CM [wt%]	CNP [wt%]
Gen3_1	2	98	1.5	98.5
Gen3_2	4	96	2	98
Gen3_3	8	92	4	96
Gen3_4	20	80	5	95
Gen3_5	20	80	5	95
Gen3_6	20	80	8	92

Table 39: Calculated capacities of different Gen3 materials

Used Gen3 material	Capacity [mAh·g <sub>AM</sub> <sup>-1</sup> ]
Gen3_1	459
Gen3_2	548
Gen3_3	754
Gen3_4	1045
Gen3_5	1409
Gen3_6	1047
Graphite	372

Table 40: Fluidized bed reactor parameters of Gen3 materials fabricated with different compositions

Parameter	Gen3_1 to Gen3_6
Process compressed air [bar]	0.1
Spray compressed air [bar]	0.07
Pump speed [rpm]	03
Temperature [°C]	41-47
Heating time at 80 °C [h]	3
Nozzle diameter [mm]	0.8

### 4.9.2.1 Influence of increasing shell thickness/silicon content

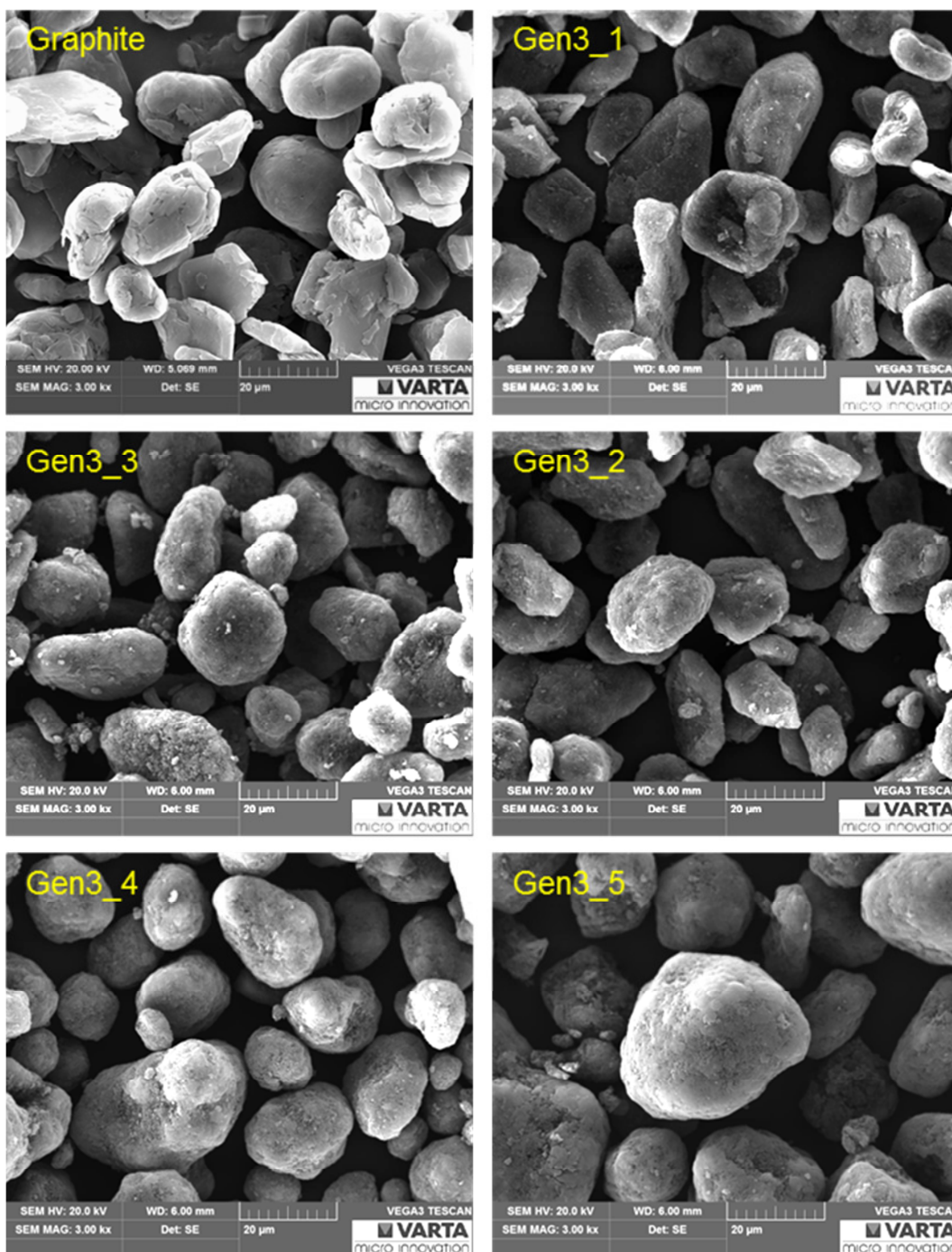
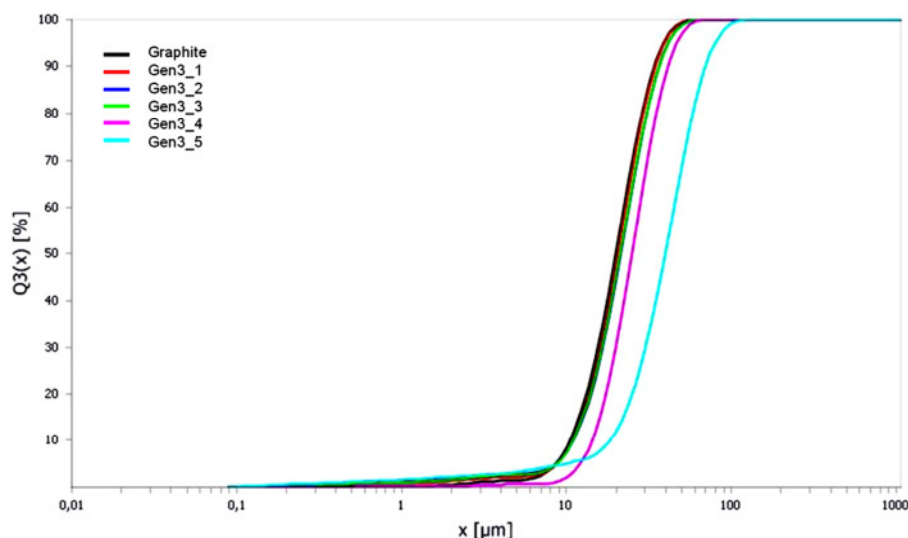


Figure 64: SEM pictures of different Gen3 materials at 3000x magnification



**Figure 65: Particle size distributions of Gen3 materials with different compositions and graphite**

The ratio of shell components to coated graphite core particles is increasing in the order Gen3\_1  $\Rightarrow$  Gen3\_2  $\Rightarrow$  Gen3\_3  $\Rightarrow$  Gen3\_4  $\Rightarrow$  Gen3\_5 (Table 37) and therefore the particles shell thickness should increase in this order as well. This tendency is already indicated by the SEM pictures in figure 64 and is additionally represented by the PSDs of these materials in figure 65. The rising shell thickness results in an increase of the particle sizes, which can be confirmed by PSD curves of the different Gen3 materials. According to their PSDs, the particle sizes of Gen3\_1 and Gen3\_2 material are close to the particle sizes of the graphite powder (core particles). This in turn displays the low shell thickness of these two materials, caused by the low content of shell components to core particles. The first remarkable shift to larger particle sizes is shown by Gen3\_4 and Gen3\_5 powders. The conspicuously higher particle sizes in case of Gen3\_5 are the result of an agglomeration of several coated particles. Figure 66 displays some of the larger agglomerates, which can be found in the Gen3\_5 material.

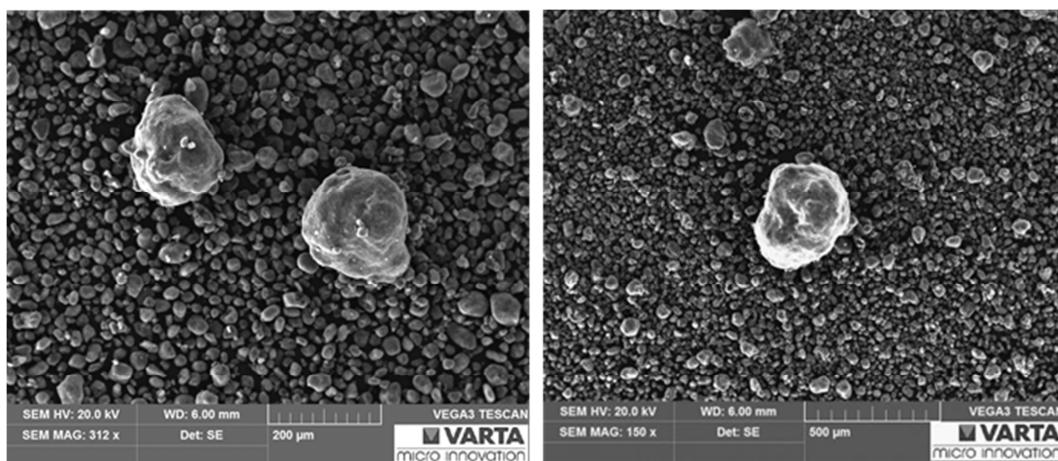


Figure 66: Huge visible agglomerates contained in Gen3\_5 material

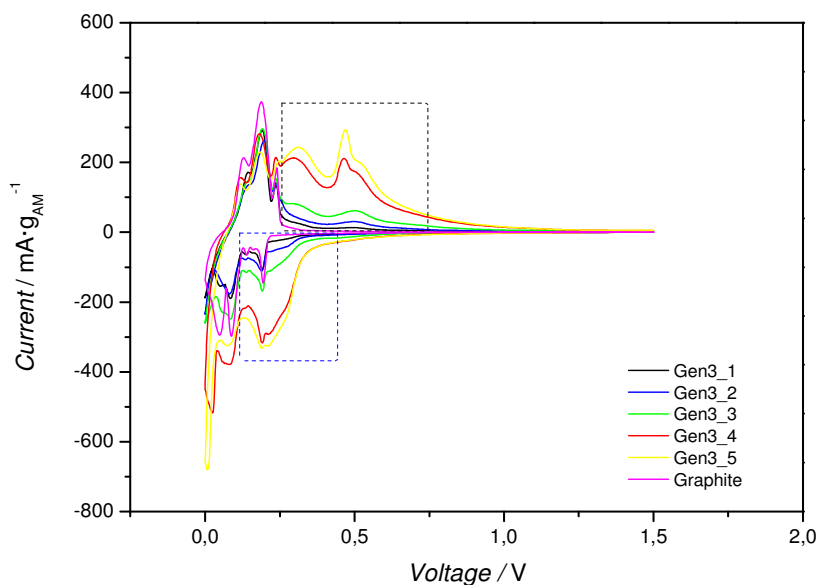


Figure 67: Comparison of 3rd cycle of CV experiments of electrodes containing Gen3 materials with different silicon contents (CV1)

Table 41: Corresponding delithiation/lithiation capacities and efficiencies of CV measurements (Figure 67)

Gen3_1				
Electrolyte: EC:DEC 3:7 1M LiPF <sub>6</sub> + 2% VC	Cycle	Delithiation [mAh·g <sub>AM</sub> <sup>-1</sup> ]	Lithiation [mAh·g <sub>AM</sub> <sup>-1</sup> ]	Efficiency [%]
El. weight [mg·cm <sup>-2</sup> ]: 0.994	1	231	312	74
CNP <sub>after pyrolysis</sub> [wt%]: 98.5	2	280	295	95
	3	298	311	96
Gen3_2				
Electrolyte: EC:DEC 3:7 1M LiPF <sub>6</sub> + 2% VC	Cycle	Delithiation [mAh·g <sub>AM</sub> <sup>-1</sup> ]	Lithiation [mAh·g <sub>AM</sub> <sup>-1</sup> ]	Efficiency [%]
El. weight [mg·cm <sup>-2</sup> ]: 1.050	1	248	344	72
CNP <sub>after pyrolysis</sub> [wt%]: 98	2	328	350	94
	3	350	367	95
Gen3_3				
Electrolyte: EC:DEC 3:7 1M LiPF <sub>6</sub> + 2% VC	Cycle	Delithiation [mAh·g <sub>AM</sub> <sup>-1</sup> ]	Lithiation [mAh·g <sub>AM</sub> <sup>-1</sup> ]	Efficiency [%]
El. weight [mg·cm <sup>-2</sup> ]: 0.999	1	406	573	71
CNP <sub>after pyrolysis</sub> [wt%]: 96	2	482	530	91
	3	500	536	93
Gen3_4				
Electrolyte: EC:DEC 3:7 1M LiPF <sub>6</sub> + 2% VC	Cycle	Delithiation [mAh·g <sub>AM</sub> <sup>-1</sup> ]	Lithiation [mAh·g <sub>AM</sub> <sup>-1</sup> ]	Efficiency [%]
El. weight [mg·cm <sup>-2</sup> ]: 0.865	1	784	1043	75
CNP <sub>after pyrolysis</sub> [wt%]: 95	2	941	1008	93
	3	980	1028	95
Gen3_5				
Electrolyte: EC:DEC 3:7 1M LiPF <sub>6</sub> + 2% VC	Cycle	Delithiation [mAh·g <sub>AM</sub> <sup>-1</sup> ]	Lithiation [mAh·g <sub>AM</sub> <sup>-1</sup> ]	Efficiency [%]
El. weight [mg·cm <sup>-2</sup> ]: 0.750	1	766	1059	72
CNP <sub>after pyrolysis</sub> [wt%]: 95	2	1001	1059	95
	3	1088	1129	96

The CV measurements reflect the predicted results of higher achievable capacities by increasing silicon content. This is also clearly indicated by the rising silicon delithiation (black framed) as well as lithiation (blue framed) peaks with increasing silicon content in figure 67. This effect can further be confirmed by CCC measurements.

Table 42: Electrode weights of the following CCC measurements of Gen3 materials fabricated with different silicon contents

Used Gen3 material	Electrode weight [mg·cm <sup>-2</sup> ]
Gen3_1	0.941
Gen3_2	1.066
Gen3_3	0.999
Gen3_4	0.871
Gen3_5	0.732
Graphite	0.884

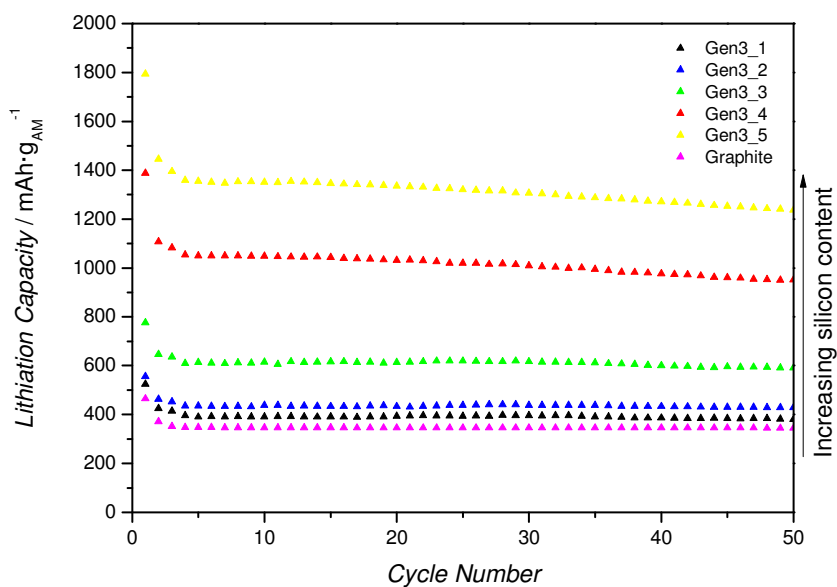


Figure 68: Lithiation capacities received in CCC measurements of electrodes containing Gen3 materials with different silicon contents (CCC1)

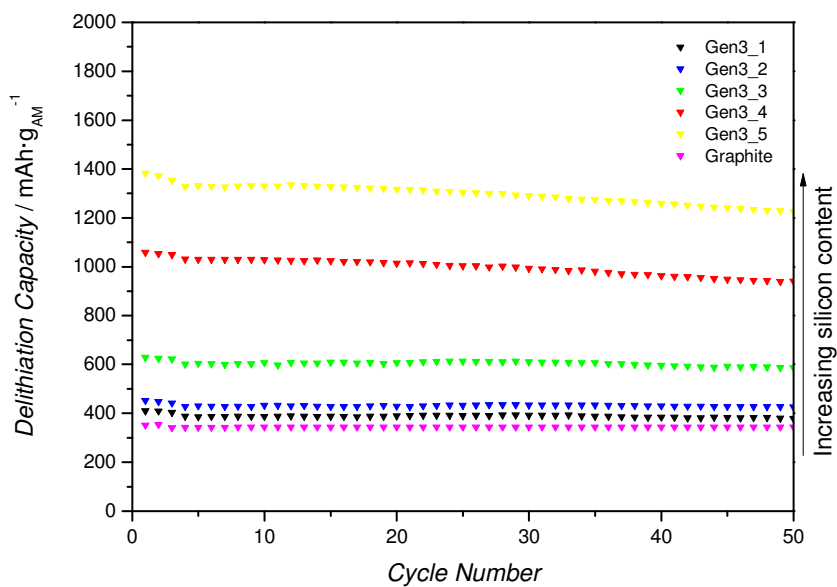
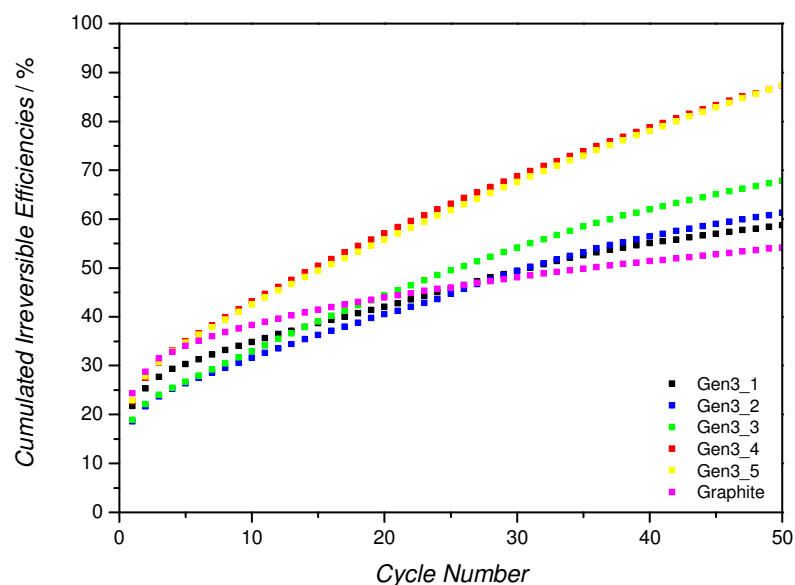


Figure 69: Delithiation capacities received in CCC measurements of electrodes containing Gen3 materials with different silicon contents (CCC1)



**Figure 70: Cumulated irreversible efficiencies received in CCC measurements of electrodes containing Gen3 materials with different silicon contents (CCC1)**

The CCC measurement results (Figure 68) confirm the CV measurement results, as capacities increase with higher content of silicon.

After the first five cycles, the pure graphite electrode displays a higher cumulated irreversible efficiency than the Gen3 electrodes but subsequently the cumulated irreversible efficiency curve of the graphite electrode flattens (Figure 70). A similar behaviour is shown by the electrode Gen3\_1. This isn't surprising due to the low silicon content of Gen3\_1 material, so its electrochemical behaviour is more determined by graphite than by silicon. Conversely, a rising cumulated irreversible efficiency with increasing cycle number is observed from Gen3\_2 to Gen3\_5 electrode. The comparable cumulated irreversible efficiencies of Gen3\_4 and Gen3\_5 materials can be attributed by the lower electrode weight of Gen3\_5 electrode compared to Gen3\_4 electrode (positive influence on the electrochemical behaviour, due to minor diffusion length in the solid phase [111] [112]).

The higher electrochemically active surfaces, caused by the increased silicon content of the materials, lead to an increased loss of irreversible capacity due to the SEI formation within the first cycles. This assumption can be confirmed by taking into account the BET-measurements, which are listed in table 43. [113]

Furthermore, the higher silicon content can be directly related with higher current loads and therefore elevated mechanical stresses, which can be observed by increased capacity fading in following order Gen3\_1  $\Rightarrow$  Gen3\_2  $\Rightarrow$  Gen3\_3  $\Rightarrow$  Gen3\_4  $\Rightarrow$  Gen3\_5.

**Table 43: BET surfaces of different Gen3 materials, graphite and nano-sized silicon**

Material	BET surface [m <sup>2</sup> g <sup>-1</sup> ]
Graphite	4.85
Gen3_1	5.96
Gen3_2	8.31
Gen3_3	11.87
Gen3_4	21.33
Gen3_5	26.14
nano-sized Silicon	63.04

#### 4.9.2.2 Influence of initial carbon black

To determine the influence of the presence of initial carbon black in the CNP, a Gen3 material without initial carbon black (Gen3\_6 material) was fabricated and electrochemically characterized. Furthermore, the electrochemical results of Gen3\_6 material were compared with the electrochemical results of a Gen3 material containing initial carbon black (Gen3\_4).

The composition of Gen3\_6 material and coating process parameters can be found in table 37 and table 40.

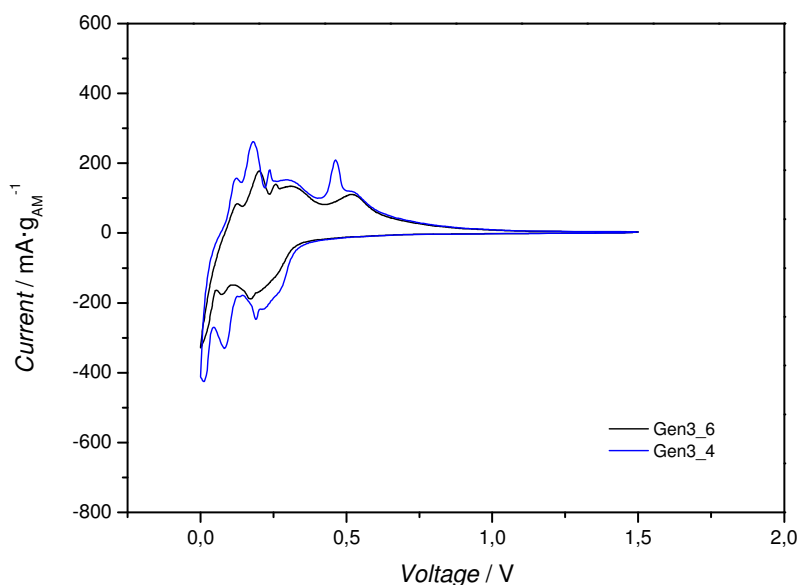


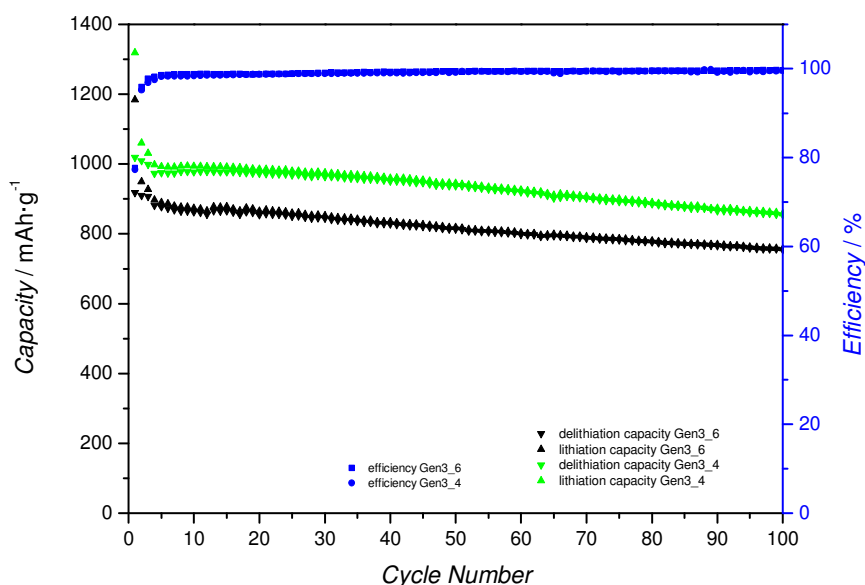
Figure 71: Comparison of 3rd cycle of CV experiments of electrodes containing Gen3 materials with different shell compositions (CV1)

Table 44: Corresponding delithiation/lithiation capacities and efficiencies of CV measurements (Figure 71)

Gen3_6				
Electrolyte: EC:DEC 3:7 1M LiPF <sub>6</sub> + 2% VC	Cycle	Delithiation [mAh·g <sub>AM</sub> <sup>-1</sup> ]	Lithiation [mAh·g <sub>AM</sub> <sup>-1</sup> ]	Efficiency [%]
El. weight [mg·cm <sup>-2</sup> ]: 0.865	1	462	632	73
	2	524	557	94
	3	611	639	96
CNP <sub>after pyrolysis</sub> [wt%]: 92	4	674	699	96
	5	703	727	97
Gen3_4				
Electrolyte: EC:DEC 3:7 1M LiPF <sub>6</sub> + 2% VC	Cycle	Delithiation [mAh·g <sub>AM</sub> <sup>-1</sup> ]	Lithiation [mAh·g <sub>AM</sub> <sup>-1</sup> ]	Efficiency [%]
El. weight [mg·cm <sup>-2</sup> ]: 0.865	1	784	1043	75
	2	941	1008	93
	3	980	1028	95
CNP <sub>after pyrolysis</sub> [wt%]: 95	4	995	1035	96
	5	1003	1037	97

**Table 45: Electrode weights of the following CCC measurements and calculated capacities of Gen3 materials fabricated with different shell compositions**

Used Gen3 material	Electrode weight [ $\text{mg}\cdot\text{cm}^{-2}$ ]	Capacity [ $\text{mAh}\cdot\text{g}_{\text{AM}}^{-1}$ ]
Gen3_6	0.858	1047
Gen3_4	0.871	1045



**Figure 72: Delithiation/lithiation capacities and efficiencies received in CCC measurements of electrodes containing Gen3 materials with different shell compositions (CCC1)**

Both, the CV as well as CCC measurement results display a remarkably enhanced electrochemical performance of the Gen3 material (Gen3\_4) with initial carbon black compared to the Gen3 material (Gen3\_6) without initial carbon black. This obviously positive influence of the additional conductive additive is also shown in case of Gen2 materials, as can be seen in chapter 4.8.4.3.

### 4.9.3 Optimization of the coating process

The subject of this chapter is primarily an overview about the influence of varied reactor parameters for Gen3 materials. Powders with same compositions (Table 46) but with varied parameters in Gen3 fabrication process were synthesized and electrochemically characterized with CV and CCC measurements. At first, the materials were fabricated with constant pump speed and varied pressure of the spray flow and afterwards with constant pressure of the spray flow and varied pump speed. The maximum pressure was equal to 1.3 bar to protect the filters.

**Table 46: Compositions before pyrolysis of Gen3 materials fabricated with different process parameters**

Gen3_7 to Gen3_14			
10 wt% EP		90 wt% CNP	
Araldite	80 wt%	Graphite	85 wt%
DAPA	20 wt%	Nano-sized silicon	10 wt%
		Carbon black	5 wt%

**Table 47: Fluidized bed reactor parameters of Gen3 materials (Table 46)**

Constant Pump Speed				
Name	Gen3_7	Gen3_8	Gen3_9	Gen3_10
Process compressed air [bar]			0.1	
Spray compressed air [bar]	0.4	0.7	1	1.3
Pump speed [rpm]			03	
Temperature [°C]	49	45	42	42
Heating time at 80 °C [h]			3	
Nozzle diameter [mm]			0.8	
Constant Spray Flow				
Name	Gen3_11	Gen3_12	Gen3_13	Gen3_14
Process compressed air [bar]			0.1	
Spray compressed air [bar]			1.3	
Pump speed [rpm]	01	05	10	20
Temperature [°C]	42	40	41	40
Heating time at 80 °C [h]			3	
Nozzle diameter [mm]			0.8	

#### 4.9.3.1 Optimization of the coating process: Constant pump speed and varied pressure of spray flow

The results of the SEM investigations of the fabricated Gen3 materials at constant pump speed and varied pressure of spray flow are displayed in figure 73.

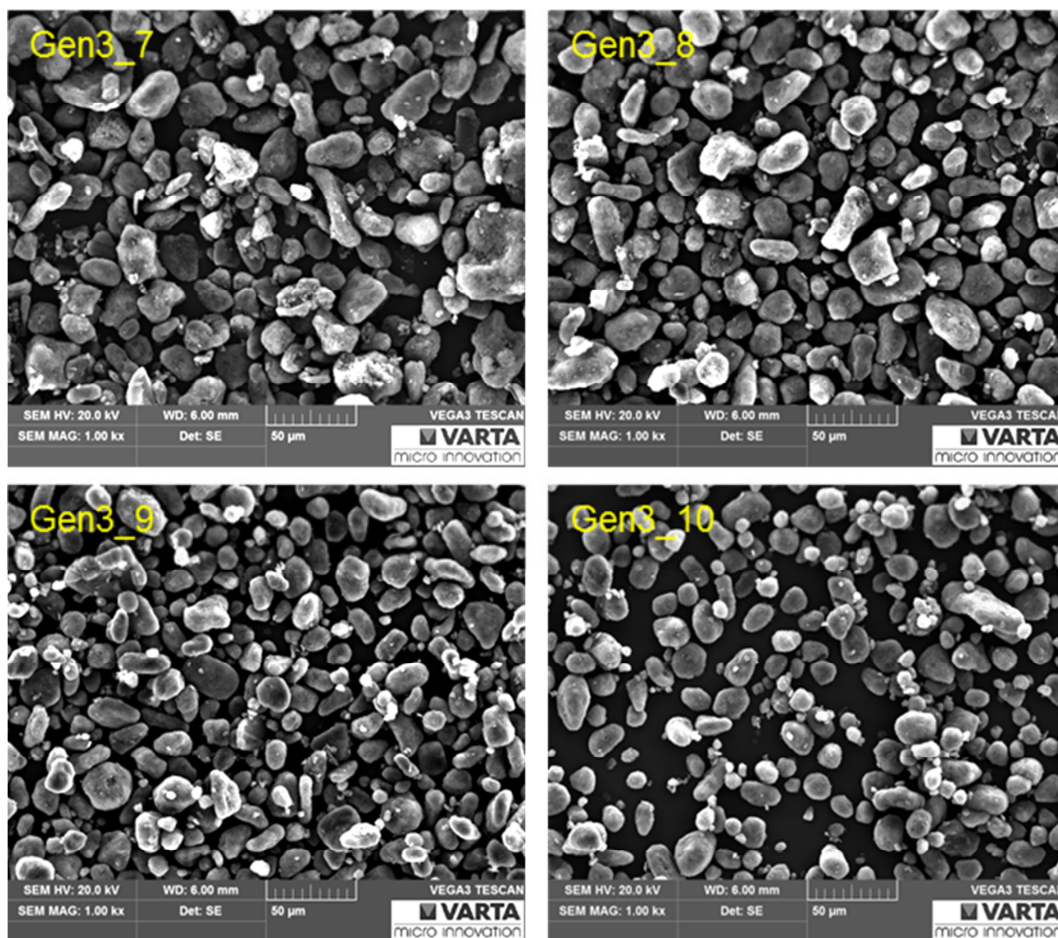
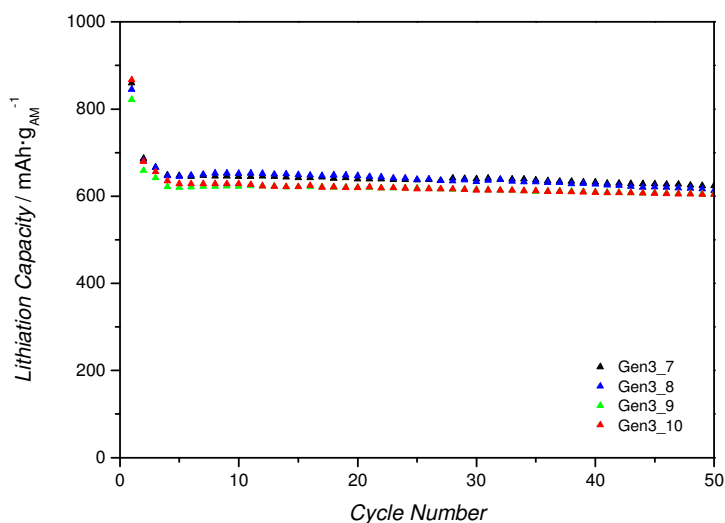


Figure 73: SEM pictures of Gen3 materials fabricated with constant pump speed and varied pressure of spray flow

Comparing the SEM pictures of Gen3\_7 to Gen3\_10, an obvious difference between the qualities of the particle coatings cannot be observed. For more detail information, these materials were additionally characterized by CCC measurements.

**Table 48: Electrode weights of the following CCC measurements and calculated capacities of Gen3 materials fabricated with constant pump speed and varied pressure of spray flow**

Used Gen3 material	Electrode weight [ $\text{mg}\cdot\text{cm}^{-2}$ ]	Capacity [ $\text{mAh}\cdot\text{g}_{\text{AM}}^{-1}$ ]
Gen3_7	0.973	714
Gen3_8	0.964	714
Gen3_9	0.879	699
Gen3_10	0.904	699



**Figure 74: Lithiation capacities received in CCC measurements of electrodes containing Gen3 materials fabricated with constant pump speed and varied pressure of spray flow (CCC1)**

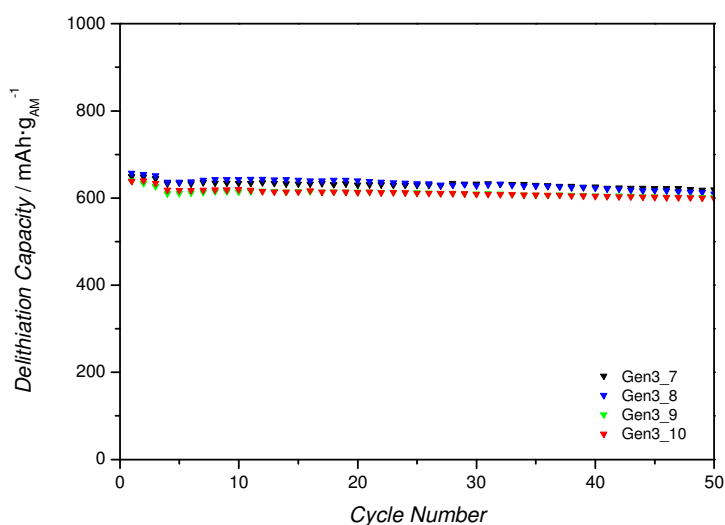


**Figure 75: Delithiation capacities received in CCC measurements of electrodes containing Gen3 materials fabricated with constant pump speed and varied pressure of spray flow (CCC1)**

Comparing the CCC measurement results of the four electrodes, there is no significant difference observable between the materials. The easier handling of the process at higher spray flow was the main reason for using a spray flow of 1.3 bar for further parameter tests.

#### 4.9.3.2 Optimization of the coating process:

##### Varied pump speed and constant pressure of spray flow

The SEM pictures of the Gen3 materials fabricated with varied pump speed (Gen3\_11 to Gen3\_14) clearly display the limitation of the pump speed below 20 rpm (Gen3\_14 material). At this pump speed a uniform particle coating can no longer be achieved, this result is additionally confirmed by a broad PSD of Gen3\_14 material.

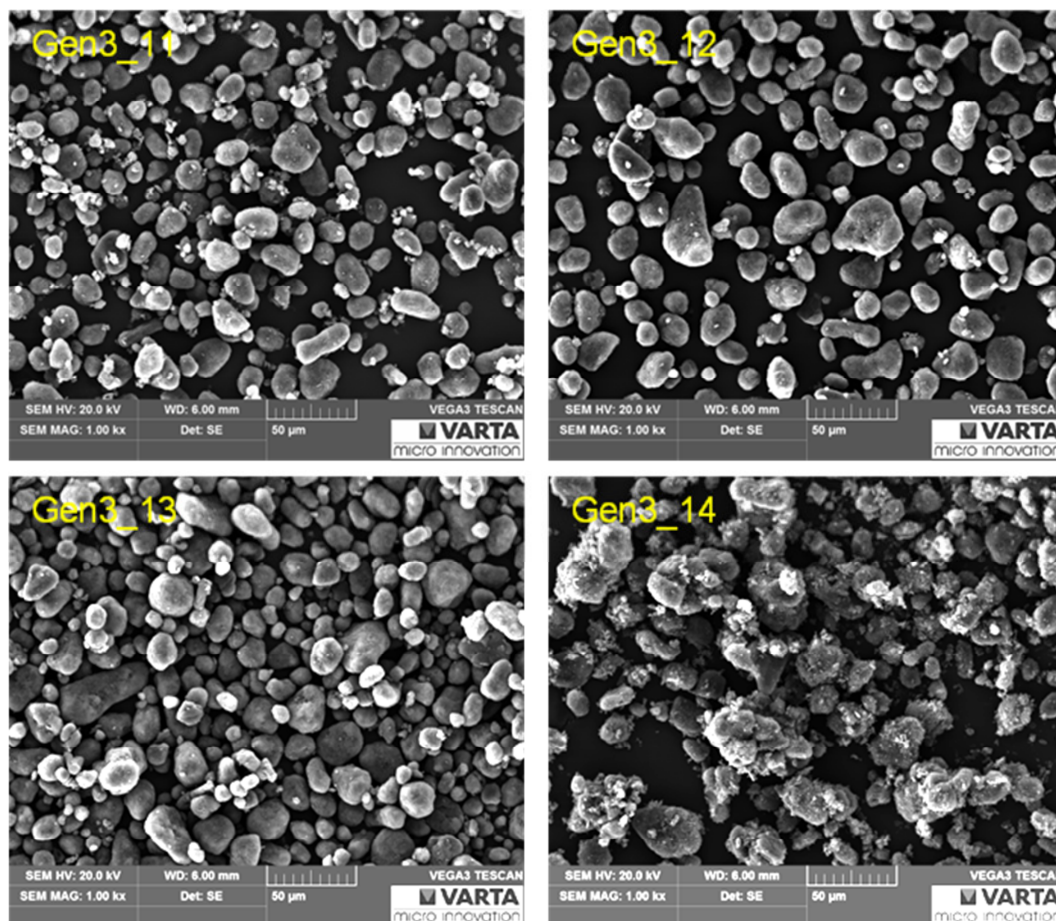


Figure 76: SEM pictures of Gen3 materials fabricated with varied pump speed and constant pressure of spray flow

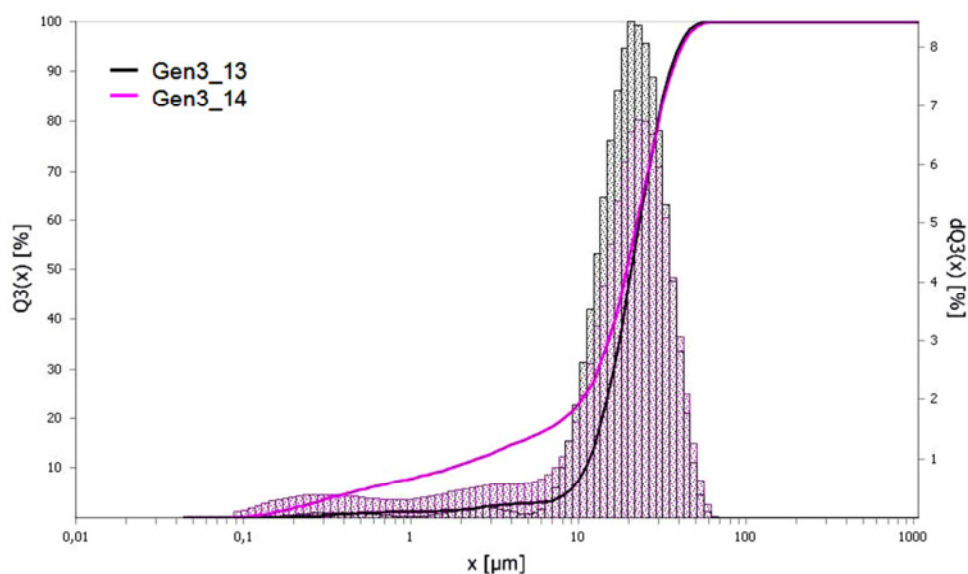


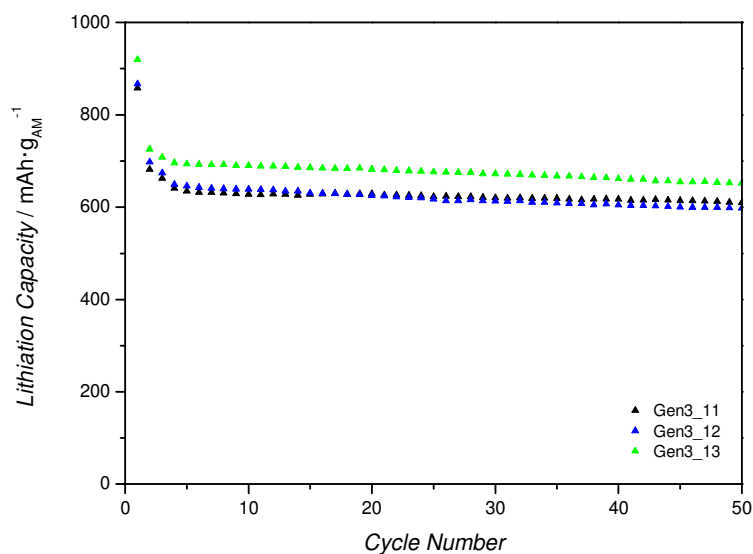
Figure 77: PSDs of Gen3\_13 and Gen3\_14 material

Due to the worse quality of the particle coating process, the Gen3\_14 powder contains a large amount of small agglomerates. These small agglomerates lead to a broader PSD of the Gen3\_14 material compared to the Gen3\_13 material.

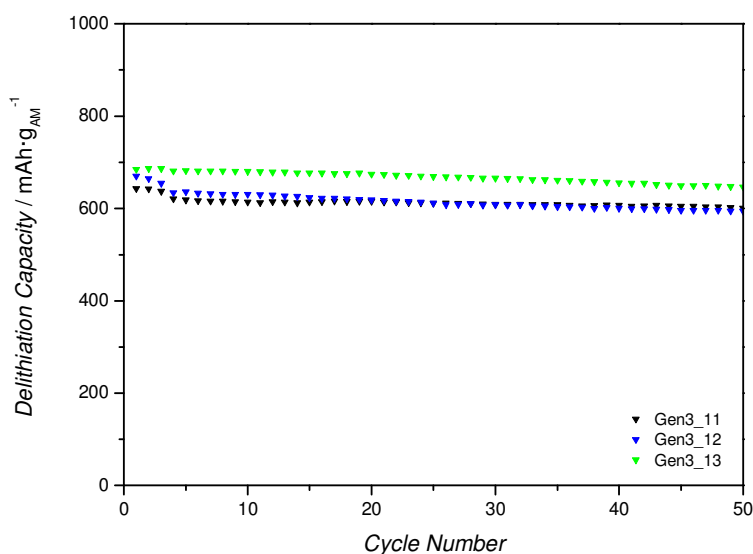
The effect of the increasing pump speed in the Gen3 coating process is evaluated by the CCC measurement results of Gen3\_11, Gen3\_12 and Gen3\_13 materials.

Table 49: Electrode weights of the following CCC measurements and calculated capacities of Gen3 materials fabricated with varied pump speed and constant pressure of spray flow

Used Gen3 material	Electrode weight [mg·cm <sup>-2</sup> ]	Capacity [mAh·g <sub>AM</sub> <sup>-1</sup> ]
Gen3_11	0.893	707
Gen3_12	0.856	714
Gen3_13	0.771	707



**Figure 78: Lithiation capacities received in CCC measurements of electrodes containing Gen3 materials fabricated with varied pump speed and constant pressure of spray flow (CCC1)**



**Figure 79: Delithiation capacities received in CCC measurements of electrodes containing Gen3 materials fabricated with varied pump speed and constant pressure of spray flow (CCC1)**

The obviously higher capacities of the Gen3\_13 material has to be interpreted carefully due to the lower electrode weight of Gen3\_13 electrode. Nevertheless, a higher spray flow is advisable in regard to the smooth functioning of the process.

#### 4.9.4 Structural characterisation of a Gen3 particle with focused ion beam technique

With the help of focused ion beam technique it was possible to illustrate the achieved core-shell particle structure of the Gen3 materials. The results of this characterisation are represented in Figure 80.

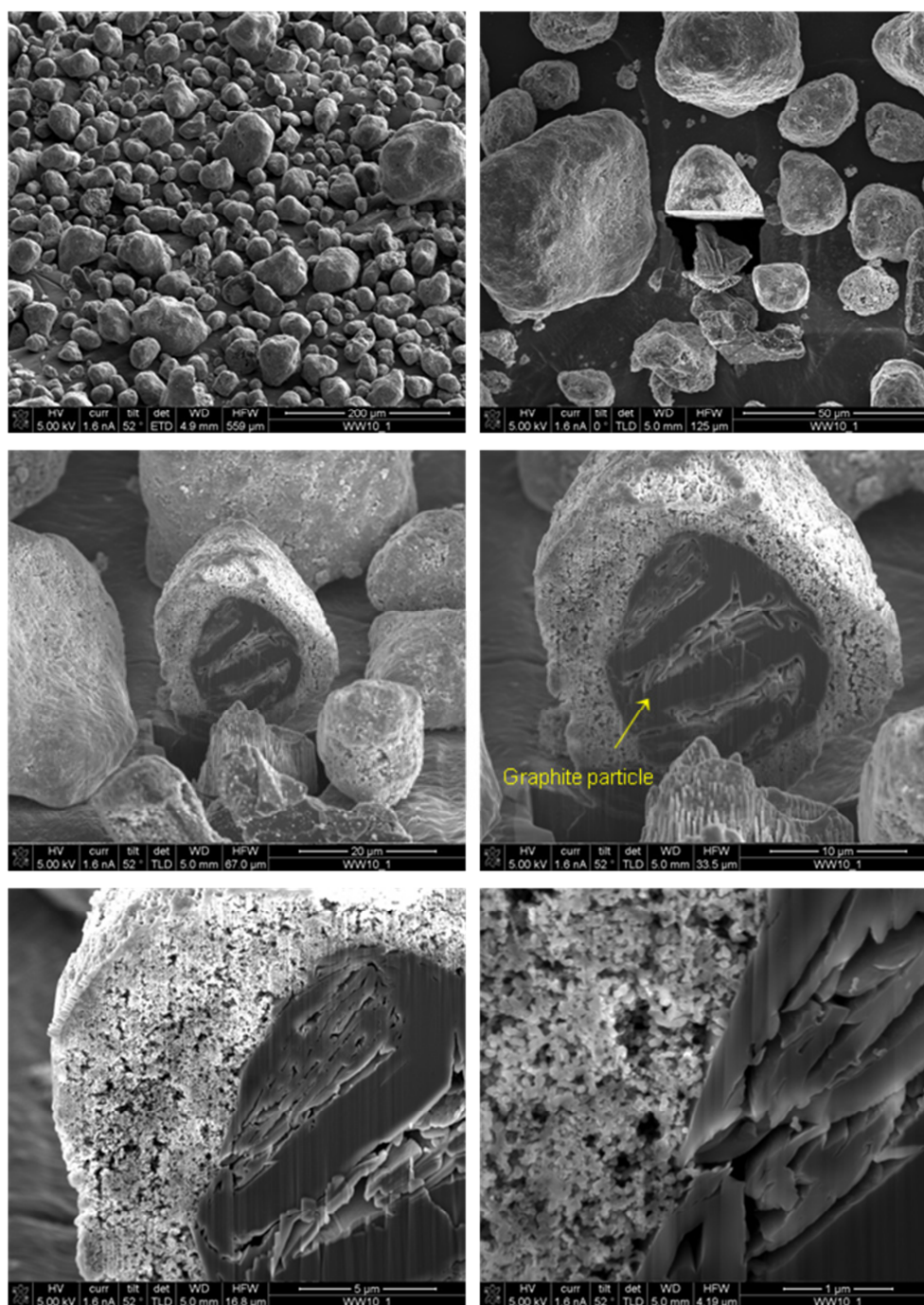


Figure 80: SEM pictures of FIB sliced Gen3 particle

The core-shell structure of Gen3 materials, with the graphite particle in the centre covered by shell components, is clearly demonstrated by the SEM pictures represented in Figure 80. As already mentioned, the shell, consisting of a mixture of silicon, initial carbon black and carbonaceous matrix, has a highly porous structure. The magnification of the shell area (Figure 81) displays the presence of small spherical particles. A main part of these spherical particles probably consists of carbon coated silicon particles, as it is reported in literature as well. [114] [115].

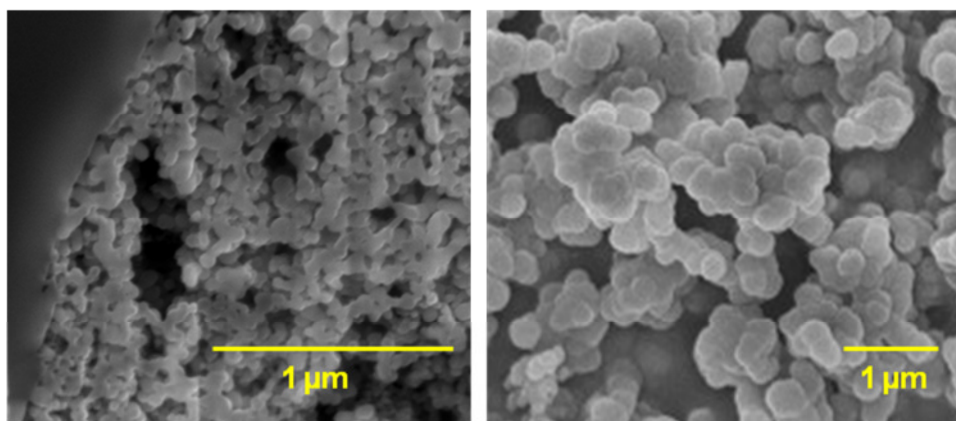


Figure 81: (left) SEM picture of Gen3 shell particles and (right) FE-SEM picture of carbon coated silicon powder represented in reference [114]

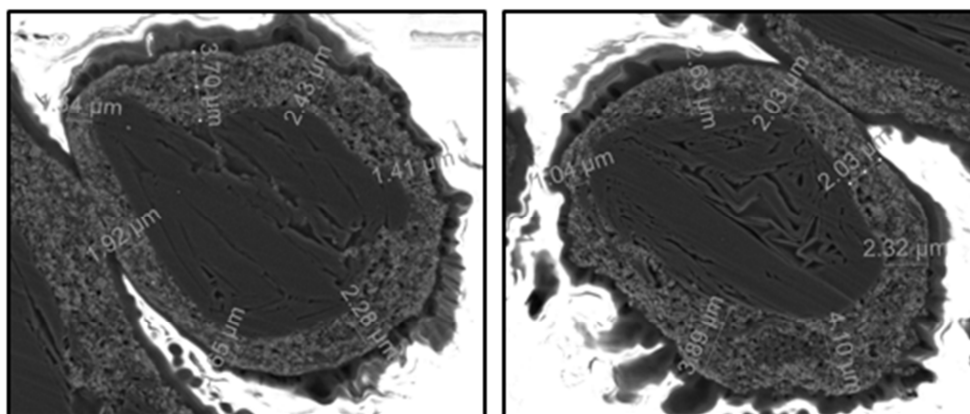


Figure 82: Shell thickness determination of Gen3 coated particles (sample preparation with Gatan Illion<sup>TM</sup> Model693)

By taking in consideration that the shell thickness of each Gen3 material mainly depends on the ratio of graphite to shell particles, the average shell thickness of a Gen3 powder, consisting of approximately 65 wt% graphite to 35 wt% shell compounds, was determined in the range of 2 to 4 μm according to figure 82.

## 4.10 Comparison of the different generations of materials

As in figure 83 demonstrated, the development of a uniform compact core-shell particle structure from Gen1 to Gen3 was successful.

The initially fabricated Gen1 materials consisted more than less of an unstructured mixture of graphite, silicon and carbon black particles embedded in amorphous carbon (Figure 84). However, a huge amount of agglomerates in all sizes was unavoidable by using this method.

The further developed Gen2 materials showed a higher structuring and additionally the formation of bigger agglomerates was prevented by using the Gen2 fabrication process. But the desired uniform core-shell particle was not yet fulfilled by Gen2 materials. Thus the Gen2 materials consisted of a mixture of small pure silicon/amorphous carbon agglomerates as well as high and poor quality coated graphite particles.

Finally, the process of development could be completed with uniformly coated particles in case of the Gen3 material.

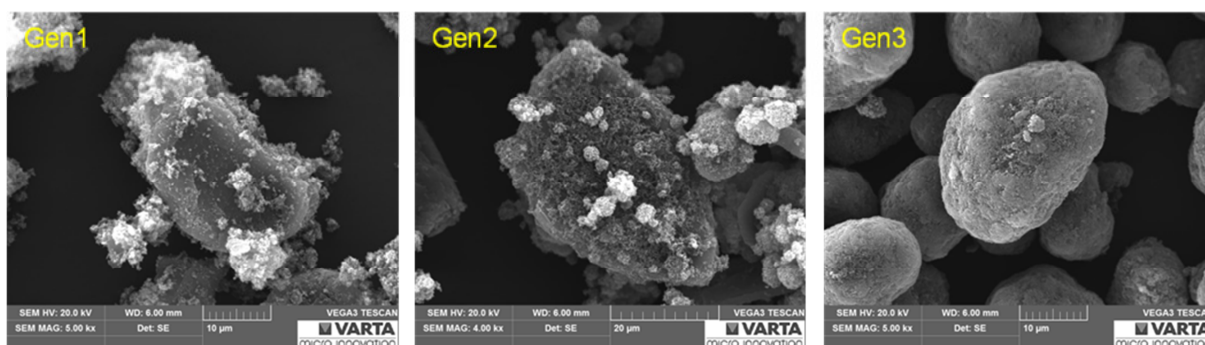


Figure 83: SEM pictures of particles of each generation

As mentioned before, a small number of big and compact agglomerates (Figure 84) were found in Gen1 materials, consisting of graphite, silicon and carbonaceous matrix mixture. Moreover a crushing of these agglomerates by the agate mortar during the crushing step after pyrolysis and respectively, during the 12 hour electrode slurry preparation was not successful. With the use of Gen2 and Gen3 material fabrication techniques the formation of such big and very compact agglomerates could be avoided.

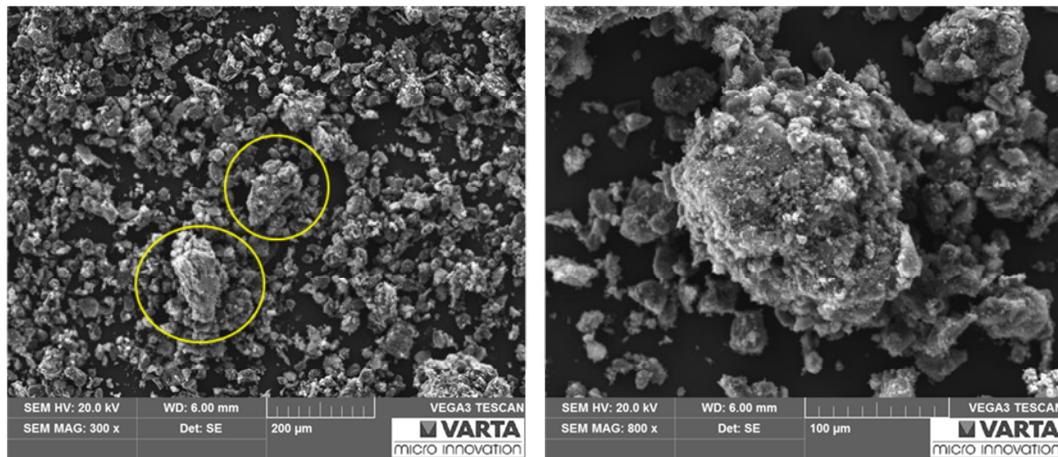


Figure 84: SEM pictures of big compact agglomerates, contained in Gen1 materials

Figure 85 displays PSDs of the different generation materials and pure graphite. It is clearly apparent that the PSDs become more homogenous from Gen1 to Gen3.

The high amount of small (pure silicon/amorphous carbon) and low number of very large compacted agglomerates (silicon/amorphous carbon/graphite) in the Gen1 materials causes a very broad PSD. The reduced amount of small agglomerates as well as the prevention of big agglomerates leads to a narrower PSD in case of the Gen2 material. Both, the graphite and the Gen3 material show similar narrow PSDs, this indicates highly homogenous particles within the Gen3 material. Additionally, the shift to larger particle sizes of Gen3 material compared to graphite demonstrates the increase of particle sizes due to the silicon/amorphous carbon coating of the graphite core particles.

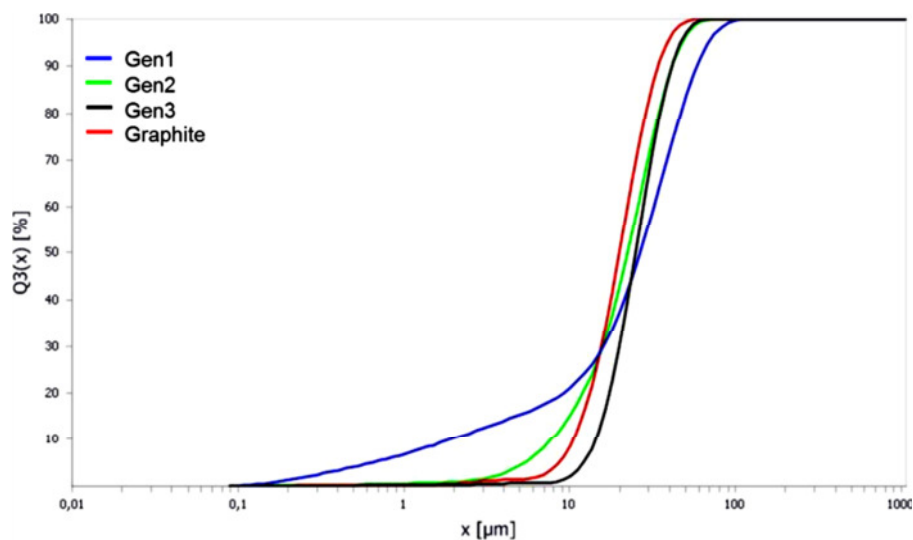


Figure 85: Particle size distributions of Gen1, Gen2, Gen3 materials and graphite

The CCC measurements of Gen1, Gen2 and Gen3 material with equal composition and of a standardized fabricated nano-sized silicon-graphite composite electrode are used for the following electrochemical comparison. Furthermore, the standard silicon-graphite composite electrode was made by slurry technique and the electrode composition is described in table 50.

**Table 50: Composition of standard silicon-graphite composite electrode**

Reagent		Composition [wt%]
Binder :	Na-CMC	8
Conductivity additive:	Carbon black	10
Active material:	nano-sized Silicon	20
	Graphite	62
<b>H<sub>2</sub>O as solvent</b>		

**Table 51: Electrode weights of the following CCC measurements and calculated capacities of materials of different generations and of a standard silicon-graphite composite material (SiC)**

Name	Electrode weight [mg·cm <sup>-2</sup> ]	Capacity [mAh·g <sub>AM</sub> <sup>-1</sup> ]
Gen1	0.955	1012
Gen2	0.796	946
Gen3	0.856	1012
SiC	0.928	1071

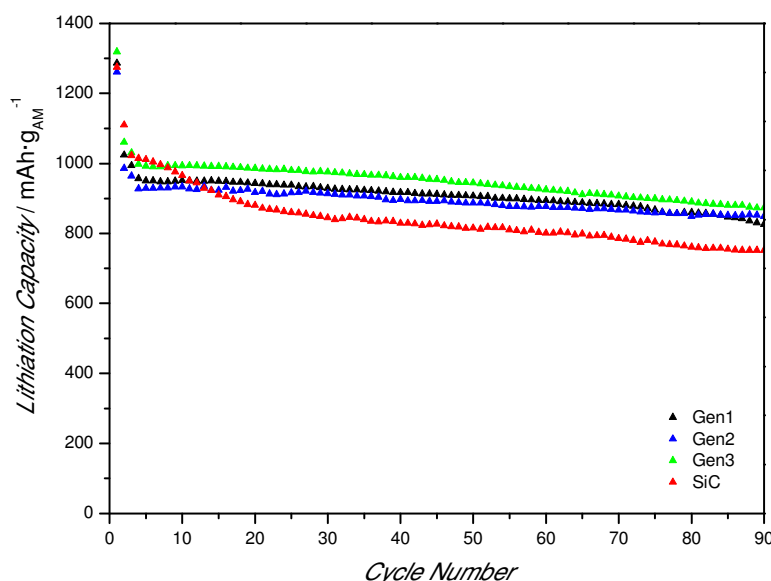


**Figure 86: Lithiation capacities received in CCC measurements of electrodes containing Gen1, Gen2 and Gen3 materials and of a standard SiC electrode (CCC1)**

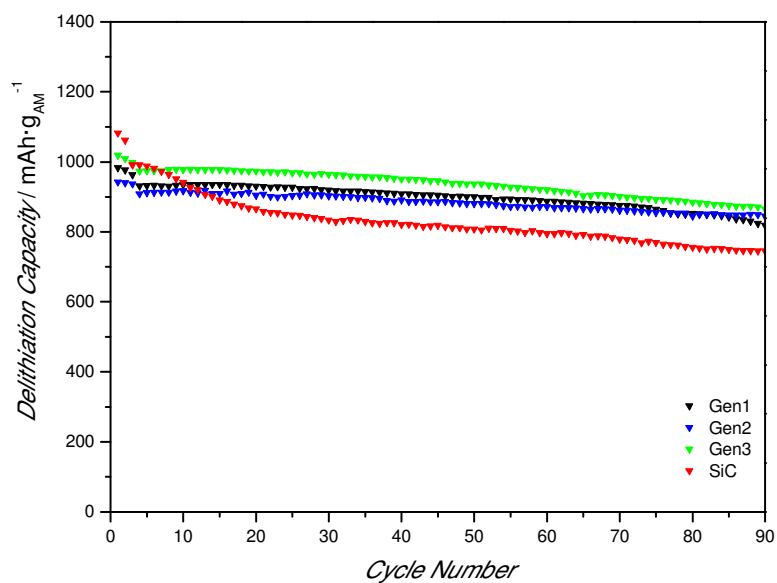


Figure 87: Delithiation capacities received in CCC measurements of electrodes containing Gen1, Gen2 and Gen3 materials and of a standard SiC electrode (CCC1)

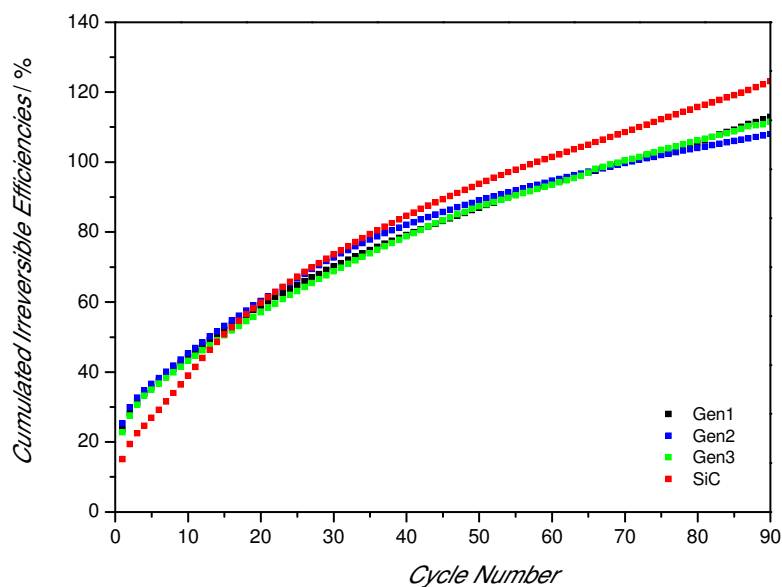


Figure 88: Cumulated irreversible efficiencies received in CCC measurements of electrodes containing Gen1, Gen2 and Gen3 materials and of a standard SiC electrode (CCC1)

Comparing the CCC measurement results of all four electrodes, the SiC electrode has obviously higher capacity fading (Figure 86) and furthermore a faster increase of cumulated irreversible efficiencies than the electrodes of Gen1, 2 and 3 materials (Figure 88).

As known from literature, the main reasons for capacity fading in case of anode materials like graphite and silicon are particle conductivity losses and lithium trapping within the solid (not all of the inserted lithium-ions can be extracted again due to thermodynamical and kinetic reasons) during the cycling. Furthermore, the irreversible capacity is the sum of the irreversible capacity losses caused by electrolyte decomposing (SEI formation within the first cycle and reformation during the cycling caused by fresh surface area), lithium trapping within the solid, active mass losses (particle conductivity losses) and, if present, the reduction of oxide impurities. [116] [117]

The higher capacity fading of the standard SiC electrode indicates elevated particle conductivity losses as well as lithium trapping during the cycling mainly caused by the high volume changes of the contained silicon particles.

By the embedding of the silicon particles into a carbonaceous matrix, the particle conductivity losses are reduced in case of the Gen(1-3) materials, resulting in a lower capacity fading compared to the standard SiC composite electrode.

The reason for abruptly rising capacity fading of Gen1 electrode after 70 cycles may be caused by the high amount of poorly embedded bare or small silicon particles/agglomerates. Due to the poor embedding the conductivity loss is intensified for these agglomerates.

Both, Gen2 and Gen3 electrodes achieve capacities close to their calculated theoretical capacities at the beginning of cycling. Moreover, it can be observed that the capacity fading at the beginning of cycling is higher for the Gen2 electrode than for the Gen3 electrode. This changed during the cycling, leading to a stronger flattening of the Gen2 capacities curves compared to Gen3 capacities curves.

Comparing the cumulated irreversible efficiencies of all electrodes, only the Gen2 electrode displays a decrease in cumulated irreversible efficiencies at the end of cycling, this indicates an improvement of the efficiency during the cycling. It has to be considered that the lowest electrode weight of the Gen2 electrode has a positive influence on the electrode performance and can be a reason for the better electrode performance at the end of cycling compared to the other electrodes.

The lower efficiencies of the Gen(1-3) electrodes in the first cycles compared to the standard SiC electrode may indicate the presence of oxide impurities. However, this assumption

wasn't clarified in the context of this thesis and needs to be analysed in further investigations. [117] [118]

#### 4.10.1 Rate capability tests of Gen(1-3) materials

To receive an overview about the electrochemical behaviour at increasing current densities, rate capability tests at different C-rates were carried out. The used test procedure of the rate capability tests is described in table 52.

**Table 52: Used program of rate capability tests**

Test procedure	Cycle number	C-rate
Step 1	4	0.1
Step 2	4	0.5
Step 3	4	1
Step 4	4	10
Step 5	6	0.1
<b>Charge/discharge limited by 0.005 to 1.5V (+Rest step of 12h)</b>		

**Table 53: Electrode weights of rate capability test and calculated capacities of materials of Gen(1-3)**

Name	Electrode weight [ $\text{mg}\cdot\text{cm}^{-2}$ ]	Capacity [ $\text{mAh}\cdot\text{g}_{\text{AM}}^{-1}$ ]
Gen1	0.937	979
Gen2	0.698	1045
Gen3	0.870	1012

In general, the C-rate specifies the charge and discharge current of the battery. [119] More precisely, the C-rate of 1 defines the charge/discharge current, which leads to a fully charge/discharge of a battery within one hour. Therefore, a C-rate of 0.5 needs two hours and a C-rate of 10 needs six minutes to fully charge/discharge the cell. An overview in respect to the effect of high current densities and strategies to improve the electrochemical performance at high discharge/charge rates is reported in reference [120].

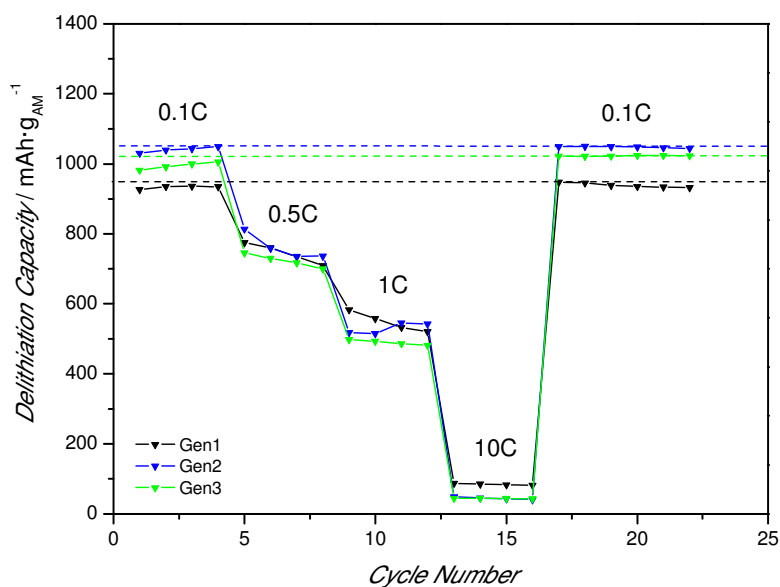


**Figure 89: Delithiation capacities received in rate capability tests of electrodes containing Gen1, Gen2 and Gen3 materials**

For the interpretation of such rate capability tests the achieved capacities at beginning and end of the test (received at equal C-Rate of 0.1) are used to display the influences of the different current densities on the electrode. Equal capacities at the beginning and the end are desirable, because this indicates a high resistance against increasing current densities.

Figure 89 represents the delithiation capacities of Gen1, Gen2 and Gen3 electrodes, achieved in their rate capability tests. All three electrodes were able to reach again the capacity values of the initial cycles after the high current treatment. In case of the Gen1 electrode a slight capacity fading in the last 6 cycles is evident. Due to the fact that this capacity fading can be only observed for Gen1 electrode, a better structural stabilisation with a better resistance against high current densities can be assumed for the Gen2 and Gen3 materials than for Gen1 material.

## 4.11 Characterisation of a Gen2 material with transmission electron microscopy

In order to receive more detailed information on the structure of the fabricated Gen2 materials, TEM and EF-TEM measurements were carried out. More precisely, a possible undesired aggregation of the silicon particles, caused by sintering during pyrolysis, should be excluded or identified by the results of the TEM characterisation.

Table 54: Used equipments for TEM characterisation

TEM (Philips CM 20)	
TEM sample preparation	Microtome (Leica Ultra UCT)
Energy filtered images	“Gatan 678 Imaging Filter” with a lateral resolution down to about 1 nm

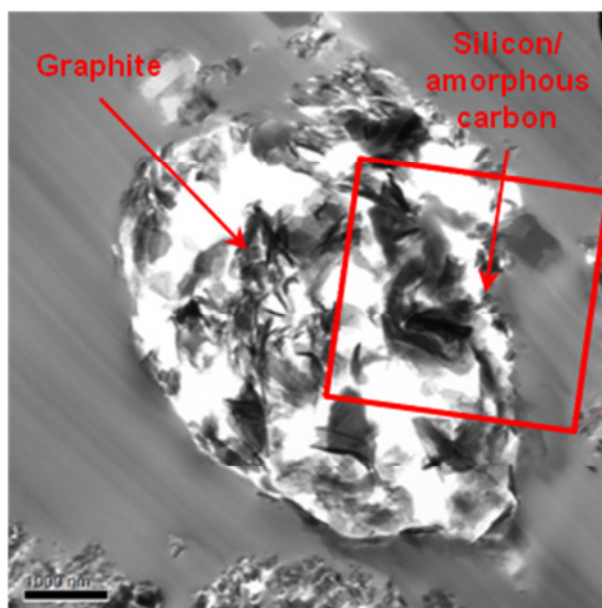
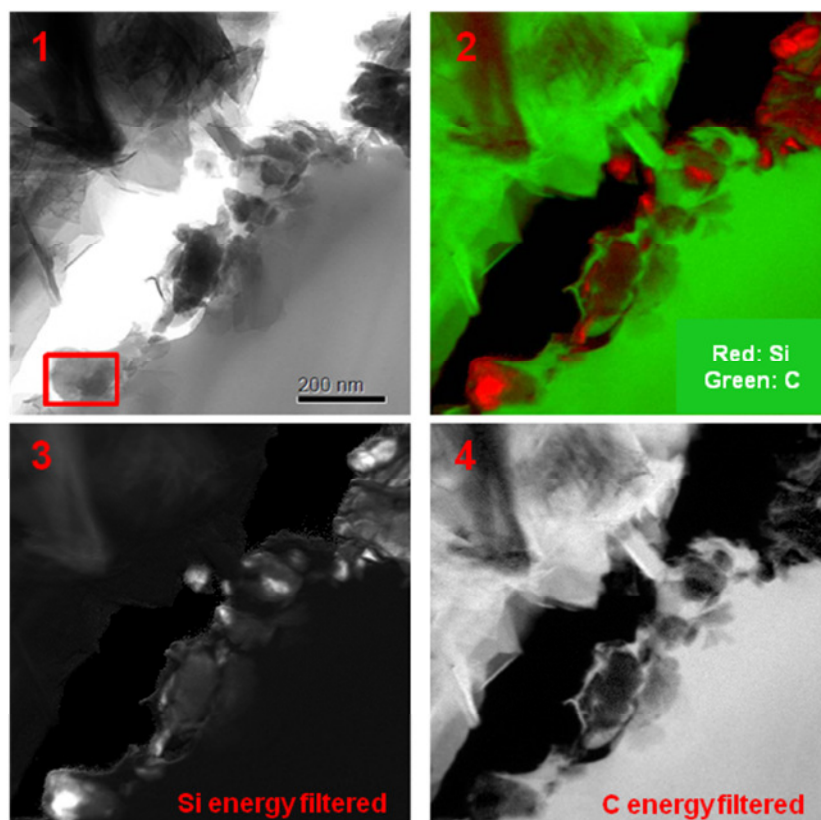


Figure 90: TEM picture of a Gen2 particle



**Figure 91: TEM and EF-TEM images (elemental maps) of the red framed area from figure 90, (1) TEM image; (2) coloured mixed EF-TEM image of silicon (Si) (red) and carbon (C) (green); (3) Si EF-TEM image; (4) C EF-TEM image**

Figure 90 illustrates a TEM image of a thin-section of a Gen2 particle. The red framed area in figure 90 was examined more closely, since shell particles were suspected in this area. This was confirmed by the recorded EF-TEM pictures of the magnified red framed area of figure 90, illustrated in figure 91.

According to the TEM and EF-TEM results, an aggregation of the silicon particles was not determined (indicated by the total carbon framing of each silicon particle). To support this result, a small pure silicon/amorphous carbon agglomerate of one Gen2 material was additionally analysed with TEM and EF-TEM (Figure 92 and figure 93). The higher amount of silicon particles in this small agglomerate enabled a more accurate interpretation of the sintering issue.

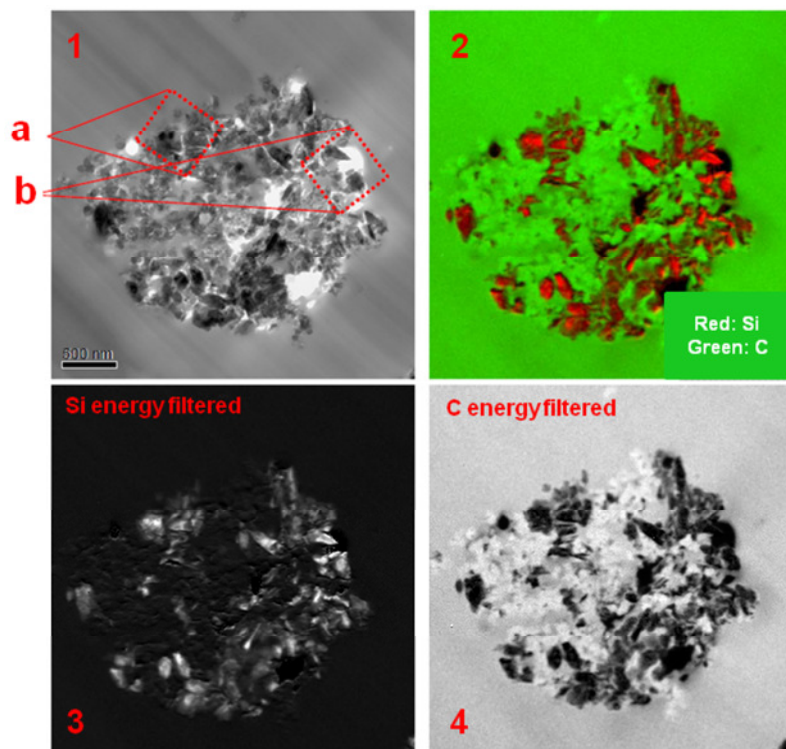


Figure 92: TEM image of silicon/amorphous carbon agglomerate (picture 1), EF-TEM of Si (picture 3); EF-TEM of C (picture 4) and coloured mixed EF-TEM image of Si (red) and C (green) (picture 2)

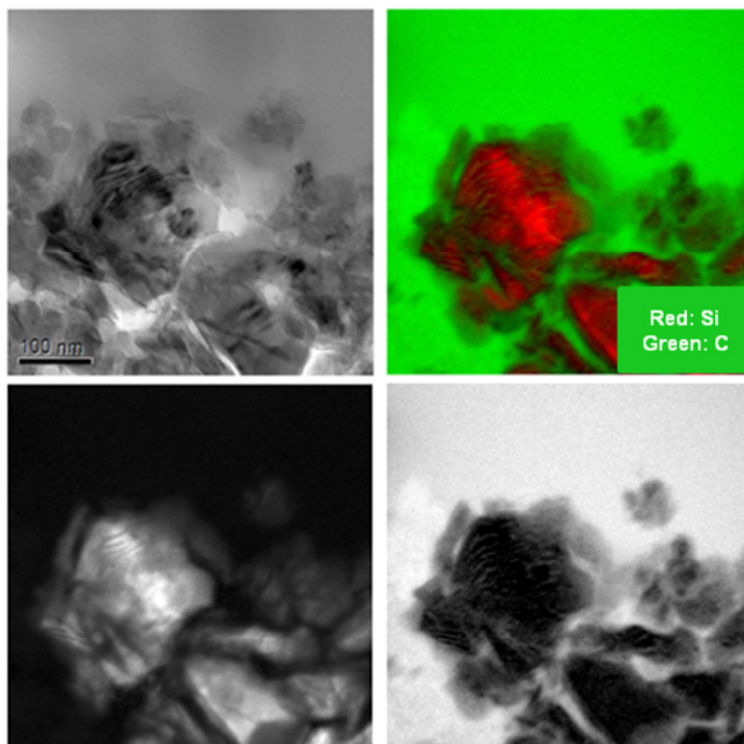
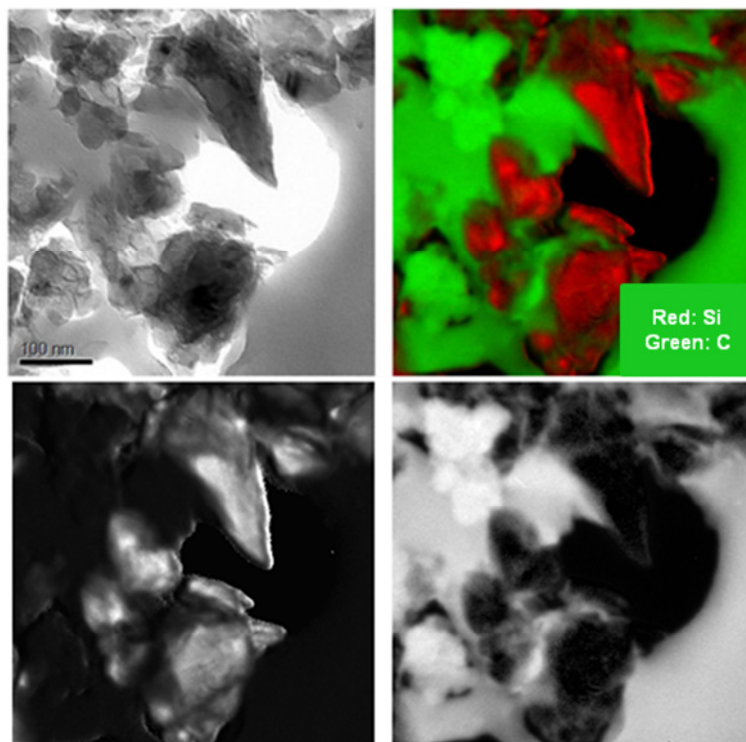


Figure 93: TEM and EF-TEM images of magnified red framed areas (a) of figure 92 with the same arrangement of images like figure 92



**Figure 94: TEM and EF-TEM images of magnified red framed area (b) of figure 92 with the same arrangement of images like figure 92**

Especially in the red framed area (b) of figure 92 (magnified in figure 94), a prevention of the sintering among the silicon particles is clearly visible, due to the sharp-ending edges of the silicon particles and the total covering/framing with carbon of each silicon particle.

## 5 Conclusion

Within this doctoral thesis, the development of a silicon-graphite composite material with core-shell structured particles was successfully realised. The composite particles consist of a graphite particle core covered with a shell of silicon particles embedded in a carbonaceous matrix. The embedding of the silicon has the major benefit that the huge volume changes of the silicon particles during the lithiation and delithiation processes can be compensated by the carbonaceous matrix, leading to higher structure stability of the fabricated composite material compared to standard silicon-graphite composite material.

The Gen1 of composite materials, fabricated with a simple mixing process, consists of low structured particles in all sizes. For the further developed Gen2 materials a spray drying process is used for synthesis, leading to more homogenous materials and simultaneously preventing huge compact agglomerates, which can be found in the Gen1 materials. Finally, a successful fabrication of highly core-shell structured particles with homogenous particle size distribution is realized in form of Gen3 materials. These materials are fabricated with the help of a fluidized bed reactor with wurster-configuration.

Additionally, the fabrication process of the Gen3 materials provides the possibility of an individual particle design with a precise capacity adjusting for each material, controlled by the amount, size, nature and form of the used components as well as process parameters such as retention time, temperature, fluid flow etc.

Considering the harmful properties of nano-sized particles, the embedding of the nano-sized silicon particles within the particle shell of the Gen3 material is a great advantage and displays a high potential for commercial application. Especially as the embedding of the silicon particles can be implemented without the loss of the beneficial properties of nano-sized particles. Moreover, the sophisticated preparation of standard nano-sized silicon-graphite composite electrodes, mainly caused by the difficult handling of the nano-sized particles, can be simplified by the use of the Gen3 composite material, due to the prevention of nano-sized particles in the electrode preparation process.

Furthermore, a reduction of the content of conductivity additives within the electrode preparation is possible, since the carbonaceous matrix is already electrically conductive in case of Gen3 particles. The reduction of the conductivity additive content in the electrode is directly related with a decrease of inactive mass in the electrode, this in turn leads to an increase of the capacity.

The use of a lab-sized fluidized bed reactor for the Gen3 material fabrication has limited application possibilities. Thereby, the up-scaling in commercial used fluidized bed reactor will offer many opportunities for further improvements. Considerable optimization potential regarding to the process can also be found by varying the nature, size and form of the different components (graphite, silicon, polymer precursor). Moreover, adding of varied conductivity additives as well as direct carbon coating of the manufactured core-shell particles may lead to an improved electrochemical performance of these materials due to the increased electrical conductivity.

Summing up, the Gen3 materials display great potential for a commercial application regarding to the easier handling, the precise adjusting of the particle design/capacity and the improved structural stabilisation caused by the embedded silicon particles within the carbonaceous matrix.

## 6 Appendix

### 6.1 List of chemicals

#### ***Materials:***

Graphite...	Nanshu graphite - high purity graphite
Nano-sized Silicon...	Silicon Nanopowder 30-50 nm APS

#### ***Components of the epoxy resin precursor:***

Epoxy resin...	Araldite®506 epoxy resin
Hardener...	3-Dimethylamino-propylamin
Solvent...	1-Methoxy-2-propanol

#### ***Other polymer precursors:***

PVdF...	Kynar 761
Tar...	OMV-sample

#### ***Conductivity additives:***

Carbon black...	Super P™ Li
CNT/carbon black mixture...	multi-walled carbon nanotubes (CNT) + carbon black

#### ***Components of the used electrolyte:***

Additive...	VC
Salt...	LiPF <sub>6</sub>
Solvents...	EC, DEC, EMC

## 6.2 List of devices

BET measurements...	ASAP 2000 Model Nr: 200/00000/10
CCC measurements...	Maccor Series 4000
CV measurements...	Bio-logic VMP3
FIB measurements...	FIB/SEM Dual Beam Microscope FEI NOVA200
Fluidized bed reactor...	Mini Glatt with Microkit (Project nr.11147)
PSD measurements...	Analysette 22 NanoTec plus
SEM...	Analytic Scanning Electron Microscope VEGA 3 SEM
Tube Furnace...	RHTC 80-230/15 with Controller B180
TEM...	Philips CM 20

## 6.3 List of abbreviations

AM...	Electrochemically <b>active material</b> used for electrode preparation (Silicon and graphite)
CCC...	<b>Constant current charging</b>
CCC1...	CCC program used for CCC measurements (Table 8)
CM...	<b>Carbonaceous matrix</b> formed by pyrolysed EP
CNP...	<b>Components that are not pyrolysed</b> (silicon, graphite, carbon black)
CNT...	<b>Carbon nanotubes</b>
CV...	<b>Cyclic voltammetry</b>
CV1...	CV program used for CV measurements (Table 7)
DAPA...	<b>3-Dimethylamino-propylamin</b>
DEC...	<b>Diethyl carbonate</b>
EC...	<b>Ethylene carbonate</b>
EF-TEM...	<b>Energy-filtered transmission electron microscopy</b>
EMC...	<b>Ethyl methyl carbonate</b>
EP...	Initial <b>epoxy resin precursor</b> (non pyrolysed)

---

FIB...	<b>F</b> ocused ion <b>b</b> eam
Gen(1-3)...	<b>G</b> eneration <b>1-3</b> materials
Li <sup>+</sup> ...	<b>L</b> ithium- <b>i</b> on
LIB...	<b>L</b> ithium- <b>i</b> on <b>b</b> attery
Li-GIC...	<b>L</b> ithium <b>g</b> raphite intercalation <b>c</b> ompound
LiPF <sub>6</sub> ...	<b>L</b> ithium hexa <b>f</b> luoro <b>p</b> hosphate
Na-CMC...	Sodium- <b>c</b> arboxy <b>m</b> ethyl <b>c</b> ellulose
OCV...	<b>O</b> pen circuit <b>v</b> oltage
PSD...	<b>P</b> article <b>s</b> ize <b>d</b> istribution
PVDF...	<b>P</b> oly <b>v</b> inylidene <b>d</b> ifluoride
SEM...	<b>S</b> canning <b>e</b> lectron <b>m</b> icroscopy
SiC...	Nano-sized silicon-graphite composite material
TEM...	<b>T</b> ransmission <b>e</b> lectron <b>m</b> icroscopy
VC...	<b>V</b> inylene <b>c</b> arbonate

## 6.4 List of figures

Figure 1: Rechargeable battery market worldwide (redrawn from [1]) .....	1
Figure 2: The total cell capacity (18650 Li-ion cell) as a function of the anode capacity including masses of other required internal components and case [2] .....	2
Figure 3: Schematic illustration of galvanic cell (Daniell element) (redrawn from [7]) .....	4
Figure 4: Electrochemical series of metals (redrawn from [8]) .....	6
Figure 5: Tafel plot (redrawn from [12]) .....	12
Figure 6: Cell polarization as function of operating current (redrawn from [4] [14]) .....	14
Figure 7: Illustration of Ragone plots of various battery systems [17] .....	17
Figure 9: Cylindrical [26] (left), prismatic (middle) [27] and pouch (right) [27] format of lithium-ion batteries .....	20
Figure 10: Potentials and theoretical capacities of negative and positive active materials for LIBs [29] .....	21
Figure 11: Possible mechanisms for lithium deposition and dissolution (redrawn from [5]) .....	22
Figure 12: Schematic illustration of (a) hard (non-graphitizable) and (b) soft (graphitizable) carbons (redrawn from [35] [36]) .....	24
Figure 13: Schematic illustration of the crystal structure of hexagonal graphite showing AB layer stacking sequence and the corresponding unit cell [30] .....	24
Figure 14: (a) Stage formation and structure of lithium-graphite intercalation compounds [33] [37] and (b) cyclic voltammogram of lithium intercalation into highly crystalline graphite [38] .....	25
Figure 15: (left) gravimetric and volumetric capacity of various full lithiated negative active materials (volume expansion but no lithium weight is included) and (right) volumetric expansion rates of these full lithiated materials [40] .....	26
Figure 16: Coulometric titration curve for the lithium-silicon system at temperature of 415 °C (redrawn from [46]) .....	27
Figure 17: Schematic illustration of 1-, 2- and 3-dimensional Li-host materials [33] .....	30
Figure 18: 2D layered structure of $\text{LiMO}_2$ ( $\alpha$ - $\text{NaFeO}_2$ -type) [72] .....	31
Figure 19: (left) Schematical illustration of $\text{LiMn}_2\text{O}_4$ structure [71] and (right) cyclic voltammogram of $\text{LiMn}_2\text{O}_4$ [33] .....	32
Figure 20: Schematical illustration of the $\text{LiFePO}_4$ structure (1D mobility of $\text{Li}^+$ ) [78] .....	33
Figure 21: (left) Schematic illustration of oxidative and reductive reactions taking place on Au electrode in Li-salt/alkyl carbonate solution ( $\text{LiClO}_4/\text{PC}$ ) depending on the applied potential [87] and (right) electrochemical stability window of some solvents (measured on M20 porous carbon electrode with 1 mol/l $\text{Et}_4\text{NPF}_6$ as salt) [82] .....	37
Figure 22: Schematical illustration of an graphene interlayer without $\text{Li}^+$ intercalate, with a solvated $\text{Li}^+$ intercalate (solvated (ternary) graphite intercalation compound GIC) and desolvated $\text{Li}^+$ intercalates (graphite intercalation compound GIC) [88] (interlayer distance data of ternary GIC formed in PC-electrolyte [89]) .....	38

Figure 23: Schematical illustration of changes at carbonaceous electrode/electrolyte interface [93] .....	40
Figure 24: Causes and effects of the ageing mechanisms in case of cathode materials (redrawn from [95]) .....	41
Figure 25: Schematical illustration of cathode ageing mechanisms (redrawn from [93]).....	41
Figure 27: Schematical illustration of a measurement cell type Swagelok® .....	44
Figure 28: Fluidized bed reactor (Mini Glatt) wurster-configuration .....	46
Figure 29: Particle coating principle [102] .....	47
Figure 30: Schematic diagram of particle design .....	49
Figure 31: Comparison of 3rd cycle of CV experiments of electrodes with different polymer precursors (CV1) .....	52
Figure 32: Lithiation capacities received in CCC measurements of electrodes containing different Gen1 materials (CCC1) .....	56
Figure 33: Delithiation capacities received in CCC measurements of electrodes containing different Gen1 materials (CCC1) .....	56
Figure 34: Cumulated irreversible efficiencies received in CCC measurements of electrodes containing different Gen1 materials (CCC1).....	57
Figure 35: Lithiation capacities received in CCC measurements of electrodes containing Gen1 materials fabricated with different pyrolysis temperatures (CCC1) .....	59
Figure 36: Delithiation capacities received in CCC measurements of electrodes containing Gen1 materials fabricated with different pyrolysis temperatures (CCC1) .....	60
Figure 37: Cumulated irreversible efficiencies received in CCC measurements of electrodes containing Gen1 materials fabricated with different pyrolysis temperatures (CCC1) .....	60
Figure 38: Schematic illustration of spray drying process.....	61
Figure 39: SEM picture of a Gen2 powder (some of the small graphite-free silicon/amorphous carbon agglomerates are yellow framed).....	62
Figure 40: Gen2 graphite particle coated with silicon/amorphous carbon .....	63
Figure 41: SEM pictures of an unsliced (left) and a FIB sliced (right) silicon/amorphous carbon agglomerate.....	63
Figure 42: FIB sliced graphite particle .....	64
Figure 43: Particle size distribution of a Gen1, Gen2 powder and pure graphite .....	65
Figure 44: Lithiation capacities received in CCC measurements of electrodes containing Gen2 materials fabricated with different EP content (CCC1).....	67
Figure 45: Delithiation capacities received in CCC measurements of electrodes containing Gen2 materials fabricated with different EP content (CCC1).....	67
Figure 46: Cumulated irreversible efficiency received in CCC measurements of electrodes containing Gen2 materials fabricated with different EP content (CCC1) .....	68
Figure 47: Lithiation capacities received in CCC measurements of electrodes containing Gen2 materials fabricated with varied spray flow and constant pump speed (CCC1).....	70

Figure 48: Delithiation capacities received in CCC measurements of electrodes containing Gen2 materials fabricated with varied spray flow and constant pump speed (CCC1) .....	71
Figure 49: Cumulated irreversible efficiencies received in CCC measurements of electrodes containing Gen2 materials fabricated with varied spray flow and constant pump speed (CCC1) .....	71
Figure 50: Lithiation capacities received in CCC measurements of electrodes containing Gen2 materials fabricated with constant spray flow and varied pump speed (CCC1) .....	72
Figure 51: Delithiation capacities received in CCC measurements of electrodes containing Gen2 materials fabricated with constant spray flow and varied pump speed (CCC1) .....	73
Figure 52: Cumulated irreversible efficiencies received in CCC measurements of electrodes containing Gen2 materials fabricated with constant spray flow and varied pump speed (CCC1) .....	73
Figure 53: Comparison of 3rd cycle of CV experiments of electrodes containing Gen2 materials with varied silicon particle sizes (CV1) .....	75
Figure 54: Delithiation/lithiation capacities and efficiencies received in CCC measurements of electrodes containing Gen2 materials with varied silicon particle sizes (CCC1) .....	76
Figure 55: Comparison of 3rd cycle of CV experiments of electrodes containing Gen2 materials with varied silicon contents (CV1) .....	77
Figure 56: Delithiation/lithiation capacities and efficiencies received in CCC measurements of electrodes containing Gen2 materials with varied silicon contents (CCC1) .....	78
Figure 57: Comparison of 3rd cycle of CV experiments of electrodes containing Gen2 materials with varied carbonaceous matrix compositions (CV1) .....	80
Figure 58: Delithiation/lithiation capacities received in CCC measurements of electrodes containing Gen2 materials with varied carbonaceous matrix compositions (CCC1) .....	81
Figure 59: Cumulated irreversible efficiencies received in CCC measurements of electrodes containing Gen2 materials with varied carbonaceous matrix compositions (CCC1) .....	82
Figure 60: SEM pictures of Gen2_4 powder (a) with 500x (b) with 2000x magnification (c)+(e) with high quality coated graphite particles, (d) small pure silicon/amorphous carbon agglomerate and (f) poor coated graphite particle .....	83
Figure 61: Particle size distributions of a Gen2 material and graphite .....	84
Figure 62: SEM pictures of a Gen3 powder .....	84
Figure 63: SEM pictures of Gen3 powder fabricated with an initial epoxy resin content of 30 wt% .....	86
Figure 64: SEM pictures of different Gen3 materials at 3000x magnification .....	88
Figure 65: Particle size distributions of Gen3 materials with different compositions and graphite .....	89
Figure 66: Huge visible agglomerates contained in Gen3_5 material .....	90
Figure 67: Comparison of 3rd cycle of CV experiments of electrodes containing Gen3 materials with different silicon contents (CV1) .....	90

Figure 68: Lithiation capacities received in CCC measurements of electrodes containing Gen3 materials with different silicon contents (CCC1) .....	92
Figure 69: Delithiation capacities received in CCC measurements of electrodes containing Gen3 materials with different silicon contents (CCC1) .....	92
Figure 70: Cumulated irreversible efficiencies received in CCC measurements of electrodes containing Gen3 materials with different silicon contents (CCC1) .....	93
Figure 71: Comparison of 3rd cycle of CV experiments of electrodes containing Gen3 materials with different shell compositions (CV1).....	95
Figure 72: Delithiation/lithiation capacities and efficiencies received in CCC measurements of electrodes containing Gen3 materials with different shell compositions (CCC1).....	96
Figure 73: SEM pictures of Gen3 materials fabricated with constant pump speed and varied pressure of spray flow.....	98
Figure 74: Lithiation capacities received in CCC measurements of electrodes containing Gen3 materials fabricated with constant pump speed and varied pressure of spray flow (CCC1) .....	99
Figure 75: Delithiation capacities received in CCC measurements of electrodes containing Gen3 materials fabricated with constant pump speed and varied pressure of spray flow (CCC1) .....	99
Figure 77: PSDs of Gen3_13 and Gen3_14 material .....	101
Figure 78: Lithiation capacities received in CCC measurements of electrodes containing Gen3 materials fabricated with varied pump speed and constant pressure of spray flow (CCC1) .....	102
Figure 79: Delithiation capacities received in CCC measurements of electrodes containing Gen3 materials fabricated with varied pump speed and constant pressure of spray flow (CCC1) .....	102
Figure 80: SEM pictures of FIB sliced Gen3 particle .....	103
Figure 81: (left) SEM picture of Gen3 shell particles and (right) FE-SEM picture of carbon coated silicon powder represented in reference [114] .....	104
Figure 82: Shell thickness determination of Gen3 coated particles (sample preparation with Gatan Illion <sup>+</sup> ™ Model693) .....	104
Figure 83: SEM pictures of particles of each generation .....	105
Figure 84: SEM pictures of big compact agglomerates, contained in Gen1 materials .....	106
Figure 85: Particle size distributions of Gen1, Gen2, Gen3 materials and graphite .....	106
Figure 86: Lithiation capacities received in CCC measurements of electrodes containing Gen1, Gen2 and Gen3 materials and of a standard SiC electrode (CCC1) .....	107
Figure 87: Delithiation capacities received in CCC measurements of electrodes containing Gen1, Gen2 and Gen3 materials and of a standard SiC electrode (CCC1) .....	108
Figure 88: Cumulated irreversible efficiencies received in CCC measurements of electrodes containing Gen1, Gen2 and Gen3 materials and of a standard SiC electrode (CCC1).....	108

Figure 89: Delithiation capacities received in rate capability tests of electrodes containing Gen1, Gen2 and Gen3 materials.....	111
Figure 90: TEM picture of a Gen2 particle .....	112
Figure 91: TEM and EF-TEM images (elemental maps) of the red framed area from figure 90, (1) TEM image; (2) coloured mixed EF-TEM image of silicon (Si) (red) and carbon (C) (green); (3) Si EF-TEM image; (4) C EF-TEM image.....	113
Figure 94: TEM and EF-TEM images of magnified red framed areas (a) of figure 93 with the same arrangement of images like figure 93.....	114
Figure 95: TEM and EF-TEM images of magnified red framed area (b) of figure 93 with the same arrangement of images like figure 93.....	115

## 6.5 List of tables

Table 1: Comparison of available LIB cell formats (redrawn from [25]) .....	20
Table 2: Stoichiometry and potential range E (open circuit voltage/electromotive force) of the four Li-Si phases (at 415°C), plotted in Figure 16 [46] .....	27
Table 3: Organic solvent used for LIB electrolytes [81] [82].....	35
Table 4: Conductive salts used in LIB electrolytes [81] [82].....	35
Table 5: Causes, effects and influences of LIB anode ageing (redrawn) [93] .....	40
Table 6: Electrode slurry composition used in this thesis .....	43
Table 7: Program used for CV measurements.....	44
Table 8: Program used for CCC measurements .....	45
Table 13: Corresponding delithiation/lithiation capacities and efficiencies of CV measurements (Figure 31) .....	52
Table 14: Calculated capacities of SiC_Tar, SiC_PVdF and SiC_EP materials.....	52
Table 15: Composition of Gen1 materials .....	53
Table 16: Procedure of Gen1 material fabrication.....	54
Table 17: Pyrolysis parameters of Gen1 materials introduced in table 18.....	54
Table 18: Composition ratios before and after pyrolysis of Gen1 materials with different EP content.....	55
Table 19: Electrode weights of the following CCC measurements and calculated capacities of Gen1 materials fabricated with different EP contents .....	55
Table 20: Powder composition for pyrolysis tests .....	58
Table 21: Composition ratios before and after pyrolysis of Gen1 materials fabricated at different pyrolysis temperatures .....	58
Table 22: Electrode weights of the following CCC measurements and calculated capacities of Gen1 materials fabricated with different pyrolysis temperatures .....	59
Table 23: Procedure of Gen2 material fabrication.....	62

Table 24: Composition ratios before and after pyrolysis of Gen2 materials with different EP contents .....	65
Table 25: Additional composition information for table 24 .....	66
Table 26: Spray drying parameters for Gen2 materials with different EP/CNP ratios .....	66
Table 27: Electrode weights of the following CCC measurements and calculated capacities of Gen2 materials fabricated with different EP contents .....	66
Table 28: Varied parameters of the spray drying process .....	69
Table 29: Electrode weights of the following CCC measurements and calculated capacities of Gen2 materials fabricated with varied spray flow and constant pump speed .....	70
Table 30: Electrode weights of the following CCC measurements and calculated capacities of Gen2 materials fabricated with constant spray flow and varied pump speed .....	72
Table 31: Electrode weights of the following CCC measurements and calculated capacities of Gen2 materials fabricated with varied shell compositions .....	74
Table 32: Spray drying parameters of Gen2_Si130n, Gen2_Si25%, Gen2_0C and Gen2_CNT materials .....	74
Table 33: Composition of Gen2_Si130n material.....	75
Table 34: Corresponding delithiation/lithiation capacities and efficiencies of CV measurements (Figure 53) .....	76
Table 35: Composition of Gen2_Si25% material .....	77
Table 36: Corresponding delithiation/lithiation capacities and efficiencies of CV measurements (Figure 55) .....	78
Table 37: Compositions of Gen2_CNT and Gen2_0C materials .....	79
Table 38: Corresponding delithiation/lithiation capacities and efficiencies of CV measurements (Figure 57) .....	80
Table 39: Procedure of Gen3 materials fabrication.....	85
Table 40: Compositions before pyrolysis of different Gen3 materials.....	86
Table 41: EP/CNP ratios before and CM/CNP ratios after pyrolysis of different Gen3 materials .....	87
Table 42: Calculated capacities of different Gen3 materials.....	87
Table 43: Fluidized bed reactor parameters of Gen3 materials fabricated with different compositions .....	87
Table 44: Corresponding delithiation/lithiation capacities and efficiencies of CV measurements (Figure 67) .....	91
Table 45: Electrode weights of the following CCC measurements of Gen3 materials fabricated with different silicon contents .....	91
Table 46: BET surfaces of different Gen3 materials, graphite and nano-sized silicon .....	94
Table 47: Corresponding delithiation/lithiation capacities and efficiencies of CV measurements (Figure 71) .....	95

---

Table 48: Electrode weights of the following CCC measurements and calculated capacities of Gen3 materials fabricated with different shell compositions .....	96
Table 49: Compositions before pyrolysis of Gen3 materials fabricated with different process parameters .....	97
Table 50: Fluidized bed reactor parameters of Gen3 materials (Table 49) .....	97
Table 51: Electrode weights of the following CCC measurements and calculated capacities of Gen3 materials fabricated with constant pump speed and varied pressure of spray flow.....	99
Table 52: Electrode weights of the following CCC measurements and calculated capacities of Gen3 materials fabricated with varied pump speed and constant pressure of spray flow.....	101
Table 53: Composition of standard silicon-graphite composite electrode.....	107
Table 54: Electrode weights of the following CCC measurements and calculated capacities of materials of different generations and of a standard silicon-graphite composite material (SiC).....	107
Table 55: Used program of rate capability tests.....	110
Table 56: Electrode weights of rate capability test and calculated capacities of materials of Gen(1-3).....	110
Table 57: Used equipments for TEM characterisation .....	112

## 6.6 References

- [1]. *The Hybrid Vehicle Market 2008-2015 Impact on the Battery Business*. **C. Pillot**. s.l. : Avicenne, 2009.
- [2]. **U. Kasavajjula, C. Wang, A.J. Appleby**. Nano- and bulk-silicon-based insertion anodes for lithium-ion secondary cells. *Journal of Power Sources*. 2007, Vol. 163, pp. 1005, 1006, 1023.
- [3]. **M. Ciobanu, J.P. Wilburn, M.L. Krim, D.E. Cliffl**. Fundamentals. *Handbook of Electrochemistry*. 2007, pp. 20-22.
- [4]. **T.B. Reddy**. *Linden's Handbook of Batteries, Fourth Edition*. 2011, pp. 1.3-2.12, 26.1-26.40.
- [5]. **G. Hambitzer, K. Pinkwart, C. Ripp, C. Schiller**. Thermodynamics and Mechanistics. [book auth.] J.O. Besenhard. *Handbook of Battery Materials*. 1999, pp. 2-17.
- [6]. **C.H. Hamann, W. Vielstich**. *Electrochemie 4.Auflage*. 2005, pp. 155-255, 4.
- [7]. [Online] 05 Juni 2012. [http://www.substech.com/dokuwiki/lib/exe/fetch.php?cache=cache&w=635&h=488&media=galvanic\\_cell.png](http://www.substech.com/dokuwiki/lib/exe/fetch.php?cache=cache&w=635&h=488&media=galvanic_cell.png).
- [8]. [Online] 16 November 2009. [http://www.goiit.com/upload/2009/11/16/e27cc18b5f0bc56e57f9b2b89efa5fa5\\_1419003.JPG](http://www.goiit.com/upload/2009/11/16/e27cc18b5f0bc56e57f9b2b89efa5fa5_1419003.JPG).
- [9]. **R.A. Alberty, R.J. Silbey**. *Physical Chemistry*. 1996.
- [10]. [Online] 08 October 2004. <http://faculty.kfupm.edu.sa/ME/hussaini/Corrosion%20Engineering/02.05.05.htm>.
- [11]. **Laboratory, U.S. Department of Energy Office of Fossil Energy National Energy Technology**. *Fuel Cell Handbook, Sixth Edition*. 2002.
- [12]. **A.J. Bard, L.R. Faulkner**. *Electrochemical Methodes: Fundamentals and Applications*. 2001.
- [13]. **P.W. Atkins**. *Physikalische Chemie, Dritte, korrigierte Auflage*. 2001.
- [14]. **C. Daniel, J.O. Besenhard**. *Handbook of Battery Materials, Second Edition*. 2011.
- [15]. **J. Garche**. *Encyclopedia of electrochemical power sources, Volume 5*. 2009.

- [16]. **K.E. Aifantis, S.A. Hackney, R.V. Kumar.** *High Energy Density Lithium Batteries.* 2010, pp. 1-25.
- [17]. **F.R. Kalhammer, B.M. Kopf, D.H. Swan, V.P. Roan.** *Status and Prospects for Zero Emissions Vehicle Technology; Report of the ARB Independent Expert Panel 2007.* 2007, p. 25.
- [18]. **M. Anzai, H. Kato, T. Yamahira.** *Nonaqueous electrolyte secondary battery.* US 5053297 A 1 October 1991.
- [19]. **K. Hwang.** *Cathode Active Material, Cathode Material Having the Cathode Active Material, Secondary Aqueous Lithium-ion Battery Having the Cathode Material, and Method for Preparing the Cathode Active Material.* US20080152995 A1 26 June 2008.
- [20]. **K. Oates.** Lithium-ion Batteries: Commercialization History and current Market. *Foresight Science & Technology.* 2010, pp. 1-4.
- [21]. **M.S. Whittingham.** Electrical Energy Storage and Intercalation Chemistry. *Science.* 1976, Vol. 192, 4244, pp. 1126-1127.
- [22]. **B. Xu, D. Qian, Z. Wang, Y.S. Meng.** Recent progress in cathode materials research for advanced lithium ion batteries. *Materials Science and Engineering R.* 2012, Vol. 73, pp. 52-64.
- [23]. Lithium ion Rechargeable Batteries; Technical Handbook. [Online] 16 August 2007. <http://www.sony.com.cn/products/ed/battery/download.pdf>.
- [24]. Issues in Physics and Society. [Online] 03 April 2013. <http://physicsandsocietybc.files.wordpress.com/2013/04/meriampic.gif>.
- [25]. **D. Andrea.** *Battery Management System for Large Lithium-Ion Battery Packs.* 2010, pp. 1-3.
- [26]. atbatt. [Online] 25 April 2013. <http://www.atbatt.com/blogimages/cylindrical.jpg>.
- [27]. electronic design. [Online] 25 April 2013. <http://electronicdesign.com/power/use-li-ion-batteries-your-next-mobile-computer>.
- [28]. **A. Manthiram.** Materials Aspects: A Overview. [book auth.] G. Pistoia G. Nazri. *Lithium Batteries Science and Technology.* 2004, pp. 3-41.
- [29]. **S. Koller, M. Schmuck.** lecture. *Batteries and Supercapacitors.* 2010.

- [30]. **M. Inaba.** Negative Electrodes: Graphite. [book auth.] J. Garche. *Encyclopedia of Electrochemical Power Sources*. 2009, pp. 198-236.
- [31]. **J. Dahn, G.M. Ehrlich.** Lithium-ion battery. [book auth.] T.B. Reddy. *Linden's Handbook of Batteries; Fourth Edition*. 2011, pp. 26.17-26.22.
- [32]. **Z. Ogumi, M. Inaba.** Carbon Anodes. [book auth.] B. Scrosati W.A. van Schalkwijk. *Advanced in Lithium-Ion Batteries*. 2002.
- [33]. **M. Winter, J.O. Besenhard, M.E. Spahr, P. Novak.** Insertion Electrode Material for Rechargeable Lithium Batteries. *Advanced Materials*. 1998, Vol. 10, pp. 725-763.
- [34]. **M. Winter, K.C. Moeller, J.O. Besenhard.** Carbonaceous and graphitic anodes. [book auth.] G. Pistoia G. Nazri. *Lithium Batteries Science and Technology*. 2004, pp. 151-152.
- [35]. **R. E. Franklin.** Crystallite Growth in Graphitizing and Non-Graphitizing Carbons. *Proceedings of the Royal Society*. 1951, Vol. A209, pp. 196-208.
- [36]. **P.J. F. Harris.** New Perspectives on the Structure of Graphitic Carbons. *Solid State and Materials Sciences*. 2005, Vol. 30, p. 241.
- [37]. **J.O. Besenhard, H. P. Fritz.** The Electrochemistry of Black Carbons. *Angewandte Chemie International Edition English*. 1983, Vol. 22, p. 954.
- [38]. **H. Kren.** About the Continuous Growth of the Solid Electrolyte Interphase in Lithium Ion Batteries. *Doctoral Thesis*. 2011, p. 21.
- [39]. **M. Winter, J.O. Besenhard.** Electrochemical lithiation of tin and tin-based intermetallics and composites. *Electrochimica Acta*. 1999, Vol. 45, pp. 31-50.
- [40]. **J. Yang, J. Wang.** Negative Electrodes: Lithium Alloys. [book auth.] J. Garche. *Encyclopedia of Electrochemical Power Sources Volume 5*. 2009, pp. 225-236.
- [41]. **R. Nesper.** Structure and chemical bonding in zintl-phases containing lithium. *Progress in Solid State Chemistry*. 1990, Vol. 20, p. 1.
- [42]. **R. Nesper.** Bonding Patterns in Intermetallic Compounds. *Angewandte Chemie International Edition English*. 1991, Vol. 30, p. 789.
- [43]. **J. Yang, M. Winter, J.O. Besenhard.** Small particle size multiphase Li-alloy anodes for lithium-ion batteries. *Solid State Ionics*. 1996, Vol. 90, pp. 281-287.
- [44]. **J.O. Besenhard, J. Yang, M. Winter.** Will advanced lithium-alloy anodes have a chance in lithium-ion batteries?. *Journal of Power Sources*. 1997, Vol. 68, p. 87.

- [45]. **B.A. Boukamp, G.C. Lesh, R.A. Huggins.** All-Solid Lithium Electrodes with Mixed-Conductor Matrix. *Journal of The Electrochemical Society*. 1981, Vol. 128, p. 725.
- [46]. **C.J. Wen, R.A. Huggins.** Chemical Diffusion in Intermediate Phases in the Lithium-Silicon System. *Journal of Solid State Chemistry*. 1981, Vol. 37, pp. 271-278.
- [47]. **M.N. Obrovac, L.J. Krause.** Reversible Cycling of Crystalline Silicon Powder. *Journal of the Electrochemical Society*. 2007, Vol. 154, p. A103.
- [48]. **M.N. Obrovac, L. Christensen.** Structural Changes in Silicon Anodes during Lithium Insertion/Extraction. *Electrochemical and Solid-State Letter*. 2004, Vol. 4, pp. A93-A96.
- [49]. **J.R. Dahn, T.D. Hatchard.** In Situ XRD and Electrochemical Study of the Reaction of Lithium with Amorphous Silicon. *Journal of the Electrochemical Society*. 2004, Vol. 151, pp. A838-A842.
- [50]. **X.H. Liu, L. Zhong, S. Huang, S.X. Mao, T. Zhu, J.Y. Huang.** Size-Dependent Fracture of Silicon Nanoparticles During Lithiation. *ACS Nano*. 2012, Vol. 6, pp. 1522-1531.
- [51]. **Z.P. Guo, J.Z. Wang, H.K. Liu, S.X. Dou.** Study of silicon/polypyrrole composite as anode materials for Li-ion batteries. *Journal of Power Sources*. 2005, Vol. 146, p. 448.
- [52]. **H. Li, X. Huang, L. Chen, Z. Wu, Y. Liang.** *Electrochemical and Solid-State Letter*. 1999, Vol. 2, p. 547.
- [53]. **I. Kim, P.N. Kumta, G.E. Blomgren.** Si/TiN Nanocomposites Novel Anode Materials for Li-Ion Batteries. *Electrochemical and Solid-State Letters*. 2000, Vol. 3, pp. 493-496.
- [54]. **I. Kim, G.E. Blomgren, P.N. Kumta.** Nanostructured Si/TiB<sub>2</sub> Composite Anodes for Li-Ion Batteries. *Electrochemical and Solid-State Letters*. 2003, Vol. 6, pp. A157-A161.
- [55]. **I. Kim, G.E. Blomgren, P.N. Kumta.** Si-SiC nanocomposite anodes synthesized using high-energy mechanical milling. *Journal of Power Sources*. 2004, Vol. 130, pp. 275-280.
- [56]. **Z.P. Guo, Z.W. Zhao, H.K. Liu, S.X. Dou.** Lithium insertion in Si-TiC nanocomposite materials produced by high-energy mechanical milling. *Journal of Power Sources*. 2005, Vol. 146, pp. 190-194.
- [57]. **A. Netz, R.A. Huggins, W. Weppner.** The formation and properties of amorphous silicon as negative electrode reactant in lithium systems. *Journal of Power Sources*. 2003, Vols. 119-121, pp. 95-100.
- [58]. **J. Wolfenstine.** CaSi<sub>2</sub> as an anode for lithium-ion batteries. *Journal of Power Sources*. 2003, Vol. 124, pp. 241-245.

- [59]. **J. Yang, Y. Takeda, N. Imanishi, C. Capiglia, J.Y. Xie, O. Yamamoto.** SiO<sub>x</sub>-based anodes for secondary lithium batteries. *Solid State Ionics*. 2002, Vols. 152-153, pp. 125-129.
- [60]. **A.M. Wilson, J.N. Reimers, E.W. Fuller, J.R. Dahn.** Lithium insertion in pyrolyzed siloxane polymers. *Solid State Ionics*. 1994, Vol. 74, pp. 252-254.
- [61]. **J.S. Xue, K. Myrtle, J.R. Dahn.** An Epoxy-Silane Approach to Prepare Anode Materials for Rechargeable Lithium Ion Batteries. *Journal of The Electrochemical Society*. 1995, Vol. 142, pp. 2927-2935.
- [62]. **W. Xinga, A.M. Wilson, G. Zank, J.R. Dahn.** Pyrolysed pitch-polysilane blends for use as anode materials in lithium ion batteries. *Solid State Ionics*. 1997, Vol. 93, pp. 239-244.
- [63]. **X. Yang, J. McBreen, W. Yoon, M. Yoshio, H. Wang, K. Fukuda, T. Umeno.** Structural studies of the new carbon-coated silicon anode materials using synchrotron-based in situ XRD. *Electrochemistry Communications*. 2002, Vol. 4, pp. 893-897.
- [64]. **B. Kim, H. Uono, T. Sato, T. Fuse, T. Ishihara, M. Senna.** Li-ion battery anode properties of Si-carbon nanocomposites fabricated by high energy multiring-type mill. *Solid State Ionics*. 2004, Vol. 172, pp. 33-37.
- [65]. **M. Holzzapfel, H. Buqa, W. Scheifele, P. Novak, F. Petrat.** A new type of nano-sized silicon/carbon composite electrode for reversible lithium insertion. *Chemical Communications*. 2005, 12, pp. 1566-1568.
- [66]. **N. Dimov, S. Kugino, M. Yoshio.** Mixed silicon–graphite composites as anode material for lithium ion batteries: Influence of preparation conditions on the properties of the material. *Journal of Power Sources*. 2004, Vol. 136, pp. 108-114.
- [67]. **W. Liu, M. Yang, H. Wu, S. M. Chiao, N. Wu.** Enhanced Cycle Life of Si Anode for Li-Ion Batteries. *Electrochemical and Solid-State Letters*. 2005, Vol. 8, pp. A100-A103.
- [68]. **J. Li, R.B. Lewis, J.R. Dahn.** Sodium Carboxymethyl Cellulose A Potential Binder for Si Negative Electrodes for Li-Ion Batteries. *Electrochemical and Solid-State Letters*. 2007, Vol. 10, pp. A17-A20.
- [69]. **N.S. Hochgatterer, M.R. Schweiger, S. Koller, P.R. Raimann, T. Wöhrle, C. Wurm, M. Winter.** Silicon/Graphite Composite Electrodes for High-Capacity Anodes: Influences of Binder Chemistry on Cycling Stability. *Electrochemical and Solid-State Letters*. 2008, Vol. 11, pp. A76-A80.

- [70]. **D. Mazouzi, B. Lestriez, L. Roue, D. Guyomard.** Silicon Composite Electrode with High Capacity and Long Cycle Life. *Electrochemical and Solid-State Letters*. 2009, Vol. 12, pp. A215-A218.
- [71]. **P. Kurzweil, K. Brandt.** Secondary Batteries-Lithium Rechargeable System: Overview. [book auth.] J.Garche. *Encyclopedia of Electrochemical Power Sources Volume 5*. 2009, pp. 1-39.
- [72]. **M.S. Whittingham.** Lithium Batteries and Cathode Materials. *Chemical Review*. 2004, Vol. 104, p. 4273.
- [73]. **J. Chen.** Recent Progress in Advanced Materials for Lithium Ion Batteries. *Materials*. 2003, Vol. 6, pp. 157-160.
- [74]. **D. Morgan, A. Van der Ven, G. Ceder.** Li Conductivity in  $\text{Li}_x\text{MPO}_4$  (M = Mn, Fe, Co, Ni) Olivine Materials. *Electrochemical and Solid-State Letters*. 2004, Vol. 7, pp. A30-A32.
- [75]. **C.A.J. Fisher, V.M. Hart Prieto, M.S. Islam.** Lithium battery materials  $\text{LiMPO}_4$  (M = Mn, Fe, Co, and Ni): insights into defect association, transport mechanisms, and doping behavior. *Chemistry of Materials*. 2008, Vol. 20, pp. 5907-5915.
- [76]. **A.K. Padhi, K.S. Nanjundaswamy, C. Masquelier, S. Okada, J.B. Goodenough.** Effect of Structure on the  $\text{Fe}^{3+}/\text{Fe}^{2+}$  Redox Couple in Iron Phosphates. *Journal of Electrochemical Society*. 1997, Vol. 144, pp. 1609-1613.
- [77]. **S. Nishimura, G. Kobayashi, K. Ohoyama, R. Kanno, M. Yashima, A. Yamada.** Experimental visualization of lithium diffusion in  $\text{Li}_x\text{FePO}_4$ . *Nature Materials*. 2008, Vol. 7, pp. 707-711.
- [78]. **J. Molenda, M. Molend.** Composite Cathode Material for Li-Ion Batteries Based on  $\text{LiFePO}_4$  System. [book auth.] J. Cuppoletti. *Metal, Ceramic and Polymeric Composites for Various Uses*. 2001, p. 626.
- [79]. **J. Wolfenstine, J. Allen.**  $\text{LiNiPO}_4$ - $\text{LiCoPO}_4$  solid solutions as cathodes. *Journal of Power Sources*. 2004, Vol. 136, pp. 150-153.
- [80]. **J. Wolfenstine, J. Allen.**  $\text{Ni}^{3+}/\text{Ni}^{2+}$  redox potential in  $\text{LiNiPO}_4$ . *Journal of Power Sources*. 2005, Vol. 142, pp. 389-390.
- [81]. **K. Xu.** Nonaqueous Liquid Electrolytes for Lithium-Based Rechargeable Batteries. *Chemical Reviews*. 2004, Vol. 104, pp. 4303-4417.

- [82]. **K. Xu.** Electrolytes Overview. [book auth.] J. Garche. *Encyclopedia of Electrochemical Power Sources Volume 5*. 2009, pp. 51-70.
- [83]. **M. Ue.** Electrolytes: Nonaqueous. [book auth.] J.Garche. *Encyclopedia of Electrochemical Power Sources Volume 5*. 2009, pp. 71-83.
- [84]. **H. Tanji.** Separators. [book auth.] J. Garche. *Encyclopedia of Electrochemical Power Sources*. 2009, pp. 356-367.
- [85]. **W.C. Yu, S.E. Hux.** *Method of making a trilayer battery separator*. US 5952120 United States, 15 April 1997.
- [86]. **P. Arora, Z.J. Zhang.** Battery Separator. *Chemical Review*. 2004, Vol. 104, p. 4424.
- [87]. **A. Chagnes, J. Swiatowska.** Electrolyte and Solid-Electrolyte Interphase Layer in Lithium-Ion Batteries. [book auth.] I. Belharouak. *Lithium Ion Batteries - New Developments*. s.l. : <http://www.intechopen.com/books/lithium-ion-batteries-new-developments/electrolyte-and-solid-electrolyte-interphase-layer-in-lithium-ion-batteries>, pp. 157-164.
- [88]. **K. Xu, Y. Lam, S.S. Zhang, T.R. Jow, T.B. Curtis.** Solvation Sheath of Li<sup>+</sup> in Nonaqueous Electrolytes and Its Implication of Graphite/Electrolyte Interface Chemistry. *The Journal of Physical Chemistry C*. 2007, Vol. 111, pp. 7411-7421.
- [89]. **M.R. Wagner, J.H. Albering, K.C. Möller, J.O. Besenhard, M. Winter.** XRD Evidence for the Electrochemical Formation of Li<sup>+</sup>(PC)<sub>y</sub>Cn<sup>-</sup> in PC-based Electrolytes. *Electrochemistry Communications*. 2005, Vol. 7, p. 947.
- [90]. **E. Peled, D.B. Tow, A. Merson, A. Gladkikh, L. Burstein, D. Golodnitsky.** Composition, depth profiles and lateral distribution of materials in the SEI built on HOPG-TOF SIMS and XPS studies. *Journal of Power Sources*. 2001, Vols. 97-98, pp. 52-57.
- [91]. **E. Peled, D. Golodnitsky, J. Penciner.** The Anode/Electrolyte Interface. [book auth.] J.O. Besenhard. *Handbook of Battery Materials*. 1999, pp. 419-456.
- [92]. **W. Zhang.** A review of the electrochemical performance of alloy anodes for lithium-ion batteries. *Journal of Power Sources*. 2011, Vol. 196, pp. 13-24.
- [93]. **J. Vetter, P. Novak, M.R. Wagner, C. Veit, K.C. Möller, J.O. Besenhard, M. Winter, M. Wohlfahrt-Mehrens, C. Vogler, A. Hammouche.** Ageing mechanisms in lithium-ion batteries. *Journal of Power Sources*. 2005, Vol. 147, pp. 268-281.

- [94]. **M. Broussely, S. Herreyre, P. Biensan, P. Kasztejna, K. Nechev, R.J. Staniewicz.** Aging mechanism in Li ion cells and calendar life predictions. *Journal of Power Sources*. 2001, Vols. 97-98, pp. 13-21.
- [95]. **M. Wohlfahrt-Mehrens, C. Vogler, J. Garche.** Aging mechanisms of lithium cathode materials. *Journal of Power Sources*. 2004, Vol. 127, pp. 58-64.
- [96]. **J. Vetter, M. Winter, M. Wohlfahrt-Mehrens.** Aging Mechanisms. [book auth.] J. Garche. *Encyclopedia of Electrochemical Power Sources*. 2009, pp. 393-403.
- [97]. **W. Rähse.** Produktdesign disperser Stoffe: Industrielles Partikelcoating. *Chemie Ingenieur Technik*. 2009, Vol. 81, pp. 225-239.
- [98]. **B. Guignon, E. Regalado, A. Duquenoy, E. Dumoulin.** Helping to choose operating parameters for a coating fluid bed process. *Powder Technology*. 2003, Vol. 130, pp. 193-198.
- [99]. **N. Hampel, A. Brück, M. Peglow, E. Tsotsas.** Continuous pellet coating in a Wurster fluidized bed process. *Chemical Engineering Science*. 2013, Vol. 86, pp. 87-98.
- [100]. **F. Christensen, P. Bartelsen.** Qualitative description of the Wurster-based fluid-bed coating process. *Drug Development and Industrial Pharmacy*. 1997, Vol. 23, pp. 451-463.
- [101]. **S.G. Lopez.** Fachlabor Mechanische Verfahrenstechnik Wirbelschichttechnik. 2010.
- [102]. **Glatt.** Glatt. [Online] 16 May 2013. <http://www.glatt.com/cm/en/process-technologies/coating/fluid-bed-coating.html>.
- [103]. **M. Scharfegger, H. Kren, S. Koller.** *Strukturstabiles Aktivmaterial für Batterieelektroden*. EP 2 573 845 A1 26 September 2011.
- [104]. **W. Jiang, T. Tran, X. Song, K. Kinoshita.** Thermal and electrochemical studies of carbons for Li-ion batteries 1. Thermal analysis of petroleum and pitch cokes. *Journal of Power Sources*. 2000, Vol. 85, pp. 261-268.
- [105]. **Z.S. Wen, J. Yang, B.F. Wang, K. Wang, Y. Liu.** High capacity silicon/carbon composite anode materials for lithium ion batteries. *Electrochemistry Communications*. 2003, Vol. 5, pp. 165-168.
- [106]. **X. Zhang, P.K. Patil, C. Wang, A.J. Appleby, F.E. Little, D.L. Cocke.** Electrochemical performance of lithium ion battery, nano-silicon-based, disordered carbon composite anodes with different microstructures. *Journal of Power Sources*. 2004, Vol. 125, pp. 206-213.

- [107]. **P. Zuo, G. Yin, Y. Ma.** Electrochemical stability of silicon/carbon composite anode for lithium ion batteries. *Electrochimica Acta*. 2007, Vol. 52, pp. 4878–4883.
- [108]. **I. Kim, P.N. Kumta.** High capacity Si/C nanocomposite anodes for Li-ion batteries. *Journal of Power Sources*. 2004, Vol. 136, pp. 145-149.
- [109]. **Y. Liu, Z.Y. Wen, X.Y. Wang, A. Hirano, N. Imanishi, Y. Takeda.** Electrochemical behaviors of Si/C composite synthesized from F-containing precursors. 2009, Vol. 189, pp. 733-737.
- [110]. **H. Li, X. Huang, L. Chen, Z. Wu, Y. Liang.** A High Capacity Nano-Si Composite Anode Material for Lithium Rechargeable Batteries. *Electrochemical and Solid-State Letters*. 1999, Vol. 2, pp. 547-549.
- [111]. **J.P. Maranchi, A.F. Hepp, P.N. Kumta.** High Capacity, Reversible Silicon Thin-Film Anodes for Lithium-Ion Batteries. *Electrochemical and Solid-State Letters*. 2003, Vol. 6, pp. A198-A201.
- [112]. **K.T. Lee, J. Cho.** Roles of nanosize in lithium reactive nanomaterials for lithium ion batteries. *Nano Today*. 2011, Vol. 6, p. 33.
- [113]. **K. Zaghib, G. Nadeau, K. Kinoshita.** Effect of Graphite Particle Size on Irreversible Capacity Loss. *Journal of Electrochemical Society*. 2000, Vol. 147, pp. 2110-2115.
- [114]. **Y.S. Jung, K.T. Lee, S.M. Oh.** Si-carbon core-shell composite anode in lithium secondary batteries. *Electrochimica Acta*. 2007, Vol. 52, p. 7063.
- [115]. **L. Xue, G. Xu, Y. Li, K. Fu, Q. Shi, X. Zhang.** Carbon-Coated Si Nanoparticles Dispersed in Carbon Nanotube Networks As Anode Materials for Lithium-Ion Batteries. *ACS Applied Material Interfaces*. 2013, Vol. 5, p. 23.
- [116]. **N.S. Hochgatterer.** *Zellulosechemie in der Lithium-Ionen-Technologie: Integrität von hochkapazitiven, nanostrukturierten Metall- und Halbmetall-Komposit-Anoden*. 2008. pp. 194-198.
- [117]. **M. Wachter, J.O. Besenhard, M. Winter.** Tin and tin-based intermetallics as new anode materials for lithium-ion cells. *Journal of Power Sources*. 2001, Vol. 94, pp. 189-193.
- [118]. **K. Guerin, A. Fevrier-Bouvier, S. Flandrois, B. Simon, P. Biensan.** On the irreversible capacities of disordered carbons in lithium-ion rechargeable batteries. *Electrochimica Acta*. 2000, Vol. 45, pp. 1607-1615.

[119]. *Battery University*. [Online] 18 July 2013. [http://batteryuniversity.com/learn/article/battery\\_definitions](http://batteryuniversity.com/learn/article/battery_definitions).

[120]. **H.S. Choi, C.R. Park**. Towards high performance anodes with fast charge/discharge rate for LIB based electrical vehicles. [book auth.] C.R. Park. *Lithium-ion Batteries*. 2010.